Yerbilimleri, 2024, 45 (1), 1-51, 1393877

Hacettepe Üniversitesi Yerbilimleri Uygulama ve Araştırma Merkezi Bülteni (*Bulletin of the Earth Sciences Application and Research Centre of Hacettepe University*

YERBİLİMLERİ
Bulletin for Earth Sciences

ISSN: 2687- 2978

Mineralogical, Petrographical, and Geochemical Properties of the Late Oligocene Coal Seam (Seam-VI): Insights into Elemental Enrichments and Palaeodepositional Environment (İbrice field, Thrace Basin)

Geç Oligosen Yaşlı Kömür Damarının (VI No'lu) Mineralojik, Petrografik ve Jeokimyasal Özellikleri: Elementel Zenginleşmeler ve Çökelme Ortamı Değerlendirmeleri (İbrice Sahası, Trakya Havzası)

ALİ İHSAN KARAYİĞİT [1], RIZA GÖRKEM OSKAY [2]*, CÜNEYT BİRCAN [3]

[1] Hacettepe University, Department of Geological Engineering, Ankara, Türkiye

[2] Hacettepe University, Başkent OSB Technical Sciences Vocational School, Ankara, Türkiye

[3] Balıkesir University, Department of Geological Engineering, Balıkesir, Türkiye

Received *(geliş)*: 21 November (*Kasım*) 2023 Accepted *(kabul):* 26 Febuary(*Şubat*) 2024

ABSTRACT

The Thrace Basin hosts several mineable coal seams (upwards numbered I to VII) within the coal-bearing Late Oligocene-age Danişmen Formation. For the first time, the properties of the Seam-VI in the İbrice (Malkara) area have been investigated in order to evaluate elemental enrichments and palaeoenvironmental conditions. The xylite-rich and mineral-rich lithotypes were identified from the studied coal samples representing the whole-coal thickness. The coal samples, on a dry basis, display variable ash yields (13.2–63.0%), total C (21.2–57.8%), and total S (0.9–4.1%) contents. The minerals identified using XRD-whole rock analysis include clay minerals, quartz, pyrite, calcite, dolomite, and feldspars. Siderite is only identified in a single sample. Aragonite is detected in two samples, which contain fossil shell remains. The SEM observations agree with XRD data, and apatite, barite, biotite, pentlandite, sphalerite, Ti-oxide, and zircon were also identified as accessory phases. Huminite is the predominant maceral group in the studied samples, while liptinite and inertinite group macerals display variable proportions. The mean %Rr values of ulminite macerals are around 0.40-0.41±0.01-0.02%, indicating relatively low-rank coal. This study implies that the precursor peat-mires of the Seam-VI were mainly developed under forested mire conditions, where woody peat-forming plants were abundant, and occasionally the contributions of herbaceous plants were important. The coexistence of syngenetic pyrite and carbonate minerals (e.g., siderite and carbonate mineral bands) could be related to the development of weakly acidic to neutral conditions within palaeomires. Furthermore, the predominance of clay minerals and the presence of detrital accessory minerals (e.g., apatite, pentlandite, and Ti-oxides) can also be indicators of clastic influx into palaeomires. Although aluminosilicate minerals (e.g., clay minerals) are abundant in dominant phases, SEM-EDX data shows that accessory minerals mainly control the elemental enrichments in the Seam-VI. The Mn enrichments in the samples seem to be controlled by Mn-bearing siderite micronodules. Considering the presence of sulphide mineralization and metallic ore deposits in the Strandja and Rhodope massifs, enrichments of Cr, Co, Ni, Ge, and Mo are related to As-bearing pyrite grains and accessory sphalerite and pentlandite grains within clay mineral aggregates in the samples. In addition, the Sr-bearing barite overgrowths around feldspar grains and syngenetic carbonate mineral bands could also cause Sr enrichments. Overall, clastic influx ratios into palaeomires and pH conditions during peat accumulation controlled the elemental enrichments in the Seam-VI.

Keywords: Coal, Danişmen Formation, elemental enrichments, mineralogy, petrography, Thrace Basin

ÖZ

Trakya Havzası, Geç Oligosen yaşlı, kömür içeren Danişmen Formasyonu içerisinde, I'den VII'ye kadar işletilebilir kömür damarına ev sahipliği yapmaktadır. Elementel zenginleşmelerin ve paleoortam koşullarının değerlendirilmesi amacıyla İbrice (Malkara) bölgesindeki Damar-VI'nın özellikleri ilk kez bu çalışma kapsamında araştırılmıştır. İncelenen kömür örneklerinden tüm kömür kalınlığını temsil edecek şekilde ksilitçe zengin ve mineralce zengin litotipleri tanımlanmıştır. Kömür örnekleri kuru bazda geniş bir aralıkta kül verimi (%13,2–63,0), toplam C (%21,2–57,8) ve toplam S (%0,9–4,1) içeriğini göstermektedir. XRD-tüm kaya analizi kullanılarak tanımlanan mineraller kil mineralleri, kuvars, pirit, kalsit, dolomit ve feldspatlardır. Siderit yalnızca bir örnekten tanımlanırken, fosil kabuk kalıntıları içeren iki örnekte aragonit tespit edilmiştir. SEM gözlemleri XRD verileriyle uyumlu olup, apatit, barit, biyotit, pentlandit, sfalerit, Ti-oksit ve zirkon da aksesuar fazlar olarak belirlenmiştir. Çalışılan örneklerde hüminit baskın maseral grubunu oluştururken, liptinit ve inertinit grubu maseraller değişken oranlar göstermektedir. Ulminit maserallerinin ortalama %Rr değerleri 0,40-0,41±0,01-0,02% civarında olup, nispeten düşük dereceli kömürü işaret etmektedir. Bu çalışma, Damar-VI'nın ilksel turba bataklıklarının çoğunlukla odunsu turba oluşturan bitkilerin yaygın olduğu ormanlık bataklık koşullarında geliştiğini ve zaman zaman otsu bitkilerin katkılarının arttığını işaret etmektedir. Sinjenetik pirit ve karbonat minerallerinin (örneğin, siderit ve karbonat mineral bantları) bir arada bulunması, ilksel turbalıklardaki zayıf asidik ila nötr koşulların gelişimi ile ilişkili olabilir. Ayrıca, kil minerallerinin baskınlığı ve kırıntılı aksesuar minerallerin (örneğin apatit, pentlandit ve Ti-oksitler) varlığı da ilksel turbalıklara kırıntılı sedimant girdisinin göstergeleri olabilir. Her ne kadar alüminosilikat mineralleri (örneğin kil mineralleri) baskın bol ve baskın fazlar olarak bulunsa da, SEM-EDX verileri esasen aksesuar minerallerin Damar-VI'daki elementel zenginleşmeleri kontrol ettiğini göstermektedir. Örneklerdeki Mn zenginleşmelerinin Mn içeren siderit mikronodüller tarafından kontrol edildiği görülmektedir. Istranca ve Rodop masiflerinde sülfit mineralizasyonu ve metalik cevher yataklarının varlığı göz önüne alındığında, örneklerdeki Cr, Co, Ni, Ge ve Mo zenginleşmeleri, kil mineral agregatları içindeki As içeren pirit taneleri ve aksesuar sfalerit ve pentlandit taneleri ile ilişkilidir. Ayrıca feldspat taneleri etrafındaki Sr taşıyan barit büyümeleri ve sinjenetik karbonat mineral bantları Sr zenginleşmesine neden olabilir. Genel olarak, turba birikimi sırasında ilksel turbalıklara kırıntı girdisinin oranı ve pH koşullarının Damar-VI'daki element zenginleşmelerini kontrol ettiği anlaşılmaktadır.

Anahtar Kelimeler: *Kömür, Danişmen Formasyonu, element zenginleşmesi, mineraloji, petrografi, Trakya Havzası*

https://doi.org/10.17824/yerbilimleri.1393877

*Sorumlu Yazar/ Corresponding Author: rizagorkemoskay@hacettepe.edu.tr

INTRODUCTION

With increasing energy demands, elemental and mineralogical features of coal seams became important for reducing environmental impacts, recovering some critical elements from coal and its combustion remains, and improving the combustion efficiency of boilers in power plants (e.g., Dai and Finkelman, 2018; Dai et al., 2021, 2023; Finkelman et al., 2019;

Hower et al., 2023; Pan et al., 2020). Besides, mineralogical, petrographic, and geochemical properties of coal seams could provide essential data about the palaeodepositional conditions during the precursor peat accumulation. For instance, predominance of syngenetic carbonate minerals and natural zeolite minerals in coal seams could indicate alkaline conditions within the palaeomire, while the presence of syngenetic authigenic kaolinite could be evidence of open hydrogeological conditions and synchronous and/or epiclastic volcanic inputs into palaeomires (e.g., Dai et al., 2020a; Karayiğit et al., 2017; Querol et al., 1997; Ward, 2002, 2016). Furthermore, relatively high concentrations of B, S, and/or Mn could indicate possible marine influence into palaeomires (e.g., Dai et al., 2020a; Goodarzi and Swaine, 1994; Hower et al., 2002). Therefore, several studies have been conducted on coal deposits across the world, as well as on Turkish coal deposits within this scope. The studies about Turkish coal seams are mostly focused on Neogene coal seams due to their usages as a feeding coal-fired power plants (e.g., Gürdal, 2011; Karayiğit et al., 2000; Palmer et al., 2004). Even though most coal resources in the Thrace Basin are hosted in the Oligocene sequences, these seams received less concerns than the Turkish Neogene coals, and a limited number of studies focused on these seams (e.g., Çelik et al., 2017; Erarslan and Örgün, 2017; Erarslan et al., 2014, 2020).

The Thrace Basin is bordered by the Strandja Massif to the north, the Rhodope Massif to the west, and the Sakarya Zone to the south (Figure 1a). It has a very thick (c. 9000 m) Cenozoic basinal infillings (Figure 1b) (Gürgey and Batı, 2018; Okay et al., 2023; Perinçek et al., 2015; Siyako, 2006; Turgut and Eseller, 2000). More importantly, the basin hosts most of the natural gas and limited oil resources of Türkiye (Huvaz et al., 2007); nevertheless, several mineable coal seams are also located in the basin within the Cenozoic basinal infillings. Early exploration studies during the 1970s show that there are eleven coal seams (upwards from I to XI), of which seven (I to VII) are economic, and located in the latest Early-Late Oligocene Danişmen Formation (Lebküchner, 1974). These seams are exploiting different coalfields in the southwestern and north-eastern parts of the Thrace Basin. Even though the sedimentological features, source rock potential, and depositional environment of certain Palaeogene formations in the basin are well-known due to the existence of hydrocarbon systems, limited studies were conducted on the coal seams within the latest Early-Late Oligocene Danişmen Formation (Çelik et al., 2017; Erarslan and Örgün, 2017; Erarslan et al., 2014, 2020; Karayiğit et al., 2022a; Tuncalı et al., 2002). These studies show that coal seams in the Danişmen Formation are commonly characterized by low ash yields, high total huminite contents, and relatively high total S, volatile matter, and B contents. Furthermore, these studies also indicate that the palaeomires in the Thrace Basin were mostly accumulated under forested mire conditions within flood plains, and some of these mires were also opened to marine influence (Çelik et al., 2017; İslamoğlu et al., 2010; Karayiğit et al., 2022a; Leibkühner, 1974; Siyako, 2006). Therefore, high total S and B contents could be related to marine influence. However, detailed coal mineralogy studies from the Malkara and Yeniköy coalfields also noted that the relatively high total S contents could also be controlled by anoxic marine conditions, while clastic influxes from the Strandja Massif might also cause elevations in the B contents of these seams. Also, coal

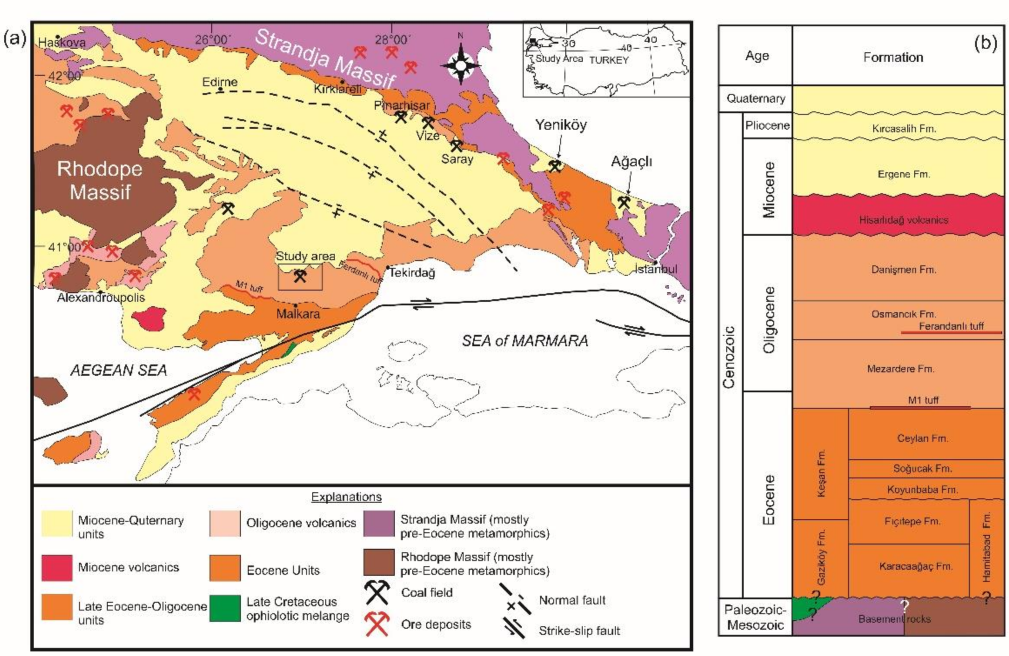

Figure 1: (a) Geological map of the Thrace Basin (modified from Karayiğit et al. (2022a), Siyako (2006), Okay et al. (2023), and (b) generalized stratigraphic column of the Thrace Basin (modified from Gürgey and Batı (2020), Karayiğit et al. (2022a), Siyako (2006) and Okay et al. (2023).

Şekil 1: *(a) Trakya Havzası'nın jeolojik haritası (Karayiğit vd. (2022a), Siyako (2006) ve Okay vd. (2023)'den değiştirilerek alınmıştır) ve (b) Trakya Havzası'nın genelleştirilmiş stratigrafik kolon kesiti (Gürgey ve Batı (2020), Karayiğit vd. (2022a), Siyako (2006) ve Okay vd. (2023)'den değiştirilerek alınmıştır).*

seams in the Malkara coalfield display different paleontological and sedimentological features (İslamoğlu et al., 2010; Karayiğit et al., 2022a; Lebküchner, 1974; Şafak, 2019). For instance, the precursor peat mires of coal seams in the northern and western parts of the coalfield (e.g., Şahin, Pirinçeşme, and Hasköy areas) were accumulated flood plain and freshwater conditions, while palaeomires of coal seams in the sectors in the eastern part (e.g., Pullukçu area) seem to be formed under back mangrove conditions, where open to influence of seawater penetration (İslamoğlu et al., 2010; Karayiğit et al., 2022a). Considering the locations of coal-bearing areas in the Malkara coalfield (Figure 2), possible marine influence into palaeomires of the Seam-VI in the İbrice area could be possible. Nevertheless, the Seam-VI has not been investigated in detail to date. In this study, we aimed to investigate the mineralogical, petrographic, and geochemical properties of the Seam-VI and evaluate elemental enrichments and palaeoenvironmental conditions during the peat accumulation. The specific goal of this study is to compare the mineralogical and petrographic properties of the Seam-VI with those of other seams in the northern and eastern parts of the Thrace basin.

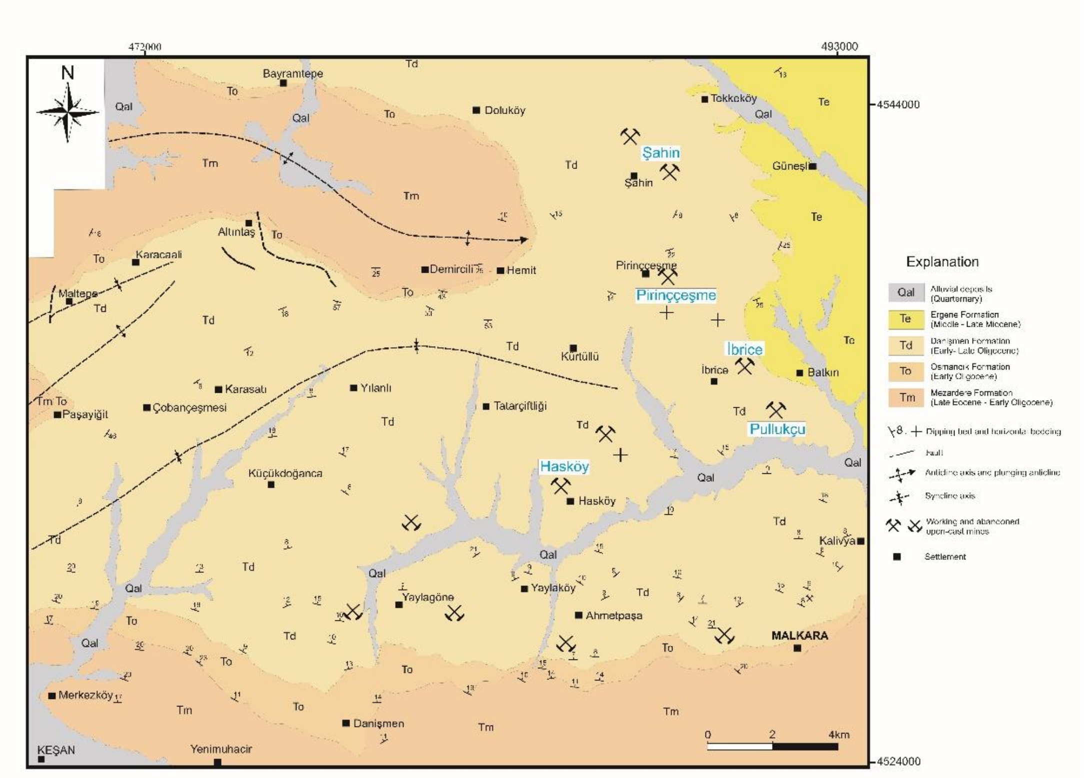

Figure 2: Geological map of the surrounding area of the İbrice area (modified from Karayiğit et al. (2022a).

Şekil 2: *İbrice sahası çevresinin jeolojik haritası (Karayiğit ve diğerleri (2022a)'dan değiştirilerek alınmıştır).*

GEOLOGY

The İbrice area (Malkara coalfield) is positioned in the southwestern part of the Thrace Basin (Figure 1a). Although pre-Cenozoic basement rocks do not crop out in the study area, the basement rocks mainly compose of metamorphic and magmatic rocks of the Strandja Massif in the northern parts of the Thrace Basin and the Rhodope Massif in the western parts of the basin, and ophiolitic rocks of Cretaceous-Paleogene Çetmi Mélange in the southern parts of the basin (Figure 1a-b). The Cenozoic basinal infillings, which crop out in the study area, are, from bottom to top, the Late Eocene-Early Oligocene Mezardere Formation, the Early Oligocene Osmancık Formation, the Early-Late Oligocene Danişmen Formation, and the Middle-Late Miocene Ergene Formation (Figure 2). The Mezardere Formation, locally also known as Mezardere shales, consists of an alternation of shale, marl, and sandstone, and tuffite layer were reported from the lower parts of the formation. Previous paleontological and sedimentological studies have reported that a major sea-level drop in the Eastern Paratethys developed during the Late Eocene and Early Oligocene; as a result, several transgressions and regressions also developed in the Thrace Basin during this period (Gürgey and Batı, 2018; Turgut and Eseller, 2000). Hence, the Mezardere Formation was deposited under prodelta and shallow marine conditions. The Osmancık Formation gradually overlies the Mezardere Formation and composes mainly of sandstone and shale, and, to a lesser extent, pebblestones and limestones. Furthermore, uneconomic coal seams and tuffite layers were also reported from this formation. The previous studies indicate that the Osmancık Formation mainly deposited under front delta and shallow marine conditions (Siyako, 2006; Turgut and Eseller, 2000).

MATERIAL AND METHODS

A total of fifteen samples (eight coal, and seven roof and intercalation samples) were gathered from the Seam-VI in the İbrice area using the channel sampling method (Figure 3). The lithotype descriptions of coal samples were done following the International Committee for Coal and Organic Petrography (ICCP) nomenclature on site (ICCP, 1993). Standard proximate, ultimate, and calorific analyses were conducted following the American Society for Testing and Materials (ASTM) standards using LECO TGA-601, SC-144DR, TruSpec, and AC 350 equipment at Hacettepe University (ASTM D3174, 2020; ASTM D3175, 2020; ASTM D3302/D3302M, 2022; ASTM D5373, 2021; ASTM D5865/D5865M, 2019). Coal petrography studies were conducted on polished blocks using a Leica DM4000M microscope, and ICCP classification was followed for maceral descriptions (ICCP, 2001; Pickel et al., 2017; Sýkorova et al., 2005). The random huminite reflectance measurements (%Rr) were done from ulminite B according to the International Organization for Standardization (ISO) 7404–5 (2009) standard. Rigaku D/MAX 2200 PC equipment equipped with CuKα radiation was used for X-ray powder diffraction (XRD) analyses, and Rietveld-based TOPAS-3 software is used for semi-quantitative mineralogical composition determination. The XRD-clay fraction (XRD-CF) analyses were conducted from selected five samples (18-13/01, 18-13/06, 18-13/11 and 18-13/14) according to methodology described in Karayiğit et al. (2022c). Major oxide contents, and minor and trace element compositions of studied coal and organic mudstone samples were conducted from ashed samples at 450˚C using a muffle furnace, according to Nadkarni (1980) at Hacettepe University. Major oxide contents were determined from pellets using XRF equipment according to the ASTM D-4326 standard at Standart Laboratories S.A, Kocaeli-Türkiye. The ashed samples were sequentially digested using HF, HCL, and nitric acid, and the diluted samples were analyzed using inductively coupled plasma-optical emission spectrometry (ICP-OES) according to the ISO-11885 standard at Standart Laboratories S.A. The accuracy of analyses was crosschecked using international and internal standards. Selected polished blocks of three coal samples (18-13/03, 18-13/04, and 18-13/10) were coated with carbon and examined under a Thermo Fisher Scientific FEI Quanta 400 MK2 SEM-EDX microscope at the General Directorate of Mineral Research and Exploration (MTA) to identify possible accessory mineral phases and to have a better understanding of the elemental compositions.

RESULTS

Standard coal quality

The coal samples from the Seam-VI exhibit a black colour on-site and contain bands of xylite and/or clayey material, and fossil shell remains. The xylite-rich and mineral-rich lithotypes were identified from the studied coal samples (Figure 3). Although it is not officially described by the

ICCP (1993), xylite-rich lithotype could be divided into xylo-detritic and detro-xylitic according to the presence of clastic bands within xylite-rich coals (Fabiańska and Kurkiewicz, 2013; Kolcon and Sachsenhofer, 1999; Karayiğit et al., 2021). In the studied Seam-VI, the xylo-detritic sub-lithotype, which is clayey bands-bearing xylite-rich coal, is also identified from one sample (18–13/09).

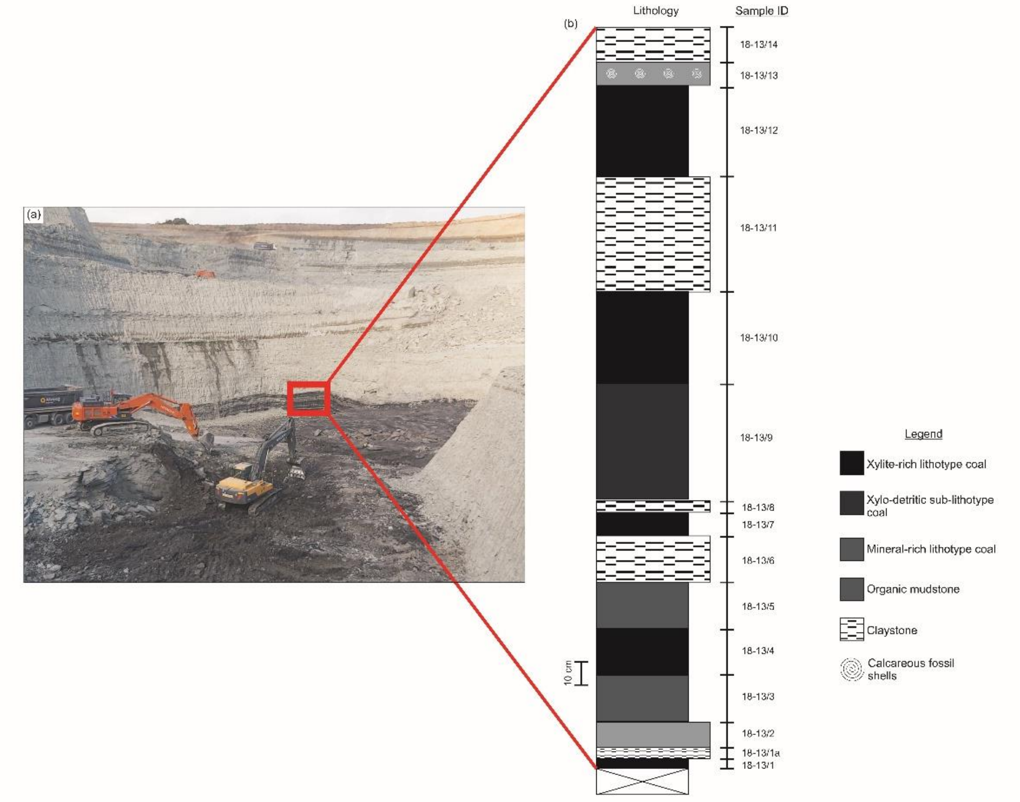

Figure 3: General view of (a) an open-cast mine and (b) the sampling profile studied in the İbrice area.

Şekil 3: *(a) İbrice sahasındaki açık ocağın genel görünümü ve (b) çalışma kapsamında çalışan kesit.*

Considering the presence of xylite-rich and mineral-rich lithotypes in the Seam-VI, the coal samples display on a dry basis variable ash yields, volatile matter, total C and H contents, and gross calorific values (Table 1 and Figure 4). As expected, xylite-rich lithotype-bearing samples generally display low ash yields, and high total C contents and gross calorific values, while mineral-rich ones show significantly high ash yields and low total C and gross calorific values (Table 1 and Figure 4). As can be seen in the coal petrography section, the distribution of H contents seems to be related to maceral compositions. The total S contents of coal samples are generally lower than 2% on a dry basis; nevertheless, samples in which pyrite is an abundant phase, have relatively higher total S (up to 4.1% on a dry basis) contents than the other coal samples (Table 1). Furthermore, carbonaceous shale (18-13/02) and organic mudstone (18-13/13) samples have ash yields higher than 50.0% on a dry basis (Table 1 and Figure 4). The samples from the İbrice area have similar ash yields, total C, H and total S contents, and gross calorific values, to those from other coal mining areas in the Malkara coalfield.

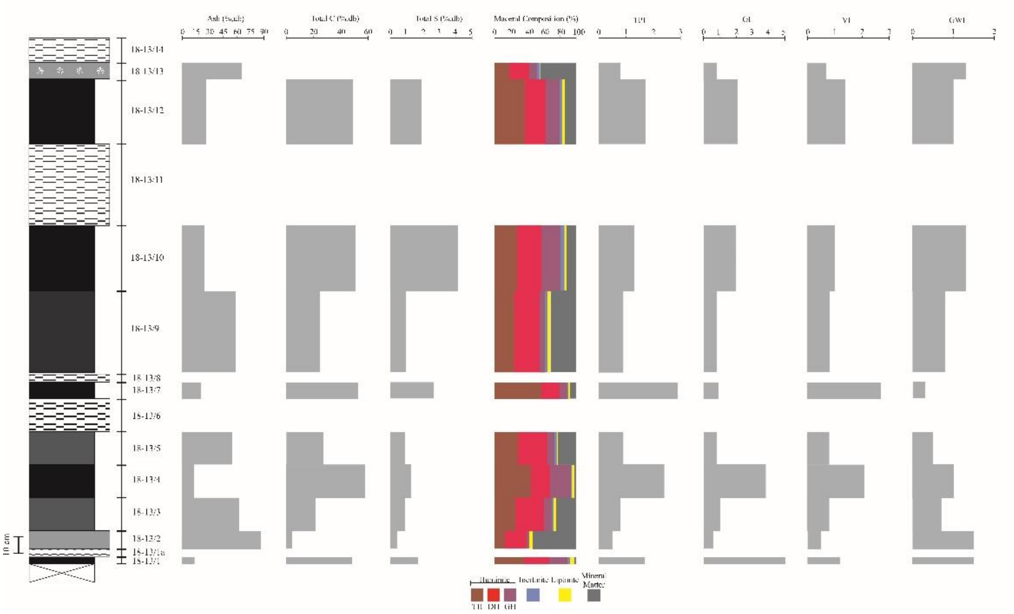

Figure 4: Vertical distrubition of ash, total C and S, macearal compositions and coal facies indicies through sampling profile (for legend of lithostratigraphic column, see Figure 3).

Şekil 4: *İncelenen örneklere ait kül, toplam C ve S, maseral içerikleri ve kömür fasiyes parametrelerinin örnekleme profil boyunca düşey dağılımı (litostratigrafik sütun kesitin açıklaması için Şekil 3'bakınız).*

Coal Petrography

Huminite is the predominant maceral group in the coal samples, while liptinite and inertinite group macerals display variable proportions (Table 2 and Figures 5 and 6). Telohuminite subgroup macerals are commonly identified in the samples (Figure 5). Ulminite is the most common telohuminite subgroup maceral in the samples (Figure 5a-b), whereas textinite has relatively higher proportions in xylite-rich lithotype samples (Figure 5a-b). Atrinite is a more common detrohuminite subgroup maceral in the mineral-rich lithotype coal, shale, and organic mudstone samples, and it is mostly observed within the clay mineral matrix (Figure 5c). Densinite displays relatively higher proportions in the xylite-rich lithotype coal samples, and sporinite and inertodetrinite are generally associated with densinite (Figure 5d). Corpohuminite is the predominant gelohuminite subgroup maceral in the coal samples and has significantly higher proportions in xylite-rich litotype coal samples (Table 2). Corpohuminite is mostly identified as corpohuminite accumulation and cell-lumen infillings of textinite (Figure 5a, b and e).

Levigelinite is another common gelohuminite subgroup maceral, while porigelinite is rarely identified within the cell-lumens of textinite (Figure 5f).

Table 1: The results of proximate, ultimate and calorific analyses of studied coal and shale samples (GCV: gross calorific value; as-rec.: as received basis; db: on dry basis; XC: xylite-rich lithotype; XCD: xylo-detritic sub-lithotype; MRC: mineral-rich lithotype; CS: carbonaceous shale, OM: organic mudstone, na: not available, *oxygen content is calculated by subtraction [O = 100 − (C + H + S + N + ash)] on dry basis)).

Çizilge 1: *İncelenen kömür ve şeyl örneklerine ait kaba kimyasal ve elementer ile kalorifik analizlere ait sonuçlar (GCV: üst ısıl değer; as-rec.: orijinal baz; db: kuru baz; XC: ksilitçe zengin litotip; XCD: ksilo-detritik altlitotip; MRC: mineralce zengin litotip; CS: karbonlu şeyl, OM: organik çamurtaşı, na: veri yok, * oksijen içeriği kuru bazda O = 100 − (C + H + S + N + kül) formülüne göre hesaplanmıştır).*

Sample	Lithotype/ Lithology	Moisture wt%, as-rec	Ash	VM	GCV kcal/kg, db	C	H	N	S	O*
			wt%, db					wt%, db		
18-13/13	OM	20.8	65.5	28.5	1472	na	2.4	0.4	na	na
18-13/12	XC	29.7	26.7	39.6	4800	48.9	4.2	1.4	1.9	17.0
18-13/10	XC	21.4	24.7	41.9	4913	50.8	4.2	1.4	4.1	14.8
18-13/09	XCD	20.5	58.8	25.5	2480	24.6	3.3	0.8	0.9	11.6
18-13/07	XC	27.5	21.1	40.0	5192	52.5	4.4	1.1	2.7	18.2
18-13/05	MRC	22.5	55.4	26.2	2667	27.2	3.2	0.8	0.9	12.4
18-13/04	XC	30.2	13.2	43.0	5637	57.8	4.5	1.8	1.3	21.4
18-13/03	MRC	20.7	63.0	24.3	3752	21.2	3.0	0.7	0.9	11.2
18-13/02	CS	18.6	86.7	12.2	na	4.5	2.2	0.2	0.4	6.0
18-13/01	XC	32.2	13.7	42.9	5663	57.6	4.6	1.9	1.7	20.5

Liptodetrinite and sporinite, which are associated with detrohuminite macerals, are the common liptinite group macerals, while cutinite, resinite, and alginite are rarely observed (Table 2 and Figure 6a-b). Inertinite displays low proportions in the samples (<3.0% on the whole coal-basis), and inertodetrinite and funginite, with variable morphologies, are the main inertinite group macerals (Figures 5d and 6c). Furthermore, funginites are identified during SEM studies (Figure 7). Since the Danişmen Formation is known for its rich fungal flora (Çelik et al., 2017; Ediger, 1981; Ediger and Alişan, 1989; Elsik et al., 1990), the diverse morphologies of funginite are expected. Similar observations have been reported in other coal seams within the Malkara coalfield (Karayiğit et al., 2022a), where fusinite and semifusinite are barely identified. Mineral matter contents vary (2.2–53.8% on a whole-coal basis), and mineral matter identified under incident white light include clays, framboidal pyrite grains (individual or aggregates), cleat/fracture pyrite infillings, syngenetic carbonate bands, siderite nodules, and quartz grains (Figures 5c and 6 d-f). Furthermore, calcareous fossil shell remains are also observed. In comparison with other coal mining areas in the Malkara coalfield (Karayiğit et al., 2022a), the studied samples display similar maceral compositions. As can be seen in the mineralogy section, syngenetic carbonate bands and siderite nodules are less common, and replacement carbonates were not observed in the Seam-VI.

The mean %Rr values of analysed samples are ranging between 0.40±0.02% and 0.41±0.01% (Table 2). These values are close to reported mean %Rr values from other coal mining areas in the Malkara coalfield (Karayiğit et al., 2022a), and slightly higher than the %Rr values of other coalfields (e.g., Pınarhisar and Yeniköy) close to Standrja massif (Çelik et al., 2017; Erarslan and Örgün, 2017).

Table 2: Maceral composition of studied coal and shale samples (vol.%, on whole basis), mean random huminite reflectance (%Rr) values of coal samples (Stdv: standard deviation).

Çizelge 2: *İncelenen kömür ve şeyl örneklerine ait maseral içerikleri (tüm bazda, hacimsel %) ve kömür örneklerine ait ortalama hüminit yansıtma (%Rr) değerleri (Stdv: standart sapma).*

Maceral	Sample									
	18-13/1	18-13/2	18-13/3	18-13/4	18-13/5	18-13/7	18-13/9	18-13/10	18-13/12	18-13/13
Textinite	11.6	0.5	2.8	16.7	8.2	27.4	5.1	10.5	13.1	2.4
Ulminite	25.1	12.3	22.2	28.4	20.3	30.5	19.0	17.1	23.8	15.2
Telohüminite	*36.8*	*12.8*	*25.0*	*45.2*	*28.5*	*57.9*	*24.1*	*27.6*	*36.9*	*17.6*
Attrinite	0.6	25.8	31.9	2.0	31.1	18.7	27.0	12.4	10.6	24.7
Densinite	29.9	0.3	3.1	20.6	5.2	3.0	4.0	17.3	15.6	0.7
Detrohüminite	*30.5*	*26.1*	*35.0*	*22.7*	*36.3*	*21.6*	*31.0*	*29.7*	*26.1*	*25.5*
Levigelinite	1.8	1.3	3.6	5.0	2.2	0.5	1.6	4.4	2.8	3.0
Porigelinite	0.4				0.2	0.9	0.1	0.3		0.3
Corpohuminite	20.0	1.7	6.2	20.8	6.1	8.0	4.6	17.9	14.2	5.6
Gelohüminite	*22.2*	*3.0*	*9.8*	*25.8*	*8.5*	*9.4*	*6.3*	*22.7*	*17.0*	*8.9*
Huminite	***89.5***	***41.9***	***69.8***	***93.7***	***73.3***	***89.0***	***61.4***	***80.0***	***79.9***	***52.0***
Fusinite	0.4		0.4		0.7		0.2	0.3	0.3	0.3
Inertodetrinite	1.3	0.4	0.3	0.0	0.3	0.0	0.5	1.1	0.8	0.7
Funginite	1.5	0.2	1.4	1.1	1.6	0.9	2.6	2.7	1.7	1.6
Semifüsinite						0.2	0.4	1.1		0.3
Inertinite	***3.1***	***0.6***	***2.1***	***1.1***	***2.7***	***1.0***	***3.7***	***5.2***	***2.8***	***2.9***
Sporinite	2.6	1.5	1.9	1.5	0.6	0.9	1.4	1.3	1.9	0.2
Cutinite	0.4	0.3		0.9	0.0	0.0		0.3		
Resinite	0.4	0.1		0.4	0.1	0.7	0.4	0.6	0.6	
Alginite	0.4	0.3			0.1				0.2	0.1
Liptodetrinite	1.3	1.5	1.0	0.2	0.7	0.9	1.6	0.6	1.1	0.4
Liptinite	***5.0***	***3.7***	***2.9***	***3.0***	***1.6***	***2.4***	***3.3***	***2.9***	***3.7***	***0.7***
Mineral Matter	***2.4***	***53.8***	***25.2***	***2.2***	***22.4***	***7.5***	***31.5***	***11.6***	***13.5***	***44.3***
Mean %Rr				0.41				0.40	0.40	
Stdv (±)				0.01				0.01	0.02	

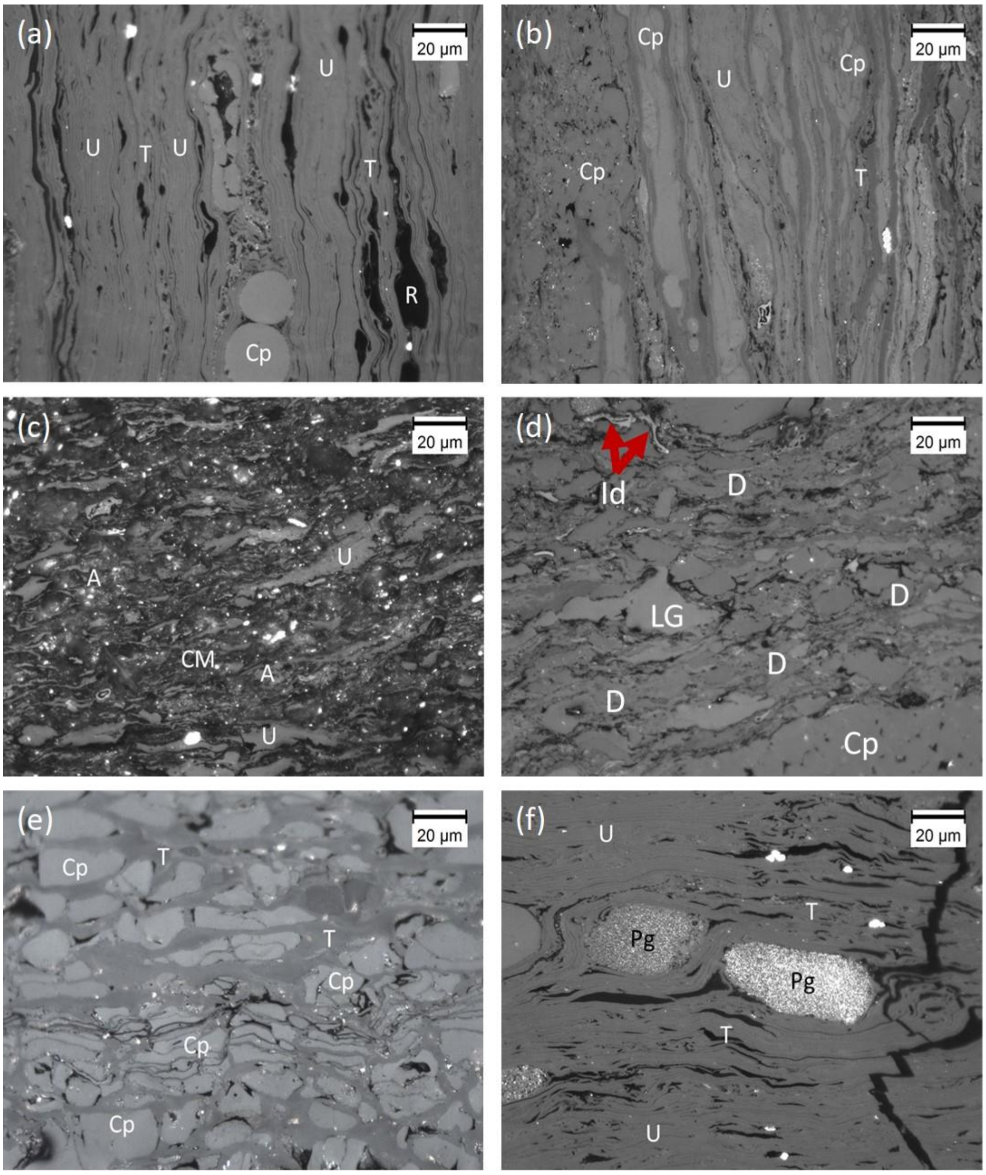

Figure 5: Photomicrographs of coal and shale samples from the Seam-VI. All photomicrographs are taken under incident white light (a-f), oil immersion, 500 × total magnification. A: attrinite, CM: clay minerals, Cp: corpohuminite, D: densinite, Id: inertodetrinite, Pg: porigelinite, R: resinite, LG: levigelinite, T: textinite, U: ulminite.

Şekil 5: *Damar-VI'dan alınan kömür ve şeyl örneklerinin fotomikrografları. Bütün mikrofotograflar üstten aydınlatmalı normal ışık kullanılarak (a-f), 500× toplam büyütmeli yağlı objektifte çekilmiştir. A: atrinit, CM: kil mineralleri, Cp: korpohüminit, D: densinit, Id: inertodetrinit, Pg: porigelinit, R: resinit, LG: levigelinit, T: tekstinit, U: ülminit.*

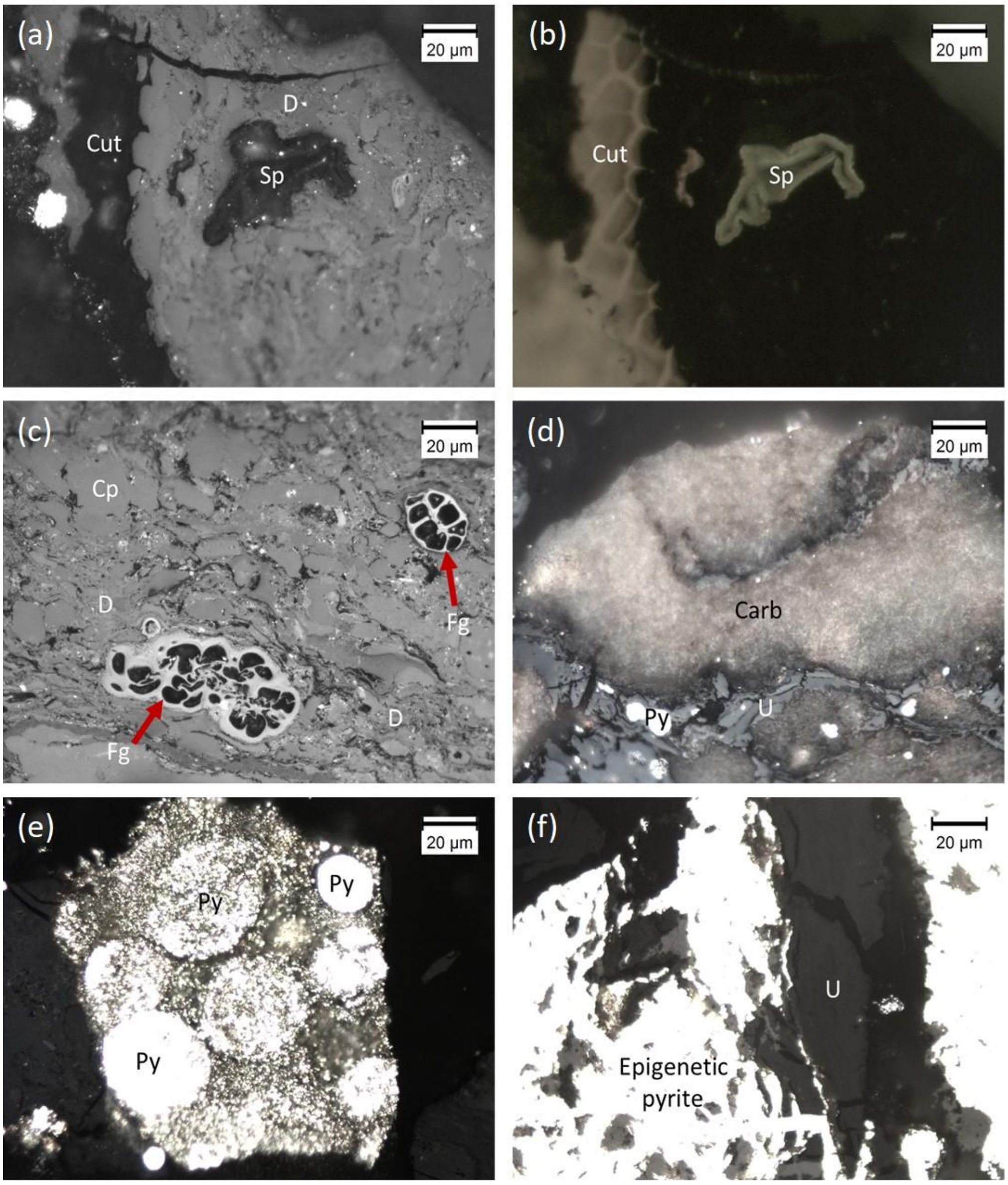

Figure 6: Photomicrographs of coal and shale samples from the Seam-VI. All photomicrographs are taken under incident white light (a,d-f) and blue-light excitation (b), oil immersion, 500 × total magnification. Carb: carbonate mineral, Cp: corpohuminite, Cut: cutinite, D: densinite, Fg: funginite, Py: pyrite, Sp: sporinite, U: ulminite.

Şekil 6: *Damar-VI'dan alınan kömür ve şeyl örneklerinin fotomikrografları. Bütün mikrofotograflar üstten aydınlatmalı normal ışık (a, c-f) ve UV mavi ışık (b) kullanılarak, 500× toplam büyütmeli yağlı objektifte çekilmiştir. Carb: karbonat minerali, Cp: korpohuminit, Cut: kütinit, D: densinit, Fg: funginit, Py: pirit, Sp: sporinit, U: ülminit.*

Table 3: Semi-quantitative mineralogical composition of the studied coal and non-coal samples based on XRD and SEM-EDX analyses (+++ = dominant phase (> 30%), ++ = abundant phase (5-30%), + = minor phase (< 5%) by XRD, a: accessory mineral detected by SEM-EDX) (Abbreviations: XC: xylite-rich lithotype; XCD: xylo-detritic sub-lithotype; MRC: mineral-rich lithotype; CS: carbonaceous shale, OM: organic mudstone, Ap: apatite, Brt: barite, Dol: dolomite, Feld: feldspars, Pnt: pentlandite, Sph: sphalerite and Zrn: zircon).

***Çizelge 3**: XRD ve SEM-EDX analizlerine göre incelenen kömür ve kömür dışı örneklere ait yarı kantitatif mineralojik bileşimleri (XRD analizlerine göre +++ = baskın faz (> 30%), ++ = bol faz (5-30%), + = minör faz (< 5%), a: SEM-EDX tarafından tespit edilen aksesuar faz) (Kısaltmalar; XC: ksilitçe zengin litotip; XCD: ksilo-detritik altlitotip; MRC: mineralce zengin litotip; CS: karbonlu şeyl, OM: organik çamurtaşı; Ap: apatit, Brt: barit, Dol: dolomit, Feld: feldspatlar, Pnt: pentlandit, Sph: sfalerit ve Zrn: zirkon).*

Sample	Lithotype/ Lithology	Quartz	Clay minerals	Feld	Biotite	Zrn	Calcite	Dol	Aragonite	Siderite	Pyrite	Sph	Pnt	Brt	Ap	Ti-oxide
18-13/14	Claystone	++	+++	+			++	+		+	+					
18-13/13	OM	++	+++	++			++		++		+					
18-13/12	XC	++	+++	++							+					
18-13/11	Claystone	++	+++	+			+	+			+					
18-13/10	XC	++	+++	a			a	a	++		++	a			a	
18-13/09	XCD	+++	+++	++			+									
18-13/08	Claystone	++	+++				++	+		+						
18-13/07	XC	++	+++								++					
18-13/06	Claystone	++	+++	+			++	++								
18-13/05	MRC	++	+++	+++												
18-13/04	XC	+++	+++	a	a	a		a		a	+			a	a	
18-13/03	MRC	++	+++	++	a		a				+		a	a	a	a
18-13/02	CS	++	+++	++												
18-13/01	XC	+++	+++								+					
18-13/01a	Claystone	++	+++	+				++			+					

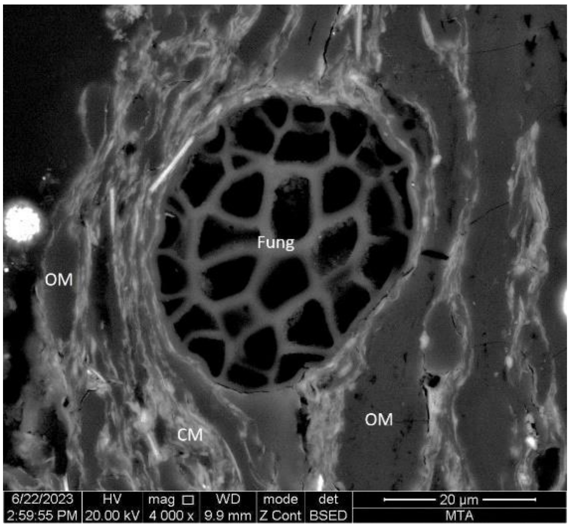

Figure 7: SEM backscattered image of funginite. CM: clay mineral, Fung: funginite, OM: organic matter.

Şekil 7*: Funginit maseraline ait SEM geri saçılım görüntüsü. CM: kil minerali, Fg: fungini, OM: organik madde.*

Mineralogy

The minerals identified using XRD-whole rock analysis are clay minerals, quartz, pyrite, calcite, dolomite, and feldspars (Table 3). Siderite is identified from one coal sample (18-13/08) and rock sample (18-13/14), whereas it is identified as an accessory phase from one coal sample (18-13/04). Aragonite is detected in two samples (18-13/10 and /13), both of which contain fossil shell remains (Table 5). The SEM observations agree with XRD data, and apatite, barite, biotite, pentlandite, sphalerite, Ti-oxide, and zircon are also determined as accessory phases in the coal samples (Table 3).

Clay minerals are the dominant phases in all studied samples (Table 3), and the identified clay minerals are smectite, illite, chlorite, and kaolinite according to XRD-CF data. Quartz is mostly an abundant phase, and in a few samples, it is the dominant phase. Feldspars are present as minor to abundant phases in mineral-rich lithotype coals and some intercalation samples (Table 3). Calcite and dolomite are present as minor to abundant phases in inorganic samples, while calcite is detected as a minor to accessory phase in coal samples (Table 3). As mentioned above, aragonite is detected as an abundant phase in fossil shell remains-bearing samples. Pyrite is mostly a minor phase in the samples, and it is commonly abundant phase in xylite-rich lithotype coal samples (Table 3).

Geochemistry

The major oxide contents of the analysed ashed samples vary (Table 4), and the SiO_2, Al_2O3 and K_2O contents of mineral-rich lithotype coal samples, carbonaceous shale, and organic mudstone samples are generally higher than those of xylite-rich lithotype coal samples. In contrast, xylite-rich lithotype coal samples display relatively higher CaO and Fe_2O_3 contents (Table 4). These differences could be related to the existence of clay mineral bands in the mineral-rich lithotype coal samples, carbonaceous shale, and organic mudstone samples, as well as possibly organically bound Ca in xylite-rich samples. Additionally, there are not any significant differences in Na_2O, MgO, and TiO_2 contents among the samples. These factors could also explain the lack of well-defined vertical variations in major oxide contents throughout the sampling profile (Figure 8a).

The average concentrations on a whole-coal basis of B, P, Mn, Sr, and Ba in coal and carbonaceous shale (e.g.18-13/02) samples are higher than 100 ppm, while the average concentrations of Li, V, Cr, Ni, Cu, Zn, Ge, and Mo in are between 10 to 100 ppm (Tables 4 and 5). The remaining elements in the coal samples display average concentrations on a whole-coal basis lower than 10 ppm (Tables 4 and 5). In order to determine elemental enrichments in the studied profile, concentration coefficient (CC) were calculated according to Dai et al. (2015). These calculations are based on dividing the average concentrations of coal and shale samples by Clarke values for low-rank coals and sedimentary rocks reported in Ketris and Yudovich (2009). The calculated CC values for coal samples indicate significant enrichments for Mn (CC=14.9) and Ni (CC=10.8), while Ge (CC=7.2) and Mo (CC=5.4) are classified as enriched (Table 5). The slightly enriched elements in the coal samples are B (CC=2.3), Cr (CC=2.8), Co (CC=2.1), and Sr (CC=3.0). The CC values for Li, P, Sc, V, Cu, Zn, As, Y, Cd, Ba, and Pb are close to low-rank coal averages (0.5<CC<2.0), whereas the remaining elements are depleted (CC<0.5).

DISCUSSIONS

Coal Rank

The rank determination of coals is mostly based on mean %Rr values; nevertheless, the sole usage of this parameter, particularly for Cenozoic coals, does not provide a proper rank estimation (O'Keefe et al., 2013). In some cases, the %Rr values of ulminite B macerals in xylite-rich coals could be suppressed due to the existence of H-rich compounds in peat-forming plants (Çelik et al., 2017; Papanicolaou et al., 2000; Sykes et al., 1994). Like the other coal seams within the Malkara coalfield (Karayiğit et al., 2022a), H contents display a moderately positive correlation with total telohuminite contents. Therefore, the mean %Rr values of the coal samples from the İbrice area should be combined with ash yields and gross calorific values in order to have better rank estimations. The mean %Rr values, along with ash yields and gross calorific values of the studied samples, show that xylite-rich lithotype coal samples are medium to high-grade low-rank A based on the ECE-UN (1988) classification and low- to medium-ash low-rank A based on the ISO 11760 (2005) classification. As expected, mineral-rich lithotype coal samples are low- to medium-grade low-rank B and medium- to high-ash low-rank A according to the ECE-UN (1988) and ISO 11760 (2005) classifications, respectively.

As mentioned previously, the studied samples have relatively lower mean %Rr values than working coal seams in the Hasköy, Şahin, and Pirinççeşme areas in the Malkara coalfield. Although the difference is not high, these differences could be related to the relatively deeper recent burial depths of the working coal seams in the Hasköy, Şahin, and Pirinççeşme

Table 4: Elemental composition of the studied coal (on whole coal basis) and shale samples (on whole rock-basis). All results in ppm, expect otherwise cited (Abbreviations: XC: xylite-rich lithotype; XCD: xylo-detritic sub-lithotype; MRC: mineral-rich lithotype; CS: carbonaceous shale, OM: organic mudstone, na: not available).

Çizelge 4: *İncelenen kömür (tüm kömür bazında) ve şeyl örnekerlerinin (tüm kayaç bazında) elementel içerikleri. Bütün sonuçlar ppm olarak sunulmuştur, aksi taktirde belirtilmiştir (Kısaltmalar: XC: ksilitçe zengin litotip; XCD: ksilo-detritik altlitotip; MRC: mineralce zengin litotip; CS: karbonlu şeyl, OM: organik çamurtaşı, na: veri mevcut değil).*

Element	18-13/1	18-13/2	18-13/3	18-13/4	18-13/5	18-13/7	18-13/9	18-13/10	18-13/12	18-13/13
Lithotype/ Lithology	XC	CS	MRC	XC	MRC	XC	XCD	XC	XCD	OM
SiO_2 (%)	28.9	61.9	56.5	30.5	55.9	38.3	58.1	31.5	47.5	48.7
TiO_2 (%)	0.68	0.68	0.78	0.59	0.80	0.63	0.74	0.57	0.92	0.59
Al_2O_3 (%)	14.0	19.6	19.0	12.6	19.6	15.8	18.7	14.2	17.7	15.4
Fe_2O_3 (%)	11.0	7.4	8.4	11.0	8.6	17.9	8.3	18.0	9.0	6.4
MgO (%)	6.5	4.8	5.2	7.5	5.3	4.5	5.0	4.2	4.6	4.1
CaO (%)	13.9	0.7	3.2	15.2	2.2	7.1	1.9	12.6	6.6	18.5
Na_2O (%)	1.5	1.0	1.1	1.7	1.2	1.0	1.0	0.9	1.1	0.9
K_2O (%)	0.5	2.7	2.9	1.5	2.8	1.6	2.8	1.3	2.1	1.8
Li	2.6	7.9	13.1	2.1	14	6.6	21	6.1	19	8.3
Be	1.7	0.24	0.47	0.61	0.47	0.41	0.49	0.78	0.77	0.58
B	137	38	72	153	93	197	66	143	141	50
P	78	254	392	195	514	191	210	375	213	354
Sc	1.4	3.9	6.5	2.6	5.8	3.5	4.4	3.3	4.4	4.0
V	8.6	44	50	14	42	26	30	18	49	33
Cr	7.1	50	81	16	63	27	71	24	24	56
Mn	31	115	13701	42	118	49	213	68	53	345
Co	2.1	11	17	3.1	19	8.6	9.1	5.7	7.2	8.9
Ni	30	157	199	18	184	75	106	72	54	100
Cu	6.6	26	25	6.6	22	7.3	19	8.3	15	19
Zn	8.0	75	76	11	60	19	55	18	32	45
Ge	5.3	17	19	5.4	17	13	15	17	8.6	14
As	3.7	3.7	9.1	2.1	2.3	4.1	1.1	11	4.6	13
Sr	338	217	344	370	342	306	323	498	403	616
Y	8.2	5.9	8.9	6.6	11.2	7.1	6.3	11.1	9.8	9.1
Zr	9.4	4.2	10	3.9	41	7.5	5.8	4.8	20	7.7
Nb	0.5	3.1	4.2	1.2	7.5	2.3	1.5	0.9	5.0	2.3
Mo	7.4	15	14	5.8	13.1	7.5	22	8.9	21	7.4
Cd	0.16	0.33	0.36	0.13	0.94	0.23	0.32	0.29	na	0.26
Ba	172	107	178	198	178	171	169	256	218	174
Pb	1.9	14	17	2.4	10	4.8	10	3.4	5.9	10

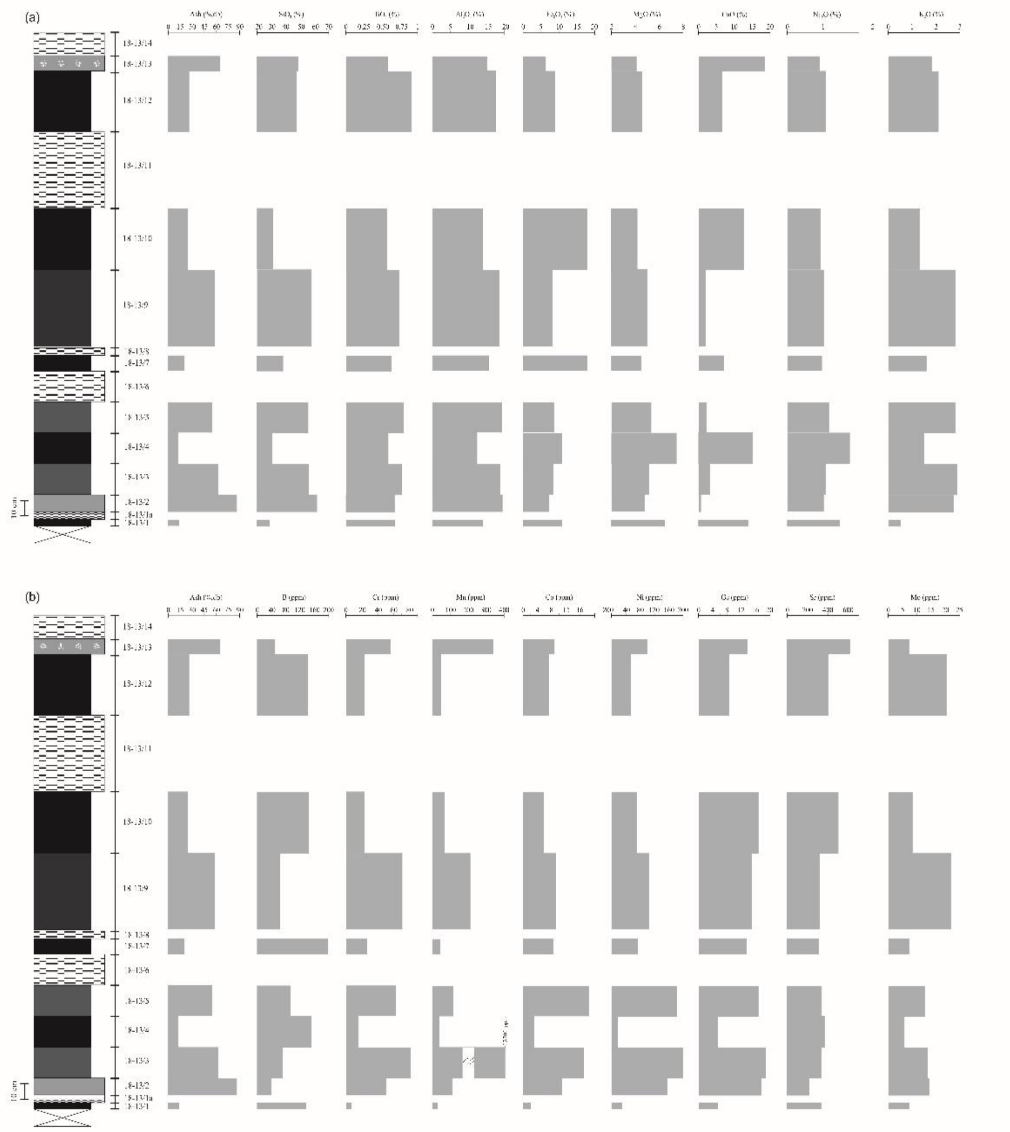

Figure 8: Vertical distrubition of (a) ash yield, SiO_2, TiO_2, Al_2O_3, CaO, Fe_2O_3, K_2O, MgO, and Na_2O; (b) B, Cr, Mn, Co, Ni, Ge, Sr and Mo (for legend of lithostratigraphic column, see Figure 3).

Şekil 8: *(a) kül, SiO_2, TiO_2, Al_2O_3, CaO, Fe_2O_3, K_2O, MgO ve Na_2O ile (b) B, Cr, Mn, Co, Ni, Ge, Sr and Mo elementlerin örnekleme profili boyunca düşey dağılımı (litostratigrafik sütun kesitin açıklaması için Şekil 3'bakınız).*

Table 5: Weighted average of the minor and trace elements (in ppm) for the coal samples from the Seam-VI in the İbrice area, and their comparison with Clarke values for low-rank coals (a: from Ketris and Yudovich (2009)). Elements in bold are enriched.

Çizelge 5: *İbrice sahasındaki Damar-VI'ya ait kömür örneklerinin ağırlıklı ortalamaları ve ortalamaların düşük kömürleşme derecesine sahip kömürlere ait Clarke değerleriyle karşılaştırılmaları (a: Ketris and Yudovich (2009)'dan alınmıştır). Koyu renkle belirtilen element değerleri zenginleşme sunmaktadır.*

Element	Clarke values for low-rank coals[a]	İbrice coal samples	Concentration coefficent (CC)
Li	10	10	1.0
Be	1.2	0.55	0.5
B	56	126	**2.3**
P	200	272	1.4
Sc	4.1	4.0	1.0
Ti	720	338	0.5
V	22	28	1.3
Cr	15	42	**2.8**
Mn	100	1493	**14.9**
Co	4.2	8.9	**2.1**
Ni	9	97	**10.8**
Cu	15	14	0.9
Zn	18	36	2.0
Ge	2	14	**7.2**
As	7.6	5.1	0.7
Sr	120	357	**3.0**
Y	8.6	8.0	0.9
Zr	35	8.1	0.2
Nb	11	2.2	0.2
Mo	2.2	12	**5.4**
Cd	0.24	0.31	1.3
Ba	150	188	1.3

areas than the İbrice area. Nevertheless, like other seams in the Malkara coalfield, Seam-VI displays higher mean %Rr values than working coal seams in the northern parts of the Thrace Basin (e.g., Yeniköy and Pınarhisar coalfields). According to thermal 1-D modelling, based on the mean %Rr values of Eocene and Oligocene formations in the oil and gas production fields in the Thrace Basin, major vertical tectonic movement from the Miocene to the Pliocene caused deeper burial depths in the central and southern parts of the basin (Huvaz et al., 2007). Furthermore, the thermal gradient around the central and southern parts of the basin was higher than the northern parts. Hence, as reported earlier by Karayiğit et al. (2022a), the differences in mean %Rr values of working coal seams between the study area and the northern parts of the Thrace Basin are expected.

Origin of Minerals

To determine the mode of occurrence of minerals in coal could provide data about water chemistry, redox, salinity, and hydrogeological conditions during the precursor peat accumulation, as well chemistry of circulating fluids during coalification (Dai et al., 2020a; Ward, 2002, 2016). The XRD and SEM-EDX data of the coal and carbonaceous shale samples could imply that the identified minerals are mainly detritic and authigenically precipitated during peatification and/or early diagenetic stages, with a lesser extent of epigenetic precipitation during coalification (Table 6). Clay minerals are observed as matrices of clay mineral aggregates (Figure 9a-c), which are associated with quartz, feldspars, apatite, biotite, chlorite, pentlandite, sphalerite, Ti-oxide, and zircon grains, during petrographic and SEM-EDX studies.

Table 6: Syngenetically and epigenetically formed minerals identified using XRD and SEM-EDX in the coal and carbonaceous shale samples. Solid line indicates clearly identified minerals in the samples, dashed line shows possible identifications.

Çizelge 6: *XRD ve SEM-EDX yardımıyla incelenen kömür ve karbonlu şeyl örneklerindeki sinjenetik ve epijenetik olarak oluşan mineraller. Kesiksiz çizgiler tanımlanan minerallerin örneklerdeki ana kökenlerini ve kesikli çizgiler ise tanımlanan minerallerin olası kökenlerini işaret etmektedir.*

Minerals	Syngenetic		Epigenetic	
	Detritus	Authigenic precipitation in peat	Authigenic precipitation at depth	Authigenic weathering reactions
Quartz	———	– – –	– – –	
Clay minerals	———	– – –		
Feldspars	———			
Biotite	———			
Zircon	———			
Calcite/Aragonite	– – –	———		
Siderite		———		
Dolomite	– – –			
Pyrite		———	– – –	
Sphalerite	———			
Pentlandite	———			
Barite		———	– – –	– – –
Apatite	———	– – –		
Ti-oxides	———			

The SEM-EDX data also show that the matrices of clay aggregates are mainly illitic and smectite compositions. Ilitic clay mineral aggregates in coals are generally related to clastic influx into paleomires from adjacent areas (Oskay et al., 2016; Ward, 2002), while clay mineral aggregates with smectite composition could be related to alteration of synchronous and/or epiclastic volcanic inputs due to the presence of tuffite layers within the Oligocene formations in the study area (Dai et al., 2017; Karayiğit et al., 2017; Spears, 2012). The existence of quartz, feldspars, biotite, Ti-oxide, and zircon grains within such matrices may also be an indicator of synchronous and/or epiclastic volcanic inputs into palaeomires (Bohor and Triplehorn, 1993; Dai et al., 2017). Nevertheless, these aggregates could also be derived from the alteration of clastic influx from the basement. The existence of Fe-rich chlorite grains (chamosite) with lath shapes (Figure 9b) could suggest that these grains could be derived from the alteration of detrital inputs from the basement rocks within palaeomires. Overall, clay minerals in the Seam-VI seem to be mainly derived as clastic influx into paleomires, with a lesser extent of authigenic formation during peat accumulation and/or late stages of peatification.

Quartz/silica is mostly identified as individual grains and/or associated with clay minerals aggregates (Figure 9c-d). Considering the presence of tuffite layers in the Oligocene formations in the basin and the presence of metamorphic rocks in the basement, it can be concluded that quartz/silica grains have a detrital origin (Ward, 2016). Furthermore, quartz/silica cavity and cell-infillings within telohuminite macerals and cleat/fracture quartz/silica infillings were rarely observed in the studied samples. The former quartz/silica infillings could be related to re-precipitation of liberated Si from plant decay or the alteration of clastic inputs within palaeomires and/or early diagenetic stages (Ward, 2002); on the other hand, cleat/fracture quartz/silica infillings could originate from precipitation of Si-rich porewater and/or leached solutions from overlying sandstone layers within the Danişmen Formation during late diagenesis/coalification. Like quartz/silica, feldspar grains (plagioclase and K-feldspars) are observed either as individual grains or within clay mineral aggregates. The variable size and irregular edges of feldspar grains (Figure 9e-f) could imply that these grains are derived by clastic influx into the palaeomire from different sources (Dai et al., 2017; Karayiğit et al., 2022c). For instance, the presence of zircon within the cavities of feldspar grains (Figure 9f) could be derived from tuffite layers within the Oligocene formations; nevertheless, the presence of barite overgrowths around feldspar grains could suggest that these grains were altered within the palaeomires (Çelik et al., 2021).

Carbonate minerals in coal samples are mostly observed as carbonate mineral bands (Figure 10a-c) and rarely as individual grains within clay mineral aggregates. Furthermore, fossil shell remains in $CaCO_3$ compositions were identified in the samples bearing fossil shell remains (Figure 10d-e) as well as in siderite micronodules (Figure 10f). It is well documented from the Turkish Cenozoic coals that Ca-rich alkaline aquifer support into palaeomires resulted in the formation of authigenic carbonate mineral bands and siderite micronodules during peatification and/or early diagenetic stages (Karayiğit et al., 2017, 2022b, 2022c; Kortenski, 1992). Such conditions could also cause the formation of alkaline conditions within the palaeomire. Siderite micronodules in coal are generally considered evidence for low sulphur contents in the palaeomire (Dai et al., 2020a; Shen et al., 2023); however, the presence of pyrite and syngenetic carbonate-pyrite associations (Figure 10c) in the same samples could suggest that dissolved Fe might be high in mire water and/or weak acidic to neutral conditions were developed during the peat accumulation (Karayiğit et al., 2017, 2022b, 2022c; Ward, 2016). As noted earlier from other coal mining areas in the Malkara coalfield (Karayiğit et al., 2022a), the co-occurrence of pyrite and syngenetic carbonate minerals could indicate the formation of weak acidic to neutral conditions. It is noteworthy to mention that no replacement carbonates were observed in the Seam-VI, like other seams in the Malkara coalfield, which indicates dissolved Ca concentrations in the paleomires of Seam-VI were not high as in the palaeomires of other

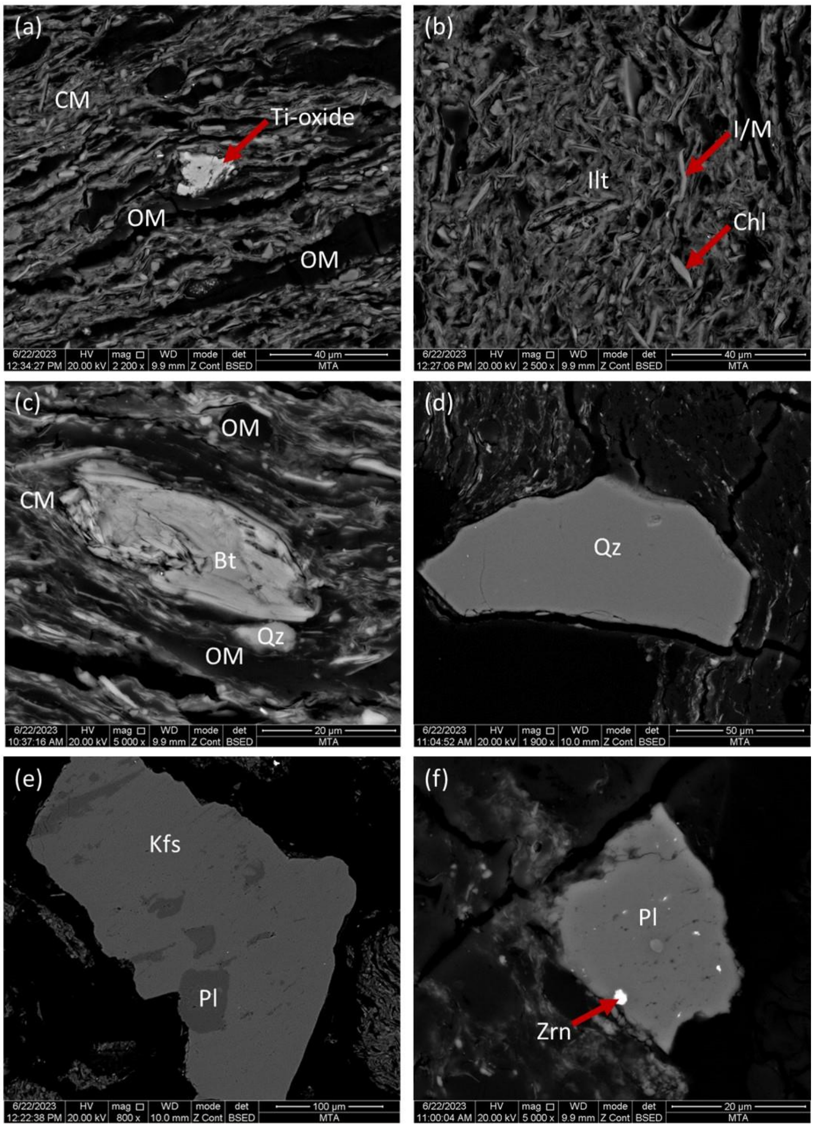

Figure 9: SEM backscattered images of crystalline phases in the studied coal and shale samples. (a-c) biotite (Bt), chlorite (Chl), illite/mica (I/M), Ti-oxide and quartz (Qz) grains associated with clay mineral (CM) matrix (illite: Ilt), and organic matter (OM); (d) individual quartz (Qz) grain; (e) plagioclase (Pl) associated with K-feldspar (Kfs) grain; (f) zircon (Zrn) within the cavities of plagioclase (Pl) grain.

Şekil 9: *İncelenen kömür ve şeyl örneklerdeki kristalin fazlara ait SEM geri saçılım görüntüleri. (a-c) kil mineralleri içerisindeki biyotit (Bt), illit/mika (I/M), klorit (Chl), kuvars (Qz) ve Ti-oksit taneleri ile organik madde (OM); (d) tekli kuvars (Qz) tanesi; (e) K-feldspat (Kfs) ile beraber gözlenen plajiyoklaz (Pl) tanesi; (f) plajiyoklaz (Pl) tanesi içerisindeki boşlukları içerisindeki zirkon (Zrn).*

seams in the Malkara coalfield. In addition, an increased Ca concentration and water level might also allow biogenic activities within the palaeomires (Ward, 2002); hence, calcareous shell remains are observed towards the upper parts of the Seam-VI.

Pyrite is the only identified sulphide mineral by XRD, while accessory sulphide minerals like sphalerite and pentlandite are detected during SEM studies (Table 6). The framboidal pyrite grains are the most common morphology, and partially pyritized calcareous fossil remains and cleat/fracture pyrite infillings are also observed in the samples (Figure 11a-c). The common presence of framboidal pyrite grains in coal seams is related to either marine influence into palaeomires and/or anoxic conditions within the palaeomires (Chou, 2012; Querol et al., 1989; Ward, 2016). The first possibly could not be applicable for the studied Seam-VI, since the detailed paleontological studies from the Malkara coalfield reported that the sequences bearing Seam-VI were deposited under flood plain and freshwater lakes (İslamoğlu et al., 2010; Şafak, 2019). Therefore, the development of anoxia seems to allow sulphate-reducing bacterial activity within the palaeomires (Chou, 2012). The formation of syngenetic framboidal pyrite grains could take place between pH 5.0 and 7.5 (Altschuler et al., 1983; Querol et al., 1989). As mentioned previously, the co-occurrence of pyrite and carbonate minerals implies that very weak acidic to neutral conditions were common during the peat accumulation. Apart from syngenetic pyrite grains, the partially pyritized calcareous fossil remains (Figure 10d-e) and cleat/fracture pyrite infillings (Figure 6f) could be formed from the replacement of carbonates by S-rich porewater and precipitation from S-rich solutions within cleat/fractures during the late diagenetic stage or coalification. Sphalerite and pentlandite grains have been identified within the clay mineral aggregates in the samples (Figures 12 and 13). Hence, the detritus origin for these sulphide minerals could be pronounced. The occurrence of pentlandite, along with chromite, in Turkish Cenozoic coals is mostly documented in the coalfields (e.g., Orhaneli and Tunçbilek) situated near ophiolitic rocks bearing Cr- and Ni- ore deposits (Karayiğit et al., 2019, 2021). On the contrary, no Cr- and Ni-ore deposits or mineralization were reported to date from ophiolitic rocks in the south-western parts of the Thrace Basin. Besides, sulphur mineralization and sulphide ore deposits were also reported from the Strandja and Rhodope massifs (Marchev et al., 2005; Mortiz et al., 2014; Taner and Çağatay, 1983). Considering the presence of pentlandite and sphalerite in these sulphide deposits, sphalerite and pentlandite in the samples are presumably derived from clastic influx into palaeomires from the Strandja and Rhodope massifs.

Barite and (Ba, Sr)-sulphates are the only identified sulphate minerals in the samples during the SEM studies (Table 6). They are commonly observed as overgrowth around the feldspar (Figures 11d and 14a) and or biotite grains (Figure 15a) and rarely as cleat/fracture infillings (Figure 11c). The barite overgrowths around feldspar or biotite grains could be related to the alteration of such grains within the palaeomires, and liberated Ba and Sr seem to be reduced by bacteria within the palaeomires (Çelik et al., 2021). Cleat/fracture barite infillings could be precipitated from Ba-bearing porewaters and/or leached solutions from the overlying sediments during coalification or post-coalification (Çelik et al., 2021; Dawson et al., 2012; Ward, 2016). Apatite is observed as individual grains within the clay minerals, which indicates a detritus

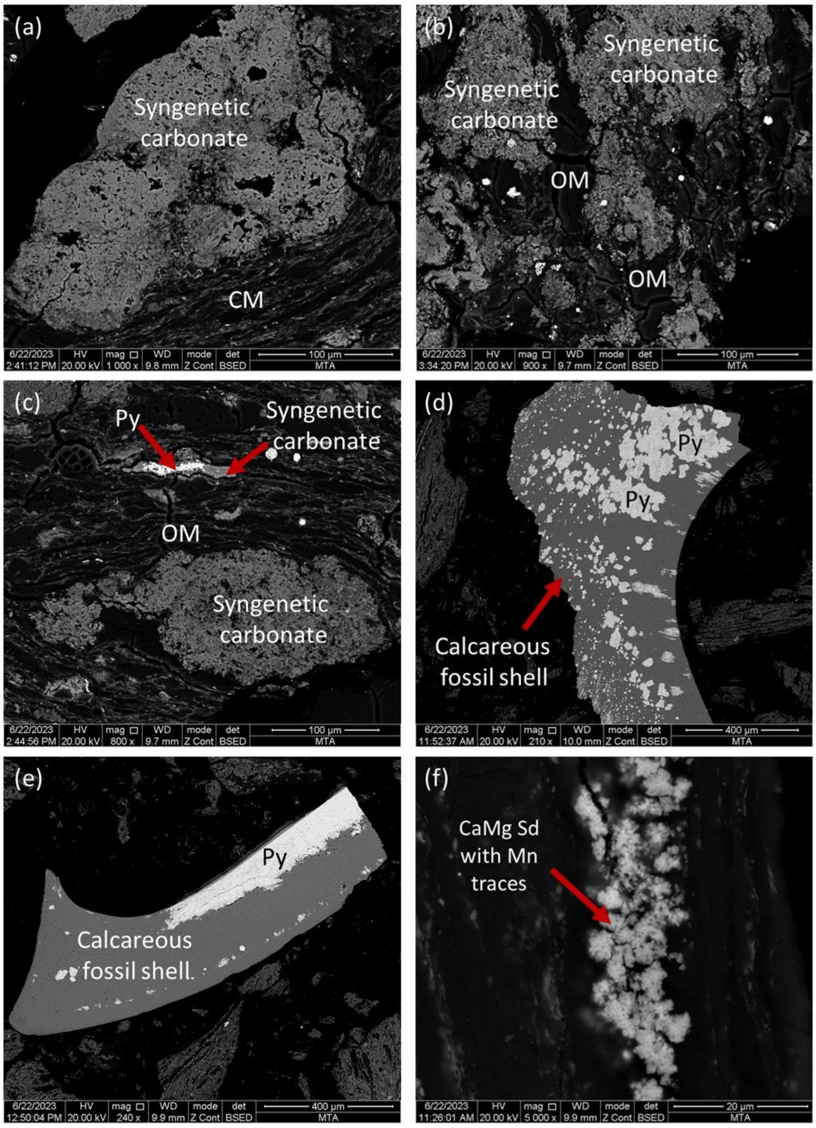

Figure 10: SEM backscattered images of crystalline phases in the studied coal and shale samples. (a-c) sygenetic carbonate mineral bands associated with organic matter (OM) and pyrite (Py), and clay minerals (CM); (d-e) partially pyritized (Py) calcareous fossil shell remains; (f) CaMg-siderite (Sd) micronodules with measurable Mn.

Şekil 10: *İncelenen kömür ve şeyl örneklerdeki kristalin fazlara ait SEM geri saçılım görüntüleri. (a-c) organik madde (OM) ile beraber gözlenen sinjenetik karbonat mineral bantları ile pirit (Py) ve kil mineralleri (CM); (d-e) kısmen piritleşmiş (Py) kalkerli fosil kavkı kalıntıları; (f) ölçülebilir miktarda Mn içeren CaMg-siderit nodülü.*

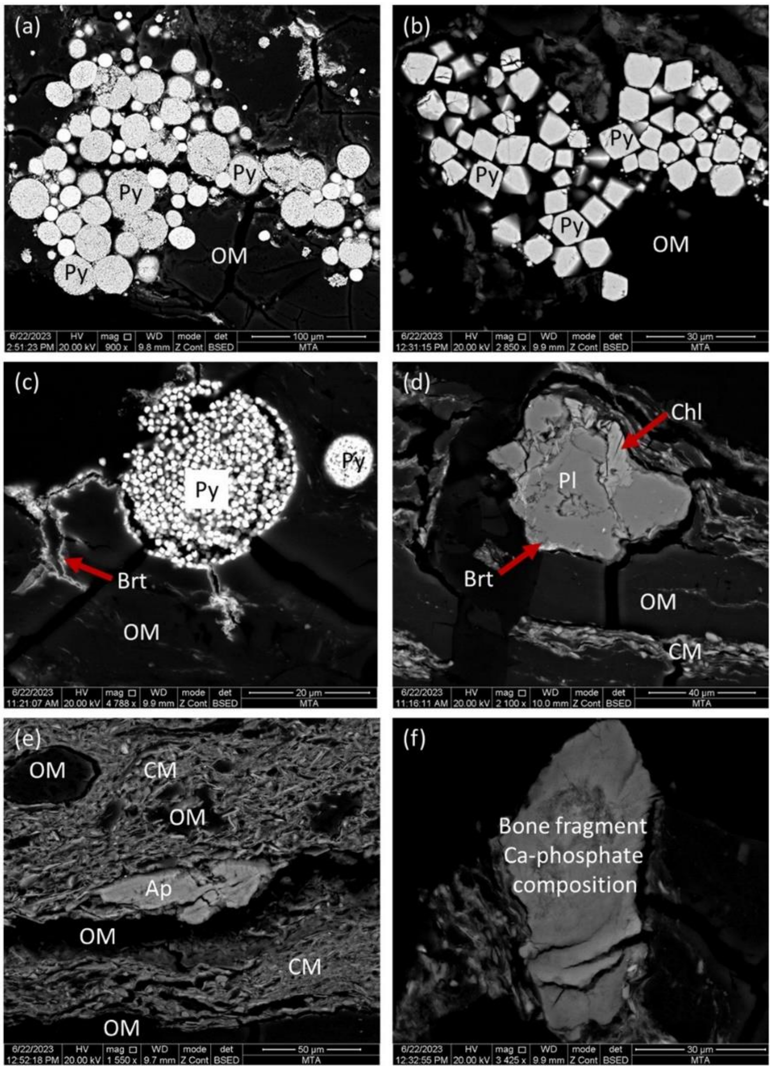

Figure 11: SEM backscattered images of crystalline phases in the studied coal and shale samples. (a) framboidal pyrite (Py) grains within organic matter (OM); (b) euhedral pyrite (Py) within organic matter (OM); (c) framboidal pyrite (Py) grains within organic matter, and cleat/fracture barite (Brt); (d) barite (Brt) overgrowths around plagioclase (Pl) grain, and chlorite (Chl), clay minerals (CM) and organic matter (OM); (e) apatite (Ap) associated with clay mineral (CM) aggregates, and organic matter (OM); (f) fossil bone fragment with Ca-phosphate composition.

Şekil 11: *İncelenen kömür ve şeyl örneklerdeki kristalin fazlara ait SEM geri saçılım görüntüleri. (a) organik madde (OM) içerisindeki framboidal piritler (Py); (b) organik madde (OM) içerisindeki özşekilli piritler (Py); (c) organik madde (OM) içerisindeki framboidal piritler (Py) ve kırık/çatlak dolgusu barit (Brt); (d) plajiyoklaz (Pl) tanesi etrafındaki barit (Brt) büyümleri, kil minerali (CM), klorit (Chl) ve organik madde (OM); (f) Ca-fosfat bileşimli fosil kemik kalıntısı.*

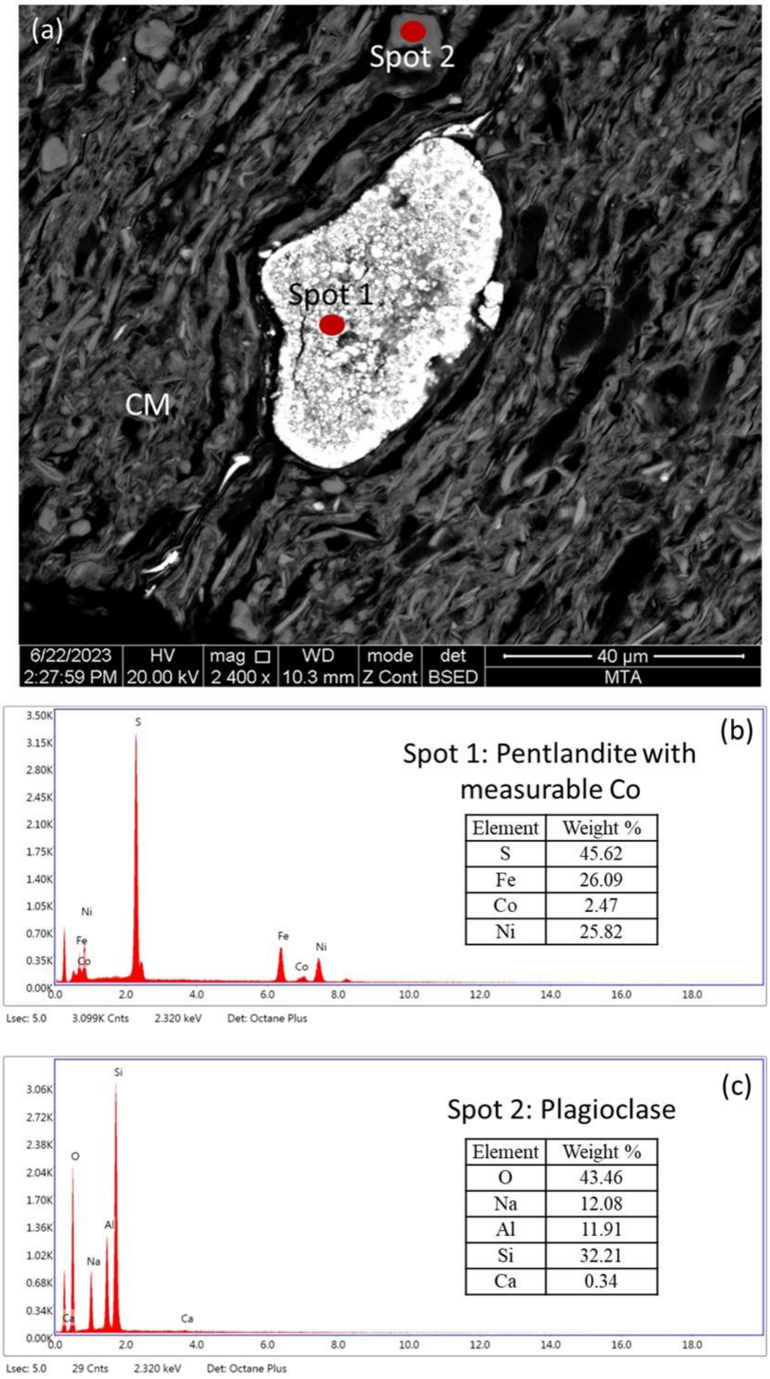

Element	Weight %
S	45.62
Fe	26.09
Co	2.47
Ni	25.82

Element	Weight %
O	43.46
Na	12.08
Al	11.91
Si	32.21
Ca	0.34

Figure 12: (a) SEM backscattered image of pentlandite and plagioclase grains associated with clay mineral (CM) aggregates; SEM-EDX spectra of (b) pentlandite at spot-1 and (c) plagioclase at spot-2.

Şekil 12: *Kil minerali (CM) yığışımları içerisindeki pentlandit ve plajiyoklaz tanelerine ait SEM geri saçılım görüntüsü. (b) Spot-1'deki pentlandit ve (c) Spot-2'deki plajiyoklaz ait SEM-EDX spektraları.*

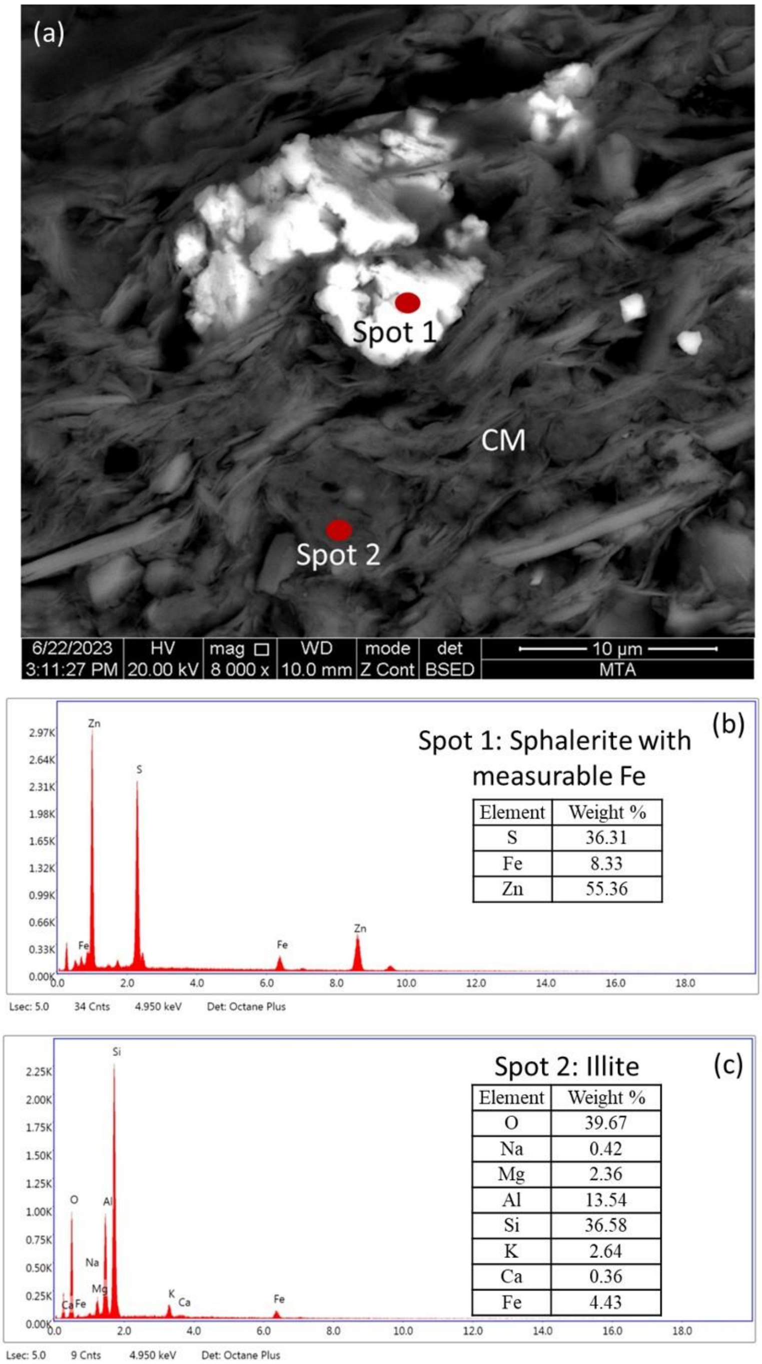

Spot 1: Sphalerite with measurable Fe

Element	Weight %
S	36.31
Fe	8.33
Zn	55.36

Spot 2: Illite

Element	Weight %
O	39.67
Na	0.42
Mg	2.36
Al	13.54
Si	36.58
K	2.64
Ca	0.36
Fe	4.43

Figure 13: (a) SEM backscattered image of sphalerite grains associated with clay mineral (CM) aggregates (illite); SEM-EDX spectra of (b) sphalerite at spot-1 and (c) illite at spot-2.

Şekil 13: *Kil minerali (CM) yığışımları içerisindeki sfalerit tanelerine ait SEM geri saçılım görüntüsü. (b) Spot-1'deki sfalerit ve (c) Spot-2'deki illite ait SEM-EDX spektraları.*

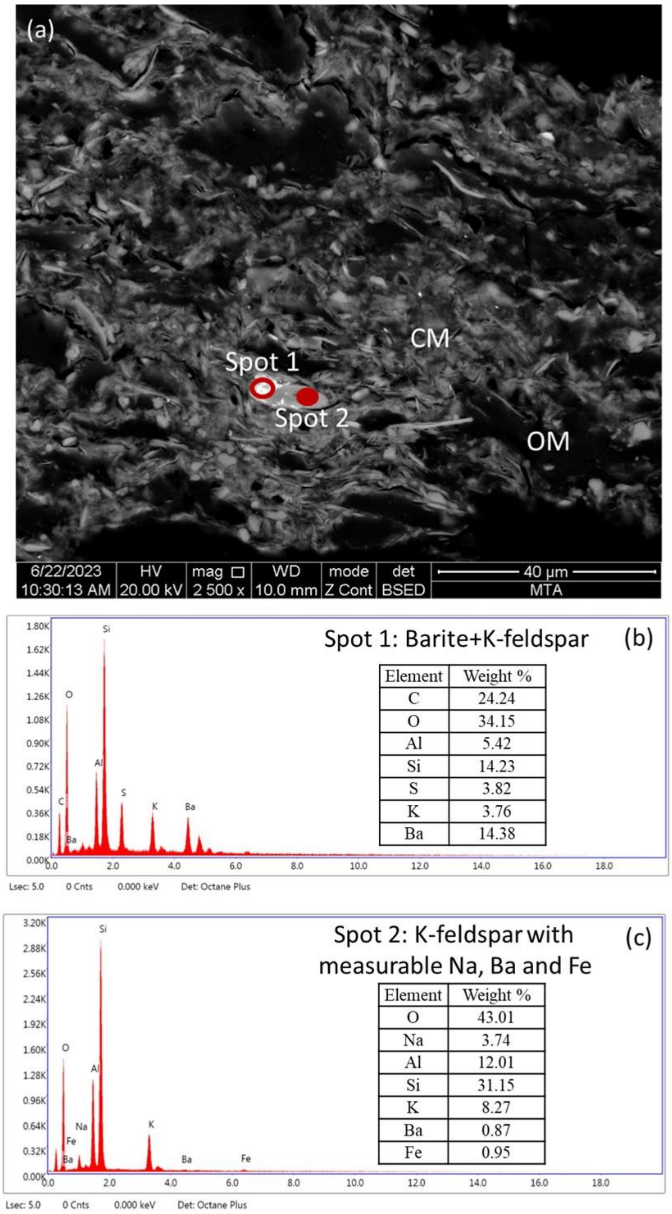

Spot 1: Barite+K-feldspar

Element	Weight %
C	24.24
O	34.15
Al	5.42
Si	14.23
S	3.82
K	3.76
Ba	14.38

Spot 2: K-feldspar with measurable Na, Ba and Fe

Element	Weight %
O	43.01
Na	3.74
Al	12.01
Si	31.15
K	8.27
Ba	0.87
Fe	0.95

Figure 14: (a) SEM backscattered image of barite (Brt) overgrowth around K-feldspar (Kfs) grain associated with clay mineral (CM) aggregates, and organic matter (OM); SEM-EDX spectra of (b) barite and K-feldspars at spot-1 and (c) K-feldpsar at spot-2.

Şekil 14: *Kil minerali (CM) yığışımları içerisindeki K-feldspat etrafında gelişen barit büyümleri ve organik maddeye (OM) ait SEM geri saçılım görüntüsü. (b) Spot-1'deki barit+K-feldspat ve (c) Spot-2'deki K-feldspata ait SEM-EDX spektraları.*

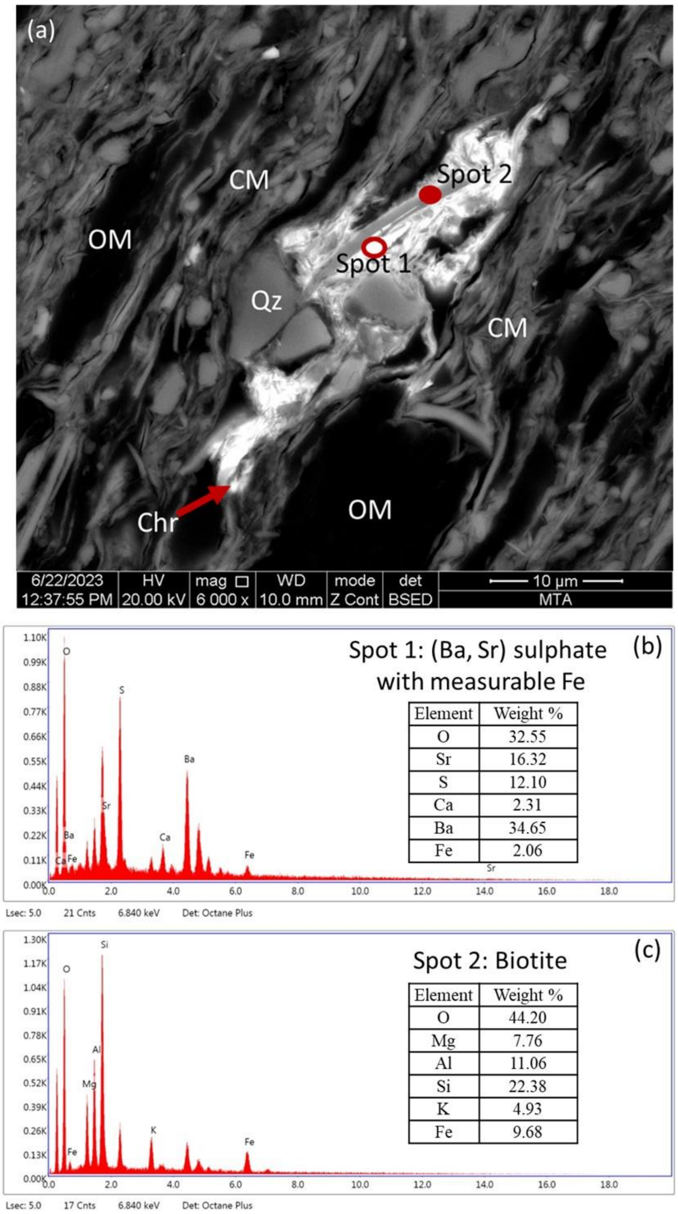

Element	Weight %
O	32.55
Sr	16.32
S	12.10
Ca	2.31
Ba	34.65
Fe	2.06

Element	Weight %
O	44.20
Mg	7.76
Al	11.06
Si	22.38
K	4.93
Fe	9.68

Figure 15: (a) SEM backscattered image of (Ba,Sr)-sulphate overgrowth around biotite grain, chromite (Chr) and quartz (Qz) grains associated with clay mineral (CM) aggregates, and organic matter (OM); SEM-EDX spectra of (b) (Ba,Sr)-sulphate at spot-1 and (c) biotite at spot-2.

Şekil 15: *Kil minerali (CM) yığışımları içerisindeki biyotit etrafında gelişen (Ba,Sr)-sülfat büyümeleri, kromit (Chr) ve kuvars (Qz) tanelerine ait SEM geri saçılım görüntüsü. (b) Spot-1'deki Ba,Sr)-sülfat ve (c) Spot-2'deki biyotite ait SEM-EDX spektraları.*

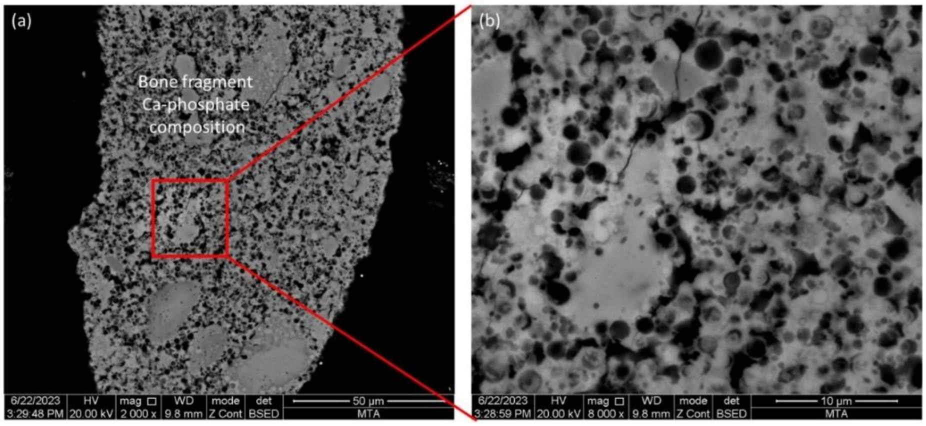

Figure 16: (a) SEM backscattered image of fossil bone fragment with Ca-phosphate composition; (b) enlarged view of selected area in image a.

Şekil 16: *(a) Ca-fosfat bileşimli fosil kemik kalıntısına ait SEM geri saçılım görüntüsü ve (b) Şekil 16a'daki seçili alanın büyütülmüş görüntüsü.*

origin (Ward, 2016); nevertheless, fossil bone remains with Ca-phosphate compositions were also detected during the SEM studies (Figures 11f and 16). Like calcareous fossil shell remains, these remains could also be indicators of increased biogenic activities within the palaeomires (Ward, 2002). Even though it is not easy to identify the origins of these bone remains, their co-occurrence with calcareous fossil shell remains may be related to the presence of aquatic animals due to increased water levels within the palaeomires.

Mode of occurrence of elements and elemental enrichments

The mode of occurrence of certain elements in coal could also be a useful tool for estimating depositional conditions during peat accumulation and/or the chemistry of porewater and circulating fluids within coal beds (Dai et al., 2020a, b; Finkelman et al., 2019). For this purpose, statistical methods (e.g., Pearson correlation or hierarchical cluster) have been commonly applied; however, recent studies show that statistical methods should be combined with direct methods, such as SEM-EDX or EPMA, in order to eliminate inaccurate correlations among elements (Eminağaoğlu et al., 2022; Eskanazy et al., 2010; Xu et al., 2020, 2022, 2023). Therefore, we combine statistical data with SEM-EDX data in this study in order to have results that are more robust.

Ash yields display strongly positive correlations with SiO_2 (r_{ash}=+0.905), Al_2O_3 (r_{ash}=+0.763), and K_2O (r_{ash}=+0.788), whereas they exhibit weak to moderately negative correlations with CaO (r_{ash}=-0.518), Fe_2O_3 (r_{ash}=-0.658), MgO (r_{ash}=-0.433), and Na_2O (r_{ash}=-0.518). These correlations could indicate that the concentrations of SiO_2, Al_2O_3, and K_2O in the samples are controlled by mineral matter. Since clay minerals, particularly illite and smectite, are the dominant phases, and quartz is abundantly present in the samples, SiO_2 and Al_2O_3 could be affiliated with clay minerals, and

SiO_2 is also associated with quartz. This assumption could also be supported by the SEM-EDX data, and K is also traced from the illitic clay matrix (Figure 13c). Furthermore, Al_2O_3 and K_2O are also traced from feldspars and biotite grains in the samples (Figures 14b and 15c). Several trace elements, such as Li, Sc, Ni, Cu, Ti, and Zr, have meaningfully moderate positive correlations with Al_2O_3 and SiO_2, which imply aluminosilicate affinity (Table 7). Besides, some of these elements are also affiliated with accessory minerals (e.g., biotite, Ti-oxide, and zircon) in the samples.

Table 7: Element affinities with ash yield and total S (%,db) deduced from the calculation of Pearson's correlation coefficients (**: correlation in table is significant at 0.01 level, 2-tailed, *: correlation is significant at 0.05 level, 2-tailed, x otherwise indicates correlation is less significant lower 0.05 level, 2-tailed).

***Çizelge 7:** Pearson korelasyon katsayısı hesaplanmasına göre kül ve toplam S (%, db) içerikleri ile elementlerin ilişkileri (**: korelasyon 0,01 düzeyinde anlamlı, 2 kuyruklu, *: korelasyon 0,05 düzeyinde anlamlı, 2 kuyruklu, x aksi halde korelasyonun 0,05 düzeyinden düşük, 2 kuyruklu olduğunu gösterir).*

Correlation with ash content $0.70<r<1.0$
SiO_2**, Al_2O_3*, K_2O**, Cr**, Ni**, Cu**, Zn**, Ge*, Pb**
Correlation with ash content $0.40<r<0.70$
P^x, V*, Mo^x, Co*
Correlation with ash content $r>-0.40$
Total S^x, Na_2O^x, MgO^x, CaO^x, Fe_2O_3*, B**, Be^x, Ba^x
Correlation with SiO_2 content $0.40<r<1.0$
TiO_2^x, Al_2O_3**, K_2O**, Li*, Sc*, V**, Cr**, Co**, Ni**, Cu**, Zn**, Ge*, Nb^x, Mo**, Pb**
Correlation with Al_2O_3 content $0.40<r<1.0$
TiO_2*, SiO_2**, K_2O**, Li*, Sc*, V**, Cr**, Co**, Ni**, Cu**, Zn**, Ge*, Zr^x, Nb*, Mo**, Pb**
Correlation with CaO content $0.40<r<1.0$
Total S^x, As^x, Sr**, Ba^x
Correlation with total S content $0.40<r<1.0$
Fe_2O_3**, CaO^x, B*, As^x, Sr*, Ba*

The negative correlations among ash yields, Fe_2O_3, MgO, and Na_2O could indicate organic affinities for these major oxides (Table 7), and Fe, Mg, and Na could be incorporated with organic matter in coal (Dai et al., 2020b). Fe_2O_3 also displays a positive correlation with total S contents (Table 7), which implies sulphide affinity for Fe, and additionally, SEM-EDX data also show that Fe is traced from pyrite, clay minerals (illitic matrix and chlorite grains), and accessory minerals, such as pentlandite, sphalerite, and barite (Figures 12b, 13b-c, 14b-c and 15b-c). This data implies that Fe_2O_3 seems to have mainly inorganic affinity instead of organic affinity. Pyrite is generally an abundant phase in the xylite-rich lithotype coal samples, and these samples have relatively lower ash yields (Table 1). Therefore, pseudo-correlations between ash yield and Fe_2O_3 are developed. Additionally, MgO is also traced from clay minerals, particularly smectite aggregates, chlorite grains (Figures 13c and 15c), and clay minerals and feldspar grains also contain measurable amount of Na by SEM-EDX (Figures 12c, 13c and14c). Hence, MgO and Na_2O may also have aluminosilicate affinity. Overall, SiO_2, Al_2O_3, K_2O, MgO, and Na_2O are mainly affiliated with aluminosilicate minerals, while Fe_2O_3 is mainly associated with sulphide minerals and, to a lesser extent, aluminosilicate minerals.

The negative correlations between ash and CaO could be an indicator of organic affinity (Table 7), and the existence of measurable amounts of Ca from organic matter by SEM-EDX could be testimony to this assumption. This could be related to Ca uptake by peat-forming plants from Ca-rich mire water and/or non-mineral Ca in the organic matter (Dai et al., 2020b; Karayiğit et al., 2017, 2021). Nevertheless, the presence of syngenetic carbonate mineral bands, calcareous fossil shell remains and siderite micronodules (Figures 10a-f and 17a-b) in the upper parts of Seam-VI could indicate that CaO has also inorganic affinity. Thus, Ca-rich water support into palaeomires and the development of weak acidic to neutral conditions within the palaeomires could control CaO concentrations of the samples. Moreover, apatite, barite, and feldspar grains and fossil bone remains in Ca-phosphate compositions serve as other other inorganic sources for CaO. Interestingly, biogenic activities within palaeomires might also cause elevations of CaO concentrations as fossil bone and calcareous shell remains-bearing samples have relatively higher CaO concentrations. All these imply that CaO exhibits dual affinity, and water chemistry and biogenic activities within the palaeomires may control CaO concentrations of the Seam-VI.

Boron enrichments in the Turkish Cenozoic coals are commonly reported, and B is mostly associated with clay minerals, organic matter, and possible accessory presences of B-bearing silicate minerals (e.g., tourmaline and zeolite minerals) (Çelik et al., 2021; Karayiğit et al., 2020a; Palmer et al., 2004). In the samples, B has meaningful negative correlations with ash yields (Table 7), which suggests an organic affinity for B in the studied samples. Furthermore, the dominance of clay minerals in the studied samples and the accessory presence of biotite could be other sources for B in the samples. Although B seems to have mainly organic affinity, the source of B-rich mire water is another question that should be addressed. Like the studied Seam-VI, B enrichments are also reported from the coal seams within the Danişmen Formation (Çelik et al., 2017; Güllüdağ and Altunsoy, 2022; Tuncalı et al., 2002). Since transgressive and regressive events took place during the Oligocene in the Thrace Basin (Batı and Gürgey, 2018), B enrichments in coal seams within the Danişmen Formation could be controlled by seawater penetration into palaeomires and/or after peatification. This assumption could be supported by B concentrations higher than 100 ppm, and the mean %Rr values are 0.40-0.41% (Dai et al., 2020a; Goodarzi and Swaine, 1994); however, B concentrations higher than 100 ppm could also be reported from coal seams within pure limnic sequences (Karayiğit et al., 2017). In agreement, coal seams within floodplain deposits in the Thrace Basin display relatively high B concentrations (Çelik et al., 2017). As mentioned above, the sequences bearing Seam-VI were deposited under floodplain and freshwater lake conditions (İslamoğlu et al., 2010); hence, B enrichments in the Seam-VI might not be controlled by seawater influence into palaeomire or post-peatification. Boron enrichments in coal seams within fluvio-lacustrine sequences in the Turkish Cenozoic coals are generally controlled by uptake B by peat-forming plants from B-rich leached surface water from volcanic/volcanoclastic rocks and/or synchronous and/or epiclastic volcanic inputs into palaeomires (Karayiğit et

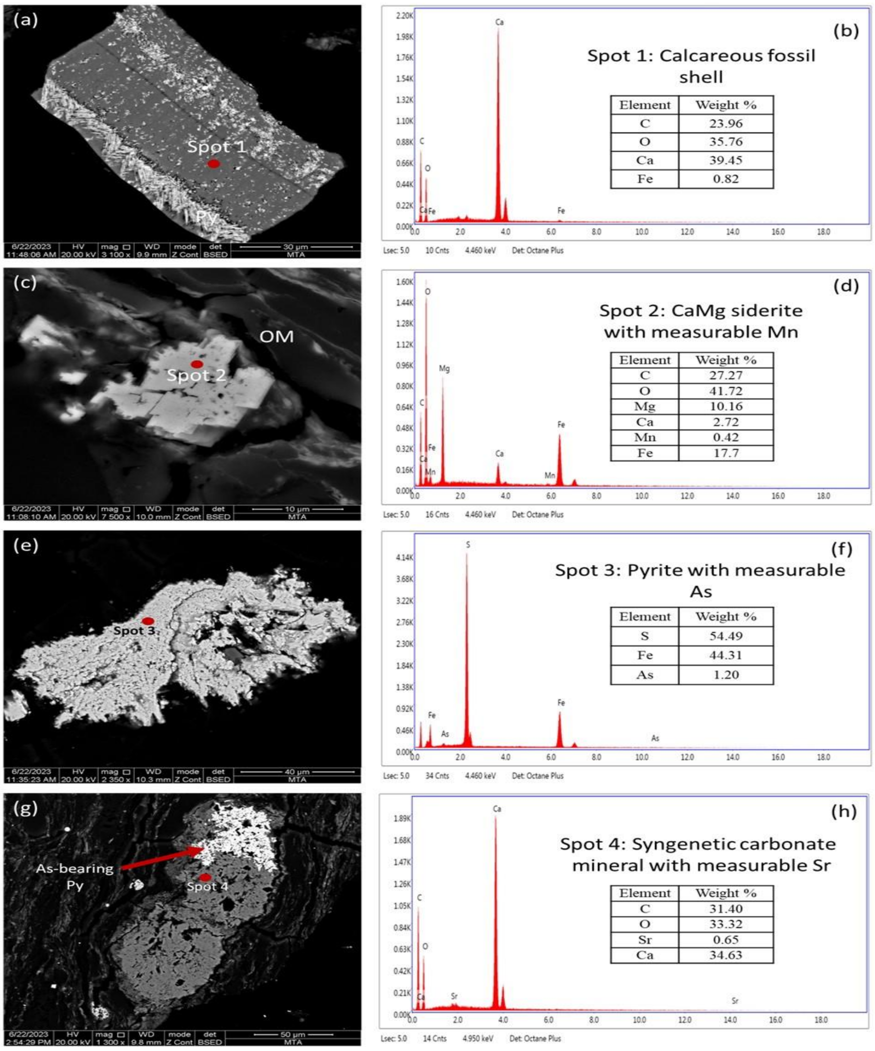

Spot 1: Calcareous fossil shell

Element	Weight %
C	23.96
O	35.76
Ca	39.45
Fe	0.82

Spot 2: CaMg siderite with measurable Mn

Element	Weight %
C	27.27
O	41.72
Mg	10.16
Ca	2.72
Mn	0.42
Fe	17.7

Spot 3: Pyrite with measurable As

Element	Weight %
S	54.49
Fe	44.31
As	1.20

Spot 4: Syngenetic carbonate mineral with measurable Sr

Element	Weight %
C	31.40
O	33.32
Sr	0.65
Ca	34.63

Figure 17: SEM backscattered images of crystalline phases in the studied coal and shale samples. (a) partially pyritized (Py) calcareous fossil shell remain; (b) SEM-EDX spectra of calcareous fossil shell remain at spot-1; (c) siderite micronodule within organic matter (OM); (d) SEM-EDX spectra of CaMg-siderite micronodule at spot-2; (e) pyrite grain; (f) SEM-EDX spectra of pyrite with measurable As at spot-3; (g) syngenetic carbonate mineral band associated with As-bearing pyrite (Py); (h) SEM-EDX spectra of syngenetic carbonate mineral band with measurable Sr at spot-4.

Şekil 17: *İncelenen kömür ve şeyl örneklerdeki kristalin fazlara ait SEM geri saçılım görüntüleri. (a) kısmen piritleşmiş (Py) kalkerli fosil kavkı kalıntısı; (b) spot-1'deki kalkerli fosil kavkı kalıntısına ait SEM-EDX spektrası; (c) organik madde (OM) içerisindeki siderite mikronodülü; (d) spot-2'deki CaMg-siderit nodülüne ait SEM-EDX spektrası; (e) pirit; (f) spot-3'deki As içeren pirite ait SEM-EDX spektrası; (g) As içeren pirit ile beraber bulunan sinjenetik carbonate minerali bandı; (h) spot-4'teki Sr içeren sinjenetik karbonat minerali bandına ait SEM-EDX spektrası.*

al., 2017, 2022a; Querol et al., 1997). This scenario might also be possible for the studied Seam-VI due to the presence of tuffite layers within the Oligocene sequences in the Thrace Basin. Thus, B-enrichments in the samples are mainly controlled by epiclastic influx from Oligocene tuffite layers into palaeomire, and liberated B from the alteration of epiclastic material seems to be taken by peat-forming plants.

Manganese in coal is mainly affiliated with carbonate minerals, particularly siderite and calcite, as well as Fe-sulphide minerals (e.g., pyrite) (Dai et al., 2021; Finkelman et al., 2019). Manganese -bearing siderite micronodules have been identified by SEM-EDX in the extremely high Mn-bearing sample 18-13/03 (Figures 10f and 17b). Such siderite micronodules could be an indicator of seawater influence (Antoshkina et al., 2017; Mozley, 1989); however, it is also documented that Mn-bearing siderite micronodules could be deposited under freshwater conditions due to the development of weak acidic to neutral conditions within palaeomires and/or during the late stages of peatification (Karayiğit et al., 2017, 2022a; Passey, 2014; Shang et al., 2023). In such cases, Mn could be derived from either the dissolution of synchronous and/or epiclastic volcanic inputs or Mn-rich surface water leached from magmatic rocks or marine carbonates. Hence, mire water could be enriched with Mn^{2+}, and Mn^{2+} could be substituted with Fe^{2+} in siderite micronodules. Considering the presence of Eocene marine carbonates, Mn mineralizations and Mn-deposits within the early Oligocene sequences (Gürgey and Batı, 2018; Gültekin, 1998, 1999; Gültekin and Balcı, 2018), the peat-forming environment in the study area had sufficient amounts of dissolved Fe^{2+} and Mn^{2+} ions within mire water and/or porewater during the late peatification stages. Thus, the formation of Mn-bearing siderite micronodules control Mn enrichments in the Seam-VI.

Nickel in coal is generally affiliated with sulphide minerals and clay minerals (Dai et al., 2021; Finkelman et al., 2019; Ruppert et al., 1996). Nickel displays meaningfully strong positive correlations with ash yields, Al_2O_3 and SiO_2 (Table 7), which indicates aluminosilicate affinity. Similar correlations were generally reported in Turkish Cenozoic coals (Palmer et al., 2004); on the other hand, the SEM-EDX data from these coals generally provide sulphide affinity (e.g., pyrite and pentlandite) instead of aluminosilicate affinity (Karayiğit et al., 2019, 2021, 2020). Of note, Ni-bearing sulphide mineral grains, particularly pentlandite, have been observed within the clay mineral matrix, and the source of pentlandite grains is generally related to clastic influx from Ni ore-bearing basement rocks. Even though Ni2+ could be substituted with Fe2+ in clay minerals (e.g., chlorite), the existence of such detritus Ni-sulphide mineral grains within clay minerals matrix could cause the correlations between Ni, Al2O3, and SiO2. More interestingly, Ni displays a negative correlation with the total S contents of the samples. This negative correlation could easily indicate that Ni is not affiliated with sulphide minerals; however, this correlation might be developed due to the relatively high total S contents of low ash yields xylite-rich lithotype samples. On the contrary, pentlandite grains are also commonly observed within clay mineral aggregates during SEM-EDX studies in the samples (Figure 12a-b). As mentioned earlier, these grains are presumably originated from clastic influx from sulphide mineralization and/or ores in the Strandja and/or Rhodope massifs (Marchev et al., 2005; Mortiz et al., 2014; Taner and Çağatay, 1983). Moreover, pentlandite grains in the samples also contain a measureable amount of Co by SEM-EDX

(Figure 12a-b). Nickel also shows moderate to positive correlations with Cu, Zn, and Pb (Table 7), which imply sulphide affinity for these elements. In agreement, detritus sphalerite grains are identified within clay mineral aggregates during SEM-EDX studies (Figure 13a-b). Therefore, as like Ni and Co, Cu, Zn and Pb concentrations in the samples might be controlled by the clastic influx into palaeomires from sulphide mineralisation and ore deposits in the Strandja and Rhodope massifs.

Like Ni, Cr and V also originate from clay minerals, sulphide minerals, and organic matter (Dai et al., 2021; Finkelman, 1994); however, detrital chromite grains, which originate from Cr- and Ni-bearing ore deposits, control their enrichments in Turkish Cenozoic coals (Karayiğit et al., 2019, 2020, 2021). Chromium and V display moderate to strong positive correlations with Al2O3, SiO2, Ni, and Co (Table 7). These correlations imply that both elements could be associated with either aluminosilicate minerals or Ni-bearing chromite grains in the samples. Notwithstanding that Karayiğit et al. (2022a) reported the accessory presence of detritus chromite grains from the coal seams within the Danişmen Formation, chromite grains have been detected in the studied samples from the Seam-VI in the İbrice area during SEM studies (Figure 15a). Nevertheless, both elements could substitute for Fe and Mg in clay minerals, particularly chlorites. Since chlorite grains are observed together with pentlandite grains within clay mineral aggregates in the samples through SEM studies, the correlations among Cr, V, Ni, and Co are presumably pseudo-correlations. Both chlorite and pentlandite grains have a detrital origin; in turn, Cr enrichments in the Seam-VI are presumably controlled by clastic influx into palaeomires.

Germanium in coal is mostly considered as an organically affiliated element, and its enrichment could be controlled by the existence of Ge-ore deposits and/or granitic rocks in the basement rocks and circulating hydrothermal solutions within coal seams (Dai et al., 2021; Yudovich, 2003). In contrast, Ge displays positive correlations with ash yields, Al2O3, and SiO2, and it does not have any meaningful correlations with maceral proportions. Therefore, the organic affinity might not be pronounced for Ge. According to general acceptance, Ge concentrations could be higher in the upper and lower parts and/or margins of coal deposits (Yudovich, 2003). Within this context, Ge could have relatively higher concentrations in the upper and lower parts of the sampling profile; however, Ge does not show any significant differences throughout the Seam-VI (Figure 8b). Besides, Ge also displays moderate positive correlations with Co, Ni, Cu, Zn, and Pb, which have mainly sulphide affinity. Even though Ge was not detected in sulphide minerals from the samples by used SEM equipment, it is reported that Ge-bearing sulphide minerals (e.g., sphalerite) could occur in sulphide deposits (Bernstein, 1985; Melcher et al., 2006; Yang et al., 2022). Since detritus sphalerite and pentlandite are observed in the samples during SEM-EDX analyses suggest a potential connection between Ge and the detritus sulphide mineral grains, which could originate from sulphide deposits in the basement. Although additional high-resolution (e.g., EPMA or TEM) analyses might be essential in the future, the correlation data among Ge, Ni, and Zn (Table 7) could imply that Ge enrichment in the Seam-VI could be controlled by clastic influx from sulphide ore-bearing deposits in the basement. The mode of occurrence of As in coal has been subjected to several studies due to its environmental impacts. The results of these studies indicated that As in coal is mainly derived from sulphide minerals and organic matter, with rare occurrences in aluminosilicate minerals (Dai et al., 2021; Finkelman et al., 2002; Hower et al., 2017). In the samples, As concentrations are close to world low-rank coal averages; nevertheless, As has moderately positive correlations with the total S contents of the samples (Table 7). Thus, As seems to have a sulphide affinity. The SEM-EDX data also agrees with this assumption, and As is traced from pyrites associated with syngenetic carbonate mineral bands (Figure 17e-h). The source of As in pyrite could be dissolved As from leached surface water sulphur mineralisation and sulhpide ore deposits in the Strandja and Rhodope massifs. Anaerobic conditions during peatification may cause the formation of As-bearing pyrites; in turn, As concentrations in syngenetic carbonate mineral band-bearing samples are relatively higher than other samples (Figure 17c-d). This could also explain weak positive correlation between As and CaO contents (Table 7). Molybdenum is another element could be affiliated with organic matter and sulphide minerals in coal (Dai et al., 2021; Finkelman et al., 2018), and it could also be redox-sensitive element together with As (Querol et al., 1996). In the samples, Mo displays moderate positive correlations with ash yields and chalcophille elements, such as Ni, Cu, Zn and Pb (Table 7); however, it has negative correlations with total S and no meaningful correlation with As. All these factors could suggest that enrichment of Mo in the samples may not be controlled by redox conditions in the palaeomires or may not mainly affiliated with As-bearing pyrites in the samples. Even though the detection of Mo by SEM-EDX in the studied samples could be problematic due to its overlap with S, detritus sulphide minerals might be source of Mo in the samples. Cupper-Mo porphyry ore deposits are also located in the Strandja and Rhodope massifs (Gültekin, 1999; Mavrogonatos et al., 2018; Ohta et al., 1988). Overall, Mo enrichments in the Seam-VI could also be related to clastic influx originating from ore-bearing Strandja and Rhodope massifs.

Strontium and Ba in coal are generally affiliated with organic matter, Sr- and Ba-bearing sulphate minerals, carbonates, and phosphate minerals, with rare occurrences in aluminosilicate minerals (Çelik et al., 2021; Dai et al., 2021; Ward et al., 1996). The ratio of Sr/Ba could serve as an indicator of paleosalinity (Dai et al., 2020a; Spiro et al., 2019). The Sr/Ba ratio of all analysed samples is higher than 1.0. As discussed above, the studied Seam-VI was deposited under freshwater conditions; however, this ratio could not be an accurate parameter for palaeosalinity estimation due to the existence of accessory minerals containing Sr and Ba (e.g., barite, zeolites, or phosphates) or Sr-bearing syngenetic carbonate minerals (Çelik et al., 2021; Dai et al., 2020a; Karayiğit et al., 2022c). In the studied samples, Sr and Ba display weak to moderate positive correlations with CaO and total S contents (Table 7). These correlations could imply carbonate and sulphate affinity for both elements. Supporting this assumption, Ca- and Sr-bearing barite overgrowths are observed around feldspar grains, and K-feldspar grains contain measurable Ba as revealed by SEM-EDX (Figures 11e and 14a-b). Furthermore, (Sr, Ba)-sulphate overgrowths are also identified around biotite grains (Figure 15a-b). Therefore, Ba and Sr mainly exhibits sulphate affinity in the samples. In Turkish Cenozoic coals, the presence of Sr-bearing calcareous fossil shell remains have been reported (Karayiğit et al., 2000). Considering the calcareous fossil shell remains observed in the samples, carbonate affinity is expected for

Sr. The SEM-EDX data, on the other hand, show that these remains do not contain a measurable amount of Sr (Figure 17a-b). The lack of Sr in such remains could be attributed to the potential discharge of Sr from aragonitic shell remains during calcination (Marcano et al., 2015). The SEM-EDX data also shows that Sr is traced from the syngenetic carbonate mineral bands (Figure 17g-h). The Sr in these bands may originated from either release of Sr in aragonitic shell remains or liberated Sr resulting from alterations of feldspar and/or biotite grains. Both could be possible, and Sr2+ ions seem to be incorporated into syngenetic carbonate mineral bands due to the formation of weak acidic to neutral conditions in the palaeomires and/or during the peatification.

Coal facies

The analysis of coal facies could be useful tools for estimating conditions during peat accumulation (Diesel, 1992; Calder et al., 1991; Kalaitzidis et al., 2004; Tuncer et al., 2023). The origins of some inertinite macerals or possible allochthonous origins of some liptinite (e.g., sporinite) and inertinite (e.g., inertodetrinite) macerals could cause misinterpretations (Crosdale, 1993; Dai et al., 2020a; O'Keefe et al., 2013; Scott, 2002). To overcome this problem and to make more accurate assumptions, coal facies analyses should be correlated with several parameters, i.e., palynofloral assemblages, sedimentological, geochemical, and mineralogical data obtained from coal seams and coal-bearing sequences (Bechtel et al., 2004; Çelik et al., 2021; Oskay et al., 2016, 2019; Zieger and Littke, 2019; Zdravkov et al., 2017, 2020). As a traditional approach, the plotting of data on a ternary diagram (Figure 18), which was designed by Mukhopadhyay (1989), implies that woody peat-forming vegetation was common in the palaeomires of the Seam-VI, and the contribution of herbaceous peat-forming plants (e.g., reeds) seems to be increased occasionally (Figure 18). Additionally, anoxic conditions might be common during peat accumulation, which could be supported by the presence of framboidal pyrite grains. The samples from Seam-VI in the İbrice area have also similar distributions to those in the Şahin and Hasköy areas in the Malkara coalfield, while the contribution of woody peat-forming vegetation was relatively higher in the Pirinççeşme area (Figure 18). This plotting data also suggests that anoxic conditions were predominant and the contribution of woody peat-forming vegetation was high during peat accumulations of all working coal seams in the Malkara coalfield, which is also supported by palynofloral data from the study area (İslamoğlu et al., 2010).

The plotting data on the Tissue Preservation Index (TPI) *vs*. Gelification Index (GI) and Vegetation Index (VI) *vs*. Groundwater Index (GWI) also imply that the precursor peats of Seam-VI mainly accumulated under telmatic conditions, with occasional development of limno-telmatic conditions (Figure 19). The GI values of the samples could imply that the water table was not stable but constantly covered the peat surface (Figure 19a) (Kalaitzidis et al., 2004; Karayiğit et al., 2017; Omodeo-Salé et al., 2017). This assumption could be supported by the relatively low inertinite contents of the samples (Table 2). The previous palaeoclimate studies from the Danişmen Formation have also pointed out that humid climatic conditions were common during the Late Oligocene in the Thrace Basin (Akgün et al., 2013; Çelik et al., 2017; Suc et al., 2015). The existence of humid conditions and rich fungal assemblages during the Late Oligocene in the Thrace Basin could also have caused the relatively funginite proportions of the samples. Similar observations have been reported in other coal mining areas in the Malkara coalfield and Yeniköy coalfield (Çelik et al., 2017; Karayiğit et al., 2021). Contrarily, the low GWI values of the studied samples and other coal seams in the Malkara coalfield might be indicators of drier conditions (Figure 19b). These low GWI values, on the other hand, could be expected from xylite-rich coals due to the masking effect of high telohuminite and low mineral matter contents (Kalaitzidis et al., 2004; Karayiğit et al., 2017; Oikonomopoulos et al., 2015; Životić et al., 2014). The TPI and VI values are higher than 1.0, suggesting that tissue preservation in the palaeomires was high due to anoxic conditions (Figure 19) (Kumar et al., 2024; Omodeo-Salé et al., 2017; Oskay et al., 2019; Zdravkov et al., 2017). These values also indicate that the contribution of woody vegetation was high during peat accumulation. In agreement, the palynoflora from the Malkara coalfield and other coal seams within the Danişmen Formation shows that coniferous peat-forming plants (e.g., Cupressaceae and Taxodioideae) were common vegetation elements during the Late Oligocene (Akgün et al., 2013; Çelik et al., 2017; İslamoğlu et al., 2010; Suc et al., 2015). Furthermore, *in-situ* fossilized wood trunks and root remains within the coal-bearing sequences were commonly reported from the study area and other coalfields in the Thrace basin (Çelik et al., 2017; Çevik-Üner et al., 2022; Karayiğit et al., 2022a). The previous studies on these remains also indicate the existence of coniferous peat-forming plants (e.g., *Glyptostroboxylon rudolphii* and *Taxodioxylon gypsaceum*) during the Late Oligocene (Akkemik, 2019; Akkemik and Sakınç, 2013; Çevik-Üner et al., 2022; Kayacık et al., 1995). Hence, the high TPI and VI values are expected for the İbrice area and other coal mining areas in the Malkara coalfield. Comparing the TPI and VI values of the studied samples from Seam-VI with those from other seams in the Şahin, Hasköy, and Pirinççeşme areas of the Malkara coalfield, the peat-forming vegetation and the degree of preservation of organic matter within the palaeomires of Seam-VI were presumably similar to those in the palaeomires of other seams in the Şahin and Hasköy areas. Hence, wet-forested and forested mires were commonly developed under the upper delta plain, and the contribution of herbaceous plants was increased due to the development

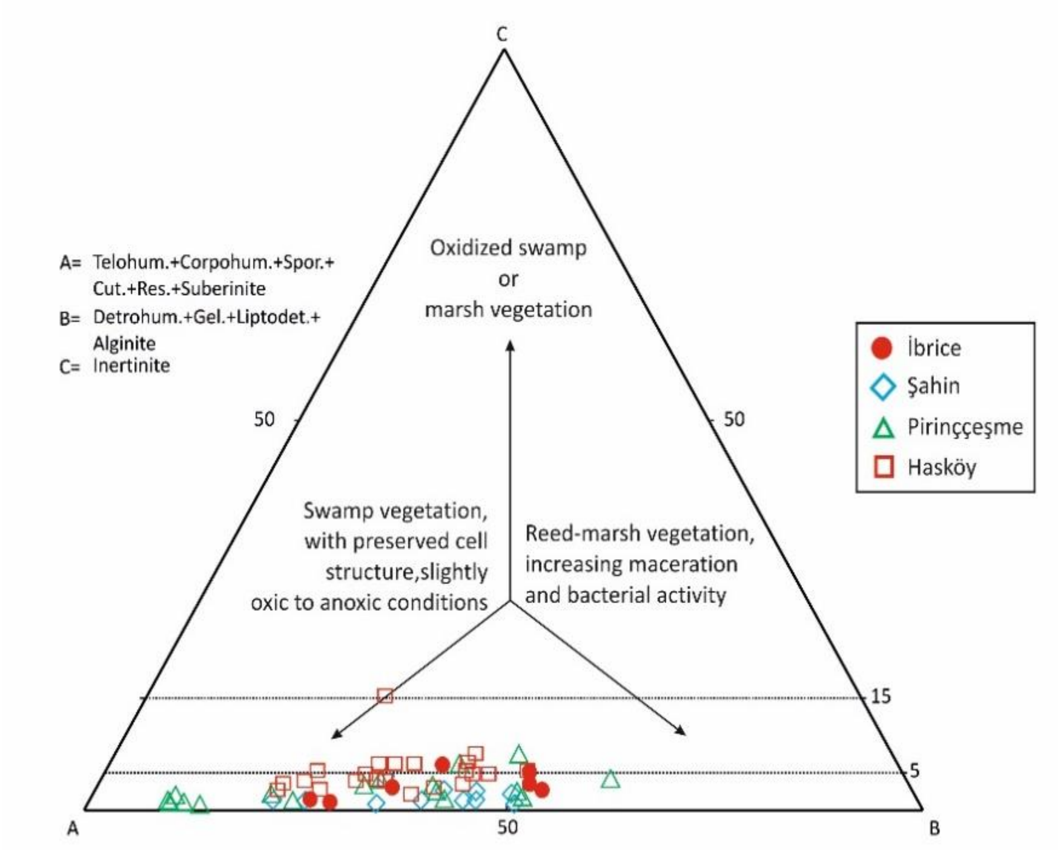

Figure 18: ABC ternary plot of the studied coal and samples from the Seam-VI in the İbrice area, and other coal seams in the Hasköy, Pirinççeşme and Şahin areas (after Mukhopadhyay, 1989; Hasköy, Pirinççeşme and Şahin areas data is from Karayiğit et al. (2022a).

Şekil 18: *İbrice sahasından incelenen Damar-VI ait kömür ve şeyl örnekleri ile Hasköy, Pirinççeşme ve Şahin sahalarından işletilen diğer damarlara ait verilerin ABC üçgen diyagramı üzerindeki dağılımları (Mukhopadhyay (1989)'a göre hesaplanmıştır; Hasköy, Pirinççeşme ve Şahin sahalarına ait veriler Karayiğit vd. (2022a)'dan alınmıştır).*

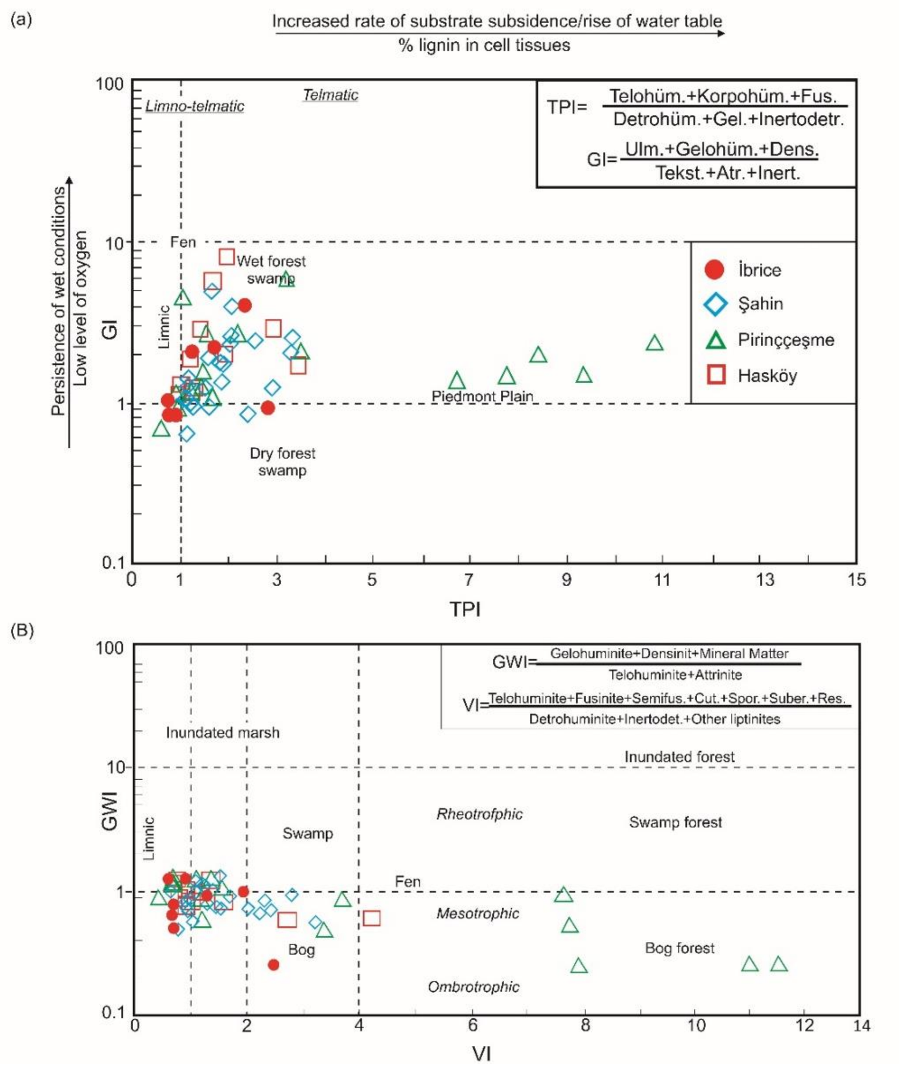

Figure 19: (a) GI *vs.* TPI plot of studied coal and samples from the Seam-VI in the İbrice area, and other coal seams in the Hasköy, Pirinççeşme and Şahin areas (after Diessel 1992, as modified by Kalaitzidis et al. 2004); b) VI *vs.* GWI plot of the studied coal and samples from the Seam-VI in the İbrice area, and other coal seams in the Hasköy, Pirinççeşme and Şahin areas (after Calder et al. 1991, as modified by Kalaitzidis et al. 2004; Hasköy, Pirinççeşme and Şahin areas data is from Karayiğit et al. (2022a).

Şekil 19: *İbrice sahasından incelenen Damar-VI ait kömür ve şeyl örnekleri ile Hasköy, Pirinççeşme ve Şahin sahalarından işletilen diğer damarlara ait verilerin (a) GI-TPI diyagramı üzerindeki dağılımları (Kalaitzidis vd. (2004) tarafından yapılan modifikasyona istinaden Diessel (1992)'ye göre hesaplanmıştır) ve (b) VI-GWI diyragamı üzerindeki dağılımları (Kalaitzidis vd. (2004) tarafından yapılan modifikasyona istinaden Calder vd. (1991)'e göre hesaplanmıştır) (Hasköy, Pirinççeşme ve Şahin sahalarına ait veriler Karayiğit vd. (2022a)'dan alınmıştır).*

of lower delta plain during the Late Oligocene in the study area (Karayiğit et al., 2022a; Omodeo-Salé et al., 2017; Oikonomopoulos et al., 2015). Besides, some significantly high TPI and VI values in the Pirinççeşme area could indicate that pure wet-forested mire was occasionally developed under upper delta plain conditions (Omodeo-Salé et al., 2017; Oikonomopoulos et al., 2015).

CONCLUSIONS

The results of this study revealed that the palaeomires of Seam-VI were mainly accumulated under telmatic conditions (forested mire), like other coal seams within the Danişmen Formation from the neighbouring Şahin, Hasköy, and Pirinççeşme areas in the Malkara coalfield; nevertheless, limno-telmatic conditions were occasionally developed. Under such conditions, the preservation of organic matter was high, and anoxic conditions were developed within palaeomires due to the high water table. Nevertheless, the presence of fossil shell remains and/or clay bands within xylite-rich lithotype coal samples and the existence of mineral-rich lithotype coal samples could indicate that sediment-laden water was introduced into palaeomires. Hence, ash yields, gross calorific values, and total C contents of samples are variable, and clay mineral aggregates were commonly observed during SEM studies. The sediment source area of clastic influx into palaeomires could have been mainly the Strandja and Rhodope massifs in the margins of the Thrace basin and/or formations bearing tuffite layers from the Late Eocene and Early Oligocene. Although the common presence of framboidal pyrite grains in the samples could be related to relatively low pH conditions within the palaeomires, their co-existence with syngenetic carbonate minerals (e.g., siderite and aragonite) and calcareous fossil shell remains could be evidence of very weak acidic to neutral conditions within the palaeomires.

Even though aluminosilicate minerals, particularly clay minerals, are abundant to dominant phases according to XRD whole-rock data, the majority of elemental enrichments in the Seam-VI seem to be mainly controlled by detritus accessory minerals in the samples. The clastic influx from the sulphide mineralization and ore deposits in the Strandja and Rhodope massifs into palaeomires seems to have caused the Co, Ni, Ge, and Mo enrichments due to the existence of accessory pentlandite and sphalerite grains within the clay mineral aggregates. The presence of siderite micronodules in the samples could indicate that Mn enrichments are related to these micronodules, and the source of Mn in the palaeomire could be dissolved surface water from Mn-bearing deposits in the Late Eocene-Early Oligocene sequences. The development of very weak acidic to neutral conditions might cause the formation of Mn-bearing siderite micronodules. The presence of Sr-bearing barite and (Ba,Sr)-sulphate overgrowths, which are related to alteration of feldspars and biotite grains within palaeomires, and syngenetic carbonate mineral bands could control the Sr enrichments in the samples. Overall, the clastic input ratio into palaeomires and pH conditions within these palaeomires seem to have elevated concentrations of the majority of enriched elements in Seam-VI.

ACKNOWLEDGEMENTS

A part of this study is supported by Scientific Research Projects Coordination Unit of Balıkesir University under the project number 2022/043. The authors would like to thank to Batı Trakya Madencilik Co. for permission sampling, Mr. Özgür Yüksel (Batı Trakya Madencilik Co.) and Dr. Cüneyt Bayraktaroğlu

(Atlı Enerji Co.) for their help during field study, and Ms. Yeşim A. Arslan (Standard Lab. Co.) for helps during XRF and ICP-OES analysis, and Prof. Dr. J. Hower for contributions. Finally, the authors would like thank Prof. Dr. Elif Varol-Muratçay, the editor-in-chief, Prof. Dr. Banu Koralay and the anonymous reviewer for their comments and corrections.

REFERENCES

Akgün F., Akkiraz, M.S., Üçbaş, S.D., Bozcu, M., Kapan-YeşIlyurt, S., Bozcu, A., 2013. Oligocene vegetation and climate characteristics in north-west Turkey: Data from the south-western part of the Thrace Basin. Turkish Journal of Earth Sciences, 22, 277-303. DOI: 10.3906/yer-1201-3

Akkemik Ü., Köse N., Poole, I., 2005. Sequoioideae (Cupressaceae) woods from the upper Oligocene of European Turkey (Thrace). Phytologia Balcanica, 11 (2), 119-131.

Altschuler, Z.S., Schnepfe, M.M., Silber, C.C., Simon, F.O., 1983. Sulfur diagenesis in Everglades peat and origin of pyrite in coal. Science, 221(4607), 221-227. DOI: 10.1126/science.221.4607.221

American Society for Testing and Materials (ASTM) D3174, 2020. Standard method of ash in the analysis sample of coal and coke from coal. ASTM, Philadelphia, 6pp. DOI: 10.1520/D3174-12R18

American Society for Testing and Materials (ASTM) D3175, 2020. Standard method of volatile matter in the analysis sample of coal and coke from coal. ASTM, Philadelphia, 14pp. DOI: 10.1520/D3175-20

American Society for Testing and Materials (ASTM) D3302/D3302M, 2022. Standard test method for total moisture in coal. ASTM, Philadelphia, 10pp. DOI: 10.1520/D3302_D3302M-22

American Society for Testing and Materials (ASTM) D4326, 2021. Standard test method for major and minor elements in coal ash by x-ray fluorescence. ASTM, Philadelphia, 9pp. DOI: 10.1520/D4326-21

American Society for Testing and Materials (ASTM) D5373, 2021. Standard Test Methods for determination of carbon, hydrogen and nitrogen in analysis samples of coal and carbon in analysis samples of coal and coke. ASTM, Philadelphia, 11pp. DOI: 10.1520/D5373-21

American Society for Testing and Materials (ASTM) D5865/D5865M, 2019. Standard test method for gross calorific value of coal and coke. ASTM, Philadelphia, 19pp. DOI: 10.1520/D5865_D5865M-19

Antoshkina, A.I., Ryabinkina, N.N., Valyaeva, O.V., 2017. Genesis of siderite nodules from the lower Carboniferous terrigenous sequence in the Subpolar Urals. Lithology and Mineral Resources, 52, 111-124. DOI: 10.1134/S0024490217020031

Bechtel, A., Markic, M., Sachsenhofer, R.F., Jelen B., Gratzer, R., Lücke, A., Püttmann, W., 2004. Paleoenvironment of the upper Oligocene Trbovlje coal seam (Slovenia). International Journal of Coal Geology, 57(1), 23-48. DOI: 10.1016/j.coal.2003.08.005

Bernstein, L.R., 1985. Germanium geochemistry and mineralogy. Geochimica et Cosmochimica Acta 49(11), 2409-2422. DOI: 10.1016/0016-7037(85)90241-8

Bohor, B.F., Triplehorn, D.M., 1993. Tonsteins: Altered volcanic-ash layers in coal-bearing sequences. GSA Special Papers, 285, 1-44.

Calder, J., Gibling, M., Mukhopadhyay, P., 1991. Peat formation in a Westphalian B piedmont setting, Cumberland Basin, Nova Scotia. Bulletin de la Societe geologique de France, 162(2), 238-298.

Chou, C.-L., 2012. Sulfur in coals: A review of geochemistry and origins. International Journal of Coal Geology, 100, 1-13. DOI: 10.1016/j.coal.2012.05.009

Crosdale, P.J., 1993. Coal maceral ratios as indicators of environment of deposition: do they work for ombrogenous mires? An example from the Miocene of New Zealand. Organic Geochemistry, 20, 797-809. DOI: 10.1016/0146-6380(93)90064-I

Çelik, Y., Karayiğit, A.I., Oskay, R.G., Kayseri-Özer, M.S., Christanis, K., Hower, J.C., Querol, X., 2021. A multidisciplinary study and palaeoenvironmental interpretation of middle Miocene Keles lignite (Harmancık Basin, NW Turkey), with emphasis on syngenetic zeolite formation. International Journal of Coal Geology, 237, Article Number 103691.

Çelik, Y., Karayiğit, A.İ., Querol, X., Oskay, R.G., Mastalerz, M., Kayseri-Özer, M.S., 2017. Coal characteristics, palynology, and palaeoenvironmental interpretation of the Yeniköy coal of late Oligocene age in the Thrace Basin (NW Turkey). International Journal of Coal Geology, 181, 103-123. DOI: 10.1016/j.coal.2021.103691

Çevik-Üner, B., Yılmaz-Şahin, S., Akkemik, Ü., 2022. Mineralogical and paleobotanical investigations of Oligo-Miocene petrified wood from the southwest of Thrace Basin (NW Turkey). Turkish Journal of Earth Sciences, 24, 383-397. DOI: 10.3906/yer-2106-2

Dai, S., Finkelman, R.B., 2018. Coal as a promising source of critical elements: Progress and future prospects. International Journal of Coal Geology, 186, 155-164. DOI: 10.1016/j.coal.2017.06.005

Dai, S., , Bechtel, A., Eble, C.F., Flore, R.M., French, D., Graham, I.T., Hood, M.M., Hower, J.C., Korasidis, V.A., Moore, T.A, Püttmann, W., Wei, Q., Zhao, L., O'Keefe, J.M.K., 2020a. Recognition of peat depositional environments in coal: A review. International Journal of Coal Geology, 219, Article number 103383. DOI: 10.1016/j.coal.2019.103383

Dai, S., Finkelman, R.B., French, D., Hower, J.C., Graham, I.T., Zhao, F., 2021. Modes of occurrence of elements in coal: A critical evaluation. Earth Science Reviews, 222, Article number 103815. DOI: 10.1016/j.earscirev.2021.103815

Dai, S., Finkelman, R.B., Hower, J.C., French, D., Graham, I.T., Zhao, L., 2023. Inorganic geochemistry of coal. Elsevier, Amsterdam, 438pp.

Dai, S., Hower, J.C., Finkelman, R.B., Graham, I.T., French, D., Ward, C.R., Eskenazy, G., Wei, Q., Zhao, L., 2020b. Organic associations of non-mineral elements in coal: A review. International Journal of Coal Geology, 218, 103347. DOI: 10.1016/j.coal.2019.103347

Dai, S., Seredin, V.V., Ward, C.R., Hower, J.C., Xing, Y., Zhang, W., Song, W., Wang, P., 2015. Enrichment of U–Se–Mo–Re–V in coals preserved within marine carbonate successions: geochemical and mineralogical data from the late Permian

Guiding Coalfield, Guizhou, China. Mineralium Deposita, 50, 159-186. DOI: 10.1007/s00126-014-0528-1

Dai, S., Ward, C.R., Graham, I.T., French, D., Hower, J.C., Zhao, L., Wang, X., 2017. Altered volcanic ashes in coal and coal-bearing sequences: A review of their nature and significance. Earth-Science Reviews, 175, 44-74. DOI: 10.1016/j.earscirev.2017.10.00

Dawson, G.K.W., Golding, S.D., Esterle, J.S., Massarotto, P., 2012. Occurrence of minerals within fractures and matrix of selected Bowen and Ruhr Basin coals. International Journal of Coal Geology, 94, 150-160. DOI: 10.1016/j.coal.2012.01.004

Demirtaş F., Bozcu, M., Koşun, E., Akkiraz, M.S., 2015. Petrography and palynology of late Oligocene and middle Miocene coals in the Gelibolu peninsula, NW Turkey. Turkish Journal of Earth Sciences, 24(4), 383-397. DOI: 10.3906/yer-1411-9

Diessel, C.F.K., 1992. Coal-bearing depositional systems, Springer, Berlin, 721pp.

Economic Commission for Europe-United Nations (E.C.E.-U.N.), 1998. International classification of in-seam coals. ECE, Geneva.

Ediger, V.Ş., 1981. Fossil fungal and algal bodies from Thrace Basin, Turkey. Palaeontographica Abteilung B, 179, 87-102.

Ediger, V.Ş., Alişan, C., 1989. Tertiary fungal and algal palynomorph biostratigraphy of the northern Thrace basin, Turkey. Review of Palaeobotany and Palynology, 58, 139-161. DOI: 10.1016/0034-6667(89)90082-1

Elsik, W.C., Ediger, V.Ş., Batı, Z., 1990. Fossil Fungal spore: Anatolinites gen. nov. Palynology, 14, 91-103. DOI: 10.1080/01916122.1990.9989374

Eminagaoglu, M., Oskay, R.G., Karayiğit, A.I., 2022. Evaluation of elemental affinities in coal using agglomerative hierarchical clustering algorithm: A case study in a thick and mineable coal seam (kM2) from Soma Basin (W. Turkey). International Journal of Coal Geology, 259, Article Number 104045. DOI: 10.1016/j.coal.2022.104045

Erarslan, C., Örgün, Y., 2017. Mineralogical and geochemical characterization of the Saray and Pınarhisar coals, Northwest Thrace Basin, Turkey. International Journal of Coal Geology, 173, 9-25. DOI: 10.1016/j.coal.2017.01.015

Erarslan, C., Örgün, Y., Balcı, N., 2020. Source and distribution of pyrite and inorganic sulfur isotopes in the Saray and Pınarhisar Coalfields, North Thrace Basin, Turkey. International Journal of Coal Geology, 227, 103533. DOI: 10.1016/j.coal.2020.103533

Erarslan, C., Örgün, Y., Bozkurtoğlu, E., 2014. Geochemistry of trace elements in the Keşan coal and its effect on the physicochemical features of ground- and surface waters in the coal fields, Edirne, Thrace Region, Turkey. International Journal of Coal Geology, 133, 1-12. DOI: 10.1016/j.coal.2014.09.003

Eskanazy, G., Finkelman, R.B., Chattarjee, S., 2010. Some considerations concerning the use of correlation coefficients and cluster analysis in interpreting coal geochemistry data. International Journal of Coal Geology, 83, 491-493. DOI: 10.1016/j.coal.2010.05.006

Fabiańska, M.J., Kurkiewicz, S., 2013. Biomarkers, aromatic hydrocarbons and polar compounds in the Neogene lignites and gangue sediments of the Konin and Turoszów Brown Coal Basins (Poland). International Journal of Coal Geology, 107, 24-44. DOI: 10.1016/j.coal.2012.11.008

Finkelman, R.B., 1994. Modes of occurrence of potentially hazardous elements in coal: levels of confidence. Fuel Processing Technology, 39, 21-34. DOI: 10.1016/0378-3820(94)90169-4

Finkelman, R.B., Dai, S., French, D., 2019. The importance of minerals in coal as the hosts of chemical elements: A review. International Journal of Coal Geology, 212, Article number 103251. DOI: 10.1016/j.coal.2019.103251

Finkelman, R.B., Orem, W., Castranova, V., Tatu, C.A., Belkin, H.E., Zheng, B.S., Lerch, H.E., Maharaj, S.V., Bates, A.L., 2002. Health impacts of coal and coal use: possible solutions. International Journal of Coal Geology, 50, 425-443. DOI: 10.1016/S0166-5162(02)00125-8

Finkelman, R.B., Palmer, C.A., Wang, P., 2018. Quantification of the modes of occurrence of 42 elements in coal. International Journal of Coal Geology, 185, 138-160. DOI: 10.1016/j.coal.2017.09.005

Goodarzi, F., Swaine, D.J., 1994. The influence of geological factors on the concentration of boron in Australian and Canadian coals. Chemical Geology,118(1-4), 301-318. DOI: 10.1016/0009-2541(94)90183-X

Güllüdağ, C.B., Altunsoy, M., 2022. Major and trace element geochemistry of the Malkara (Tekirdağ, Turkeu) coals. Kütahya Dumlupınar University Institute of Graduate Studies, 51, 1-25.

Gültekin, A.H., 1998. Geochemistry and Origin of the Oligocene Binkılıç manganese deposit, Thrace Basin, Turkey. Turkish Journal of Earth Sciences, 7(1), 11-24.

Gültekin, A.H., 1999. Geology, mineralogy and geochemistry of the Cu-Mo deposit associated with the Şükrüpaşa intrusion, Dereköy, Kırklareli. Geological Bulletin of Turkey, 42(1), 29-45.

Gültekin, A.H., Balci, N., 2018. Geochemical Characteristics of Sedimentary Manganese Deposit of Binkılıç, Thrace Basin, Turkey. Journal of Geology and Geophysics, 7(3), Article Number 1000336. DOI: 10.4172/2381-8719.1000336

Gürdal, G., 2011. Abundances and modes of occurrence of trace elements in the Çan coals (Miocene), Çanakkale-Turkey. International Journal of Coal Geology, 87, 157-173. DOI: 10.1016/j.coal.2011.06.008

Gürgey, K., Batı, Z., 2018. Palynological and petroleum geochemical assessment of the lower Oligocene Mezardere Formation, Thrace Basin, NW Turkey. Turkish Journal of Earth Sciences, 27, 349-383. DOI: 10.3906/yer-1710-24

Hower, J.C., Clack, H.L., Hood, M.M., Hopps, S.G., Thomas, G.H., 2017. Impact of coal source changes on mercury content in fly ash: Examples from a Kentucky power plant. International Journal of Coal Geology, 170, 2-6. DOI: 10.1016/j.coal.2016.10.007

Hower, J.C., Eble, C., Johnston, M.N., Ruppert, L.R., Hopps, S.D., Margan, T.D., 2023. Geochemistry of the Leatherwood coal in eastern Kentucky with an emphasis on enrichment and modes of occurrence of rare earth elements. International Journal of Coal Geology, 280, Article Number 104387. DOI: 10.1016/j.coal.2023.104387

Hower, J.C., Ruppert, L.F., Williams, D.A., 2002. Controls on boron and germanium distribution in the low-sulfur Amos coal bed, Western Kentucky coalfield, USA. International Journal of Coal Geology, 53(1), 27-42. DOI: 10.1016/S0166-5162(02)00151-9

Huvaz, O., Karahanoglu, N., Ediger, V., 2007. The thermal gradient history of the Thrace basin, NW Turkey: Correlation with basin evolution processes. Journal of Petroleum Geology, 30, 3-24. DOI: 10.1111/j.1747-5457.2007.00003.x

International Committee for Coal Petrology (ICCP), 1993. International Handbook of Coal Petrography. Centre National de la Recherche Scientifique, Paris, 146pp.

International Committee for Coal Petrology (ICCP), 2001. The new inertinite classification (ICCP System 1994). Fuel, 80, 459-471. DOI: 10.1016/S0016-2361(00)00102-2

International Standard Organisation (ISO) 11760, 2005. Classification of coals. International Organization for Standardization, Geneva, 18pp.

International Standard Organisation (ISO) 11885, 2007. Determination of selected elements by inductively coupled plasma optical emission spectrometry (ICP-OES). International Organization for Standardization, Geneva, 38pp.

International Standard Organization (ISO) 7404–2, 2009. Methods for the petrographic analysis of coals -Part 2: Methods of Preparing Coal Samples. International Organization for Standardization, Geneva, 24pp.

İslamoğlu, Y., Harzhauser, M., Gross, M., Jiménez-Moreno, G., Coric, S., Kroh, A., Rögl, F., van der Made, J., 2010. From Tethys to Eastern Paratethys: Oligocene depositional environments, paleoecology and paleobiogeography of the Thrace Basin (NW Turkey). International Journal of Earth Sciences, 99, 183-200. DOI: 10.1007/s00531-008-0378-0

Kalaitzidis, S., Bouzinos, A., Papazisimou, S., Christanis, K., 2004. A short-term establishment of forest fen habitat during Pliocene lignite formation in the Ptolemais Basin, NW Macedonia. Greece. International Journal of Coal Geology, 57, 243-263. DOI: 10.1016/j.coal.2003.12.002

Karayiğit, A.I., Atalay, M., Oskay, R.G., Córdoba, P., Querol, X., Bulut, Y., 2020. Variations in elemental and mineralogical compositions of Late Oligocene, Early and Middle Miocene coal seams in the Kale-Tavas Molasse sub-basin, SW Turkey. International Journal of Coal Geology, 218, Article Number 103366. DOI: 10.1016/j.coal.2019.103366

Karayiğit, A.I., Azeri, N., Oskay, R.G., Hower, J.C., 2022c. Zeolite and associated mineral occurrences in high-sulphur coals from the middle Miocene upper coal seam from underground mines in the Çayirhan coalfield, (Beypazarı, Central Turkey). International Journal of Coal Geology, 256, Article Number 104010. DOI: 10.1016/j.coal.2022.104010

Karayiğit, A.İ., Cicioğlu Sütcü, E., Temel, A., Gündoğdu, M.N., 2022b. Vertical variations of minerals in clayey sedimentary rocks in the cores of two-deep exploration wells from the Kozlu coalfield (Zonguldak, NW Türkiye), with emphasis on tonstein (schieferton) formation. Turkish Journal of Earth Sciences, 31(6), 597-621. DOI: 10.55730/1300-0985.1822

Karayiğit, A.I., Gayer, R.A., Querol, X., Onacak, T., 2000. Contents of major and trace elements in feed coals from Turkish coal-fired power plants. International Journal of Coal Geology, 44, 169-184. DOI: 10.1016/S0166-5162(00)00009-4

Karayiğit, A.İ., Littke, R., Querol, X., Jones, T., Oskay, R.G., Christanis, K., 2017. The Miocene coal seams in the Soma Basin (W. Turkey): Insights from coal petrography, mineralogy and geochemistry. International Journal of Coal Geology, 173, 110-128. DOI: 10.1016/j.coal.2020.103624

Karayiğit, A.İ., Oskay, R.G., Çelik, Y., 2022a. Mineralogy, petrography, and Rock-Eval pyrolysis of late Oligocene coal seams in the Malkara coal field from the Thrace Basin (NW Turkey). International Journal of Coal Geology, 244, 103814. DOI: 10.1016/j.coal.2021.103814

Karayiğit, A.İ., Yiğitler, Ö., İşerli, S., Querol, X., Mastalerz, M., Oskay, R.G., Hower, J.C., 2019. Mineralogy and Geochemistry of Feed Coals and Combustion Residues from Tunçbilekand Seyitömer Coal-Fired Power Plants in Western Turkey. Coal Combustion and Gasification Products, 11, 18-31. DOI: 0.4177/CCGP-D-18-00011.1

Karayiğit, A.I., Yerin, Ü.O., Oskay, R.G., Bulut, Y., Córdoba, P., 2021. Enrichment and distribution of elements in the middle Miocene coal seams in the Orhaneli coalfield (NW Turkey). International Journal of Coal Geology, 247, Article Number 103854. DOI: 10.1016/j.coal.2021.103854

Kayacık, H., Aytuğ, B., Yaltırık, F., Şanlı, İ., Efe, A., Akkemik, Ü, İnan, M., 1995. Sequoiadendron giganteum trees lived near İstanbul in Late Tertiary. Journal of the Faculty of Forestry Istanbul University, 45, 15-22 (in Turkish with extended English summary).

Ketris, M.P., Yudovich, Ya.E., 2009. Estimations of Clarkes for Carbonaceous biolithes: World averages for trace element contents in black shales and coals. International Journal of Coal Geology, 78, 135-148. DOI: 10.1016/j.coal.2009.01.002

Kolcon, I., Sachsenhofer, R.F., 1999. Petrography, palynology and depositional environments of the early Miocene Oberdorf lignite seam (Styrian Basin, Austria). International Journal of Coal Geology, 41, 275-30. DOI: 10.1016/S0166-5162(99)00023-3

Kortenski, J., 1992. Carbonate minerals in Bulgarian coals with different degrees of coalification. International Journal of Coal Geology, 20, 225-242. DOI: 10.1016/0166-5162(92)90015-O

Kumar, A., K. Singh, A., Christanis, K., 2024. Paleodepositional environment and hydrocarbon generation potential of the Paleogene lignite in the Barmer Basin, Rajasthan, India. Journal of Asian Earth Sciences, 259, Article Number 105892. DOI: 10.1016/j.jseaes.2023.105892

Lebküchner, R.F., 1974. Beitrag zur kenntnis der geologie des Oligozans von Mittelthrakien (Türkei). Bulletin of the Mineral Research and Exploration, 83, 1-59.

Marcano, M. C., Frank, T. D., Mukasa, S. B., Lohmann, K. C., Taviani, M. 2015. Diagenetic incorporation of Sr into aragonitic bivalve shells: implications for chronostratigraphic and palaeoenvironmental interpretations. Depositional Record, 1, 38-52. DOI: 10.1002/dep2.3

Marchev, P., Singer, B.S., Jelev, D., Hasson, S., Moritz, R., Bonev, N., 2004. The Ada Tepe deposit: A sediment-hosted, detachment fault-controlled, low-sulfidation gold deposit in the Eastern Rhodopes, SE Bulgaria. Schweizerische Mineralogische und Petrographische Mitteilungen, 84(1-2), 59-78.

Mavrogonatos, C., Voudouris, P., Spry, P.G., Melfos V., Klemme S., Berndt J., Baker T., Moritz R., Bissig, T., Monecke, T., Zaccarini, F., 2018. Mineralogical study of the advanced argillic alteration zone at the konos hill Mo–Cu–Re–Au porphyry prospect, NE Greece. Minerals, 8(11), Article Number 479. DOI: 10.3390/min8110479

Melcher, F., Oberthür, T., Rammlmair, D., 2006. Geochemical and mineralogical distribution of germanium in the Khusib Springs Cu–Zn–Pb–Ag sulfide deposit, Otavi Mountain Land, Namibia. Ore Geology Reviews, 28(1), 32-56. DOI: 10.1016/j.oregeorev.2005.04.006

Moritz, R., Noverraz, C., Márton, I., Marchev, P., Spikings, R., Fontignie, D., Spangenberg, J.E., Vennemann, T., Kolev, K., Hasson, S., 2014. Sedimentary-rock-hosted epithermal systems of the Tertiary Eastern Rhodopes, Bulgaria: New constraints from the Stremtsi gold prospect. Geological Society Special Publication, 402(1), 207-230. DOI: 10.1144/SP402.7

Mozley, P.S., 1989. Relation between depositional environment and the elemental composition of early diagenetic siderite. Geology, 17, 704-706. DOI: 10.1130/0091-7613(1989)017<0704:RBDEAT>2.3.CO;2

Mukhopadhyay, P., 1989. Organic petrography and organic geochemistry of Tertiary coals from Texas in relation to depositional environment and hydrocarbon generation. Bureau of Economic Geology, Texas.

Nadkarni, R.A., 1980. Multitechnique multielemental analysis of coal and fly ash. Analytical Chemistry, 52(6), 929-935. DOI: 10.1021/ac50056a036

Oikonomopoulos, I.K., Kaouras, G., Tougiannidis, N., Ricken, W., Gurk, M., Antoniadis, P., 2015. The depositional conditions and the palaeoenvironment of the Achlada xylite-dominated lignite in western Makedonia. Greece. Palaeogeography, Palaeoclimatology, Palaeoecology, 440, 777-792. DOI: 10.1016/j.palaeo.2015.09.031

Okay, A.I., Özcan, E., Siyako, M., Bürkan, K.A., Kylander-Clark, A.R.C., Bidgood, M., Shaw, D., Simmons, M.D., 2023. Thrace Basin—An Oligocene Clastic Basin Formed During the Exhumation of the Rhodope Complex. Tectonics, 42(10), Article number e2023TC007766. DOI: 10.1029/2023TC007766

Ohta, E., Dogan, R., Batık, H., Abe, M., 1988. Geology and mineralization of Derekoy porphyry copper deposit, northern Thrace, Turkey. Bulletin of Geological Survey of Japan, 39(2), 115-134.

O’Keefe, J.M.K., Bechtel, A., Christanis, K., Dai, S., DiMichele, W.A., Eble, C.F., Esterle, J.S., Mastalerz, M., Raymond, A.L., Valentim, B.V., Wagner, N.J., Ward, R., Hower, J.C., 2013. On the fundamental difference between coal rank and coal type. International Journal of Coal Geology, 118, 58-87. DOI: 10.1016/j.coal.2013.08.007

Omodeo-Salé, S., Deschamps, R., Michel, P., Chauveau, B., Suarez-Ruiz, I., 2017. The coal-bearing strata of the lower cretaceous Mannville Group (Western Canadian Sedimentary Basin, South Central Alberta), part 2: factors controlling the composition of organic matter accumulations. International Journal of Coal Geology, 179, 219-241. DOI: 10.1016/j.coal.2017.05.020

Oskay, R.G., Bechtel, A., Karayiğit, A.İ., 2019. Mineralogy, petrography and organic geochemistry of Miocene coal seams in the Kınık coalfield (Soma Basin-Western Turkey): Insights into depositional environment and palaeovegetation. International Journal of Coal Geology, 210, Article Number 103205. DOI: 10.1016/j.coal.2019.05.012

Oskay, R.G., Christanis, K., Inaner, H., Salman, M., Taka, M., 2016. Palaeoenvironmental reconstruction of the eastern part of the Karapınar-Ayrancı coal deposit (Central Turkey). International Journal of Coal Geology, 163, 100-111. DOI: 10.1016/j.coal.2016.06.022

Palmer, C.A., Tuncalı, E., Dennen, K.O., Coburn, T.C., Finkelman, R.B., 2004. Characterization of Turkish coals: a nationwide perspective. International Journal of Coal Geology, 60(2-4), 85-115. DOI: 10.1016/j.coal.2004.05.001

Pan, J., Nie, T., Vaziri Hassas, B., Rezaee, M., Wen, Z., Zhou, C., 2020. Recovery of rare earth elements from coal fly ash by integrated physical separation and acid leaching. Chemosphere, 248, Article number 126112. DOI: 10.1016/j.jece.2023.109921

Papanicolaou, C., Dehmer, J., Fowler, M., 2000. Petrological and organic geochemical characteristics of coal samples from Florina, lava, Moschopotamos and Kalavryta coal fields, Greece. International Journal of Coal Geology, 44, 267-292. DOI: 10.1016/S0166-5162(00)00014-8

Passey, S.R., 2014. The habit and origin of siderite spherules in the Eocene coal-bearing Prestfjall Formation, Faroe Islands. International Journal of Coal Geology, 122, 76-90. DOI: 10.1016/j.coal.2013.12.009

Perinçek, D., Ataş, N., Karatut, Ş., Erensoy, E., 2015. Geological factors controlling potential of lignite beds within the Danişmen formation in the Thrace Basin. Bulletin of the Mineral Research and Exploration, 150, 77-108. DOI: 10.19111/bmre.65462

Pickel, W., Kus, J., Flores, D., Kalaitzidis, S., Christanis, K., Cardott, B.J., Misz-Kennan, M., Rodrigues, S., Hentschel, A., Hamor-Vido, M., Crosdale, P., Wagner, N., ICCP, 2017. Classification of liptinite–ICCP system 1994. International Journal of Coal Geology, 169, 40-61. DOI: 10.1016/j.coal.2016.11.004

Querol, X., Cabrera, L., Pickel, W., López-Soler, A., Hagemann, H.W., Fernández-Turiel, J.L., 1996. Geological controls on the coal quality of the Mequinenza subbituminous coal deposit, northeast Spain. International Journal of Coal Geology, 29 (1-3), 67-91. DOI: 10.1016/0166-5162(95)00009-7

Querol, X., Chinchon, S., Lopez-Soler, A., 1989. Iron sulfide precipitation sequence in Albian coals from the Maestrazgo Basin, southeastern Iberian Range, northeastern Spain. International Journal of Coal Geology, 11(2), 171-189. DOI: 10.1016/0166-5162(89)90004-9

Querol, X., Whateley, M.K.G., Fernández-Turiel, J.L., Tuncali, E., 1997. Geological controls on the mineralogy and geochemistry of the Beypazari lignite, central Anatolia, Turkey. International Journal of Coal Geology, 33(3), 255-271. DOI: 10.1016/S0166-5162(96)00044-4

Ruppert, L., Finkelman, R., Boti, E., Milosavljevic, M., Tewalt, S., Simon, N., Dulong, F., 1996. Origin and significance of high nickel and chromium concentrations in Pliocene lignite of the Kosovo Basin, Serbia. International Journal of Coal Geology, 29, 235-258. DOI: 10.1016/0166-5162(95)00031-3

Sakinç, M., Yaltirak, C., Oktay, F.Y., 1999. Palaeogeographical evolution of the Thrace Neogene Basin and the Tethys-Paratethys relations at northwestern Turkey (Thrace). Palaeogeography, Palaeoclimatology, Palaeoecology, 153(1-4), 17-40. DOI: 10.1016/S0031-0182(99)00071-1

Scott, A., 2002. Coal petrology and the origin of coal macerals: a way ahead? International Journal of Coal Geology, 50(1-4), 119-134. DOI: 10.1016/S0166-5162(02)00116-7

Shang, N., Liu, J., Han, Q., Jia, R., Zhao, S., 2023. Mineralogy and geochemistry of the Middle Jurassic coal from the Hexi Mine, Shenfu Mining Area, Ordos Basin: With an emphasis on genetic indications of siderite. International Journal of Coal Geology, 279, Article Number 104384. DOI: 10.1016/j.coal.2023.104384

Shen, M., Dai, S., French, D., Graham, I.T., Spiro, B.F., Wang, N., Tian, X., 2023. Geochemical and mineralogical evidence for the formation of siderite in Late Permian coal-bearing strata from western Guizhou, SW China. Chemical Geology, 637, Article Number 121675. DOI: 10.1016/j.chemgeo.2023.121675

Siyako, M., 2006. “Lignitic Sandstones" of The Trakya Basin. Bulletin of the Mineral Research and Exploration, 132, 63-72.

Spears, D.A., 2012. The origin of tonsteins, an overview, and links with seatearths, fireclays and fragmental clay rocks. International Journal of Coal Geology, 94, 22-31. DOI: 10.1016/j.coal.2011.09.008

Spiro, B.F., Liu, J., Dai, D., Zeng, R., Large, D., French, D., 2019. Marine derived ^{87}Sr/^{86}Sr in coal, a new key to geochronology and palaeoenvironment: Elucidation of the India-Eurasia and China-Indochina collisions in Yunnan, China. International Journal of Coal Geology, 215, Article 103304. DOI: 10.1016/j.coal.2019.103304

Suc J.-P., Gillet, H., Çağatay, M.N., Popescu, S.-M., Lericolais, G., Armijo, R., Melinte-Dobrinescu, M.C., Şen, Ş., Clauzon, G., Sakinç, M., Zabci, C., Ucarkus, G., 2015. The region of the Strandja Sill (North Turkey) and the Messinian events. Marine and Petroleum Geology, 66, 149-164. DOI: 10.1016/j.marpetgeo.2015.01.013

Sykes, R., Fowler, M.G., Pratt, K.C., 1994. A Plant Tissue Origin for Ulminites A and B in Saskatchewan Lignites and Implications for R_o. Energy and Fuels, 8(6), 1402–1416. DOI: 10.1021/ef00048a032

Sýkorová, I. Pickel, W., Christanis, K., Wolf, M., Taylor, G.H., Flores, D., 2005. Classification of huminite-ICCP system 1994. International Journal of Coal Geology, 62, 85-106. DOI: 10.1016/j.coal.2004.06.006

Şafak, Ü., 2019. Paleoenvironmental features and ostracod investigation of Paleogene-Neogene sequences in Babaeski-Lüleburgaz- Muratli-Çorlu region (southeastern Thrace, Turkey). Bulletin of the Mineral Research and Exploration, 160, 45-79.

Taner, M.F., and Çağatay, A., 1983. Geology and mineralogy of the ore deposits of the Istranca Massif. Bulletin of the Geological Society of Turkey, 26, 31-40 (in Turkish with English abstract).

Tuncalı, E., Çiftci, B., Yavuz, N., Toprak, S., Köker, A., Gencer, Z., Ayçık, H., Pahin, N., 2002. Chemical and Technological Properties of Turkish Tertiary Coals. MTA Publication, Ankara, 401pp.

Tuncer, A., Karayiğit, A.İ., Oskay, R.G., Tunoğlu, C., Kayseri-Özer, M.S., Gümüş, B.A., Bulut, Y., Akbulut, A., 2023. A multi-proxy record of palaeoenvironmental and palaeoclimatic conditions during Plio-Pleistocene peat accumulation in the eastern flank of the Isparta Angle: A case study from the Şarkikaraağaç coalfield (Isparta, SW Central Anatolia). International Journal of Coal Geology, 256, Article Number 104149. DOI: 10.1016/j.coal.2022.104149

Turgut, S., Eseller, G., 2000. Sequence Stratigraphy/tectonics and depositional history in eastern Thrace Basin/ NW Turkey. Marine and Petroleum Geology, 17, 61-100. DOI: 10.1016/S0264-8172(99)00015-X

Xu, N., M. Peng, Q. Li, Xu, C., 2020. Towards consistent interpretations of coal geochemistry data on whole-coal versus ash bases through machine learning. Minerals, 10, Article Number 328. DOI: 10.3390/min10040328

Xu, N., Xu, C., Finkelman, R.B., Engle, M.A., Li, Q., Peng, M., He, L., Huang, B., Yang, Y., 2022. Coal elemental (compositional) data analysis with hierarchical clustering algorithms. International Journal of Coal Geology, 249, Article 103892. DOI: 10.1016/j.coal.2021.103892

Xu, N., Zhu, W., Wang, R., Li, Q., Wang, Z., Finkelman, R.B., 2023. Application of self-organizing maps to coal elemental data. International Journal of Coal Geology, 277, Article Number 104358. DOI: 10.1016/j.coal.2023.104358

Ward, C.R., 2002. Analysis and significance of mineral matter in coal seams. International Journal of Coal Geology, 50(1-4), 135-168. DOI: 10.1016/S0166-5162(02)00117-9

Ward, C.R., 2016. Analysis, origin and significance of mineral matter in coal: An updated review. International Journal of Coal Geology, 165, 1-27. DOI: 10.1016/j.coal.2016.07.014

Ward, C.R., Corcoran, J.F., Saxby, J.D., Read, H.W., 1996. Occurrence of phosphorus minerals in Australian coal seams. International Journal of Coal Geology, 30, 185-210. DOI: 10.1016/0166-5162(95)00055-0

Yang, Q., Zhang, X., Ulrich, T., Zhang, J., Wang, J., 2022. Trace element compositions of sulfides from Pb-Zn deposits in the Northeast Yunnan and northwest Guizhou Provinces, SW China: Insights from LA-ICP-MS analyses of sphalerite and pyrite. Ore Geology Reviews, 141, Article Number 104639. DOI: 10.1016/j.oregeorev.2021.104639

Yudovich, Ya.E., 2003. Notes on the marginal enrichment of Germanium in coal beds. International Journal of Coal Geology, 56(3-4), 223-232. DOI: 10.1016/j.coal.2003.08.003

Zdravkov, A., Bechtel, A., Sachsenhofer, R.F., Kortenski, J., 2017. Palaeoenvironmental implications of coal formation in Dobrudzha Basin, Bulgaria: Insights from organic petrological and geochemical properties. International Journal of Coal Geology, 180, 1-17. DOI: 10.1016/j.coal.2017.07.004

Zdravkov, A., Stefanova, M., Worobiec, E., Bechtel, A., Marinov, S., Kortenski, J., 2020. Implications for peat formation in Maritsa-West Basin, SE Bulgaria: Insights from organic petrology, palynology and biomarker assemblage. International Journal of Coal Geology, 222, Article Number 103447. DOI: 10.1016/j.coal.2020.103447

Zieger, L., Littke, R., 2019. Bolsovian (Pennsylvanian) tropical peat depositional environments: The example of the Ruhr Basin, Germany. International Journal of Coal Geology, 211, Article Number 103209. DOI: 10.1016/j.coal.2019.103209

Životić, D., Bechtel, A., Sachsenhofer, R., Gratzer, R., Radić, D., Obradović, M., Stojanović, K., 2014. Petrological and organic geochemical properties of lignite from the Kolubara and Kostolac basins, Serbia: Implication on Grindability index. International Journal of Coal Geology, 131, 344-362. DOI: 10.1016/j.coal.2014.07.004

Yerbilimleri, 2024, 45 (1), 52-65, 1325646

Hacettepe Üniversitesi Yerbilimleri Uygulama ve Araştırma Merkezi Bülteni (*Bulletin of the Earth Sciences Application and Research Centre of Hacettepe University*

YERBİLİMLERİ
Bulletin for Earth Sciences

ISSN: 2687- 2978

Crustal Stress States associated with the surface ruptures of the 2023 Pazarcık and Ekinözü Earthquakes

2023 Pazarcık ve Ekinözü depremlerinin yüzey kırıklarının yerkabuğu gerilimleri ile ilişkisi

ÖMER AYDAN [1*]

[1] University of the Ryukyus, Okinawa, Japan

Received *(geliş)*: 11 July *(Temmuz)* 2023   Accepted *(kabul)*: 19 March *(Mart)* 2024

ABSTRACT

The doublet disastrous earthquakes occurred on February 6, 2023, in the south-east part of Türkiye. These earthquakes caused a total of more than 500 km long surface ruptures with distinct ground deformations and striations. This study infers the crustal stress state at selected sites along the surface ruptures. The inferred crustal stress states differ depending upon location and the fault system. The inferred stress states of each segment of the fault system are presented and compared with those inferred focal plane solutions and the previous studies. Although the stress states inferred from the fault striations imply very complex stress states for the earthquake-affected region, they provide some insight to the stress state of the earthquake-affected region as well as that of Türkiye.

Keywords: crustal stress, surface rupture, 2023 Pazarcık and Ekinözü earthquake, striation

ÖZ

Türkiyenin güney doğusunda 2023 Şubat 6'sında ikiz 2 büyük oldukça yıkıcı deprem meydana gelmiştir. Bu depremlerde oluşan yüzey kırıkları 500 km'yi aşmakta ve belirgin kalıcı yüzey deformasyonları oluşturmuştur. Bu çalışmada yazar yüzey kırıklarından yerkabuğuna etkiyen gerilme durumunu belirlemektedir. Belirlenen yerkabuğu gerilmeleri fay sistemine göre değişim göstermektedir. Fay sistemlerinin segmentleri için belirlenen gerilme durumu ile deprem oluşum mekanizmasından tahmin edilen gerilme durumları sunulmuş ve daha önceki çalışmalarda belirlenenleri de içerecek şekilde birbirleri ile karşılaştırılmıştır. Bölgenin gerilme ortamı oldukça karmaşık olmasına rağmen, elde edilen gerilme durumu depremden etkilenen bölgenin ve Türkiyenin genelinde gerilme ortamına ışık tutmaktadır.

Anahtar Kelimeler: *yerkabuğu gerilmesi, yüzey kırıkları, 2023 Pazarcık ve Ekinözü depremleri, fay çiziğii*

https://doi.org/10.17824/yerbilimleri.1325646

*Sorumlu Yazar/ Corresponding Author: aydan@tec.u-ryukyu.ac.jp

INTRODUCTION

Two disastrous earthquakes occurred on February 6, 2023 in the south-east part of Türkiye. The first earthquake is named as the Pazarcık earthquake occurred at 4:17 and the second earthquake is named as Ekinözü (Elbistan) earthquake occurred at 13:24 after about 9 hours on the same day (e.g. Aydan and Ulusay, 2023; Goldberg et al. 2023). The first earthquake ruptured the segments of East Anadolu Fault Zone(EAFZ) and Dead Sea Fault Zone. The Pazarcık earthquake was initiated at Narlı fault segment belonging the Dead Sea Fault Zone and triggered the Pazarcık segment and Amanos segment belonging to East Anadolu Fault Zone, subsequently. While some forking of the East Anadolu Fault segments were observed at Gölbaşı City, another rupture started from Ozan passed over Harmanlı (H) and ruptured Erkenek Gölet (EG) dam body and extended towards Çelikhan (Ç). However, it should be noted this fault intermittently ruptured and it does not exactly follow the Erkenek fault trace depicted in the active fault map by MTA (Emre et al. 2013). The estimated total rupture length was about 330 (50+280) km while it was much shorter at the time of the earthquake occurrence (i.e. 250-270 km).

The Ekinözü earthquake involved E-W trending Çardak segment of the Çardak and Sürgü fault, which was 120-130 km long part initially, and later extended a total rupture length of 180 km. The focal mechanisms of both earthquakes implied sinistral slip with slight vertical component. The Ekinözü earthquake initially ruptured the fault segments between Göksun and Nurhak and later bended at Kullar and extended towards Doğanşehir. Figure 1 shows the fault ruptures together with seismicity and focal mechanisms reported by KOERI (2023) and the active faults prepared by MTA (Emre et al. 2013).

The author surveyed the entire surface ruptures caused by the 2023 Pazarcık and Ekinözü from March 24 until May 3, 2023 as a member of the reconnaissance team of the International Consortium on Geo-disaster Reduction (ICDdR) dispatched to the disaster region. Figure 2 shows the locations and views of selected scarps and the traces of fault surface ruptures caused by the 2023 Pazarcık and Ekinözü earthquakes. In this study, the crustal stresses inferred from the striations on the fault scarps using the method of Aydan (2000, 2003, 2013, 2015, 2016, 2019) are presented and the stress states of the earthquake affected regions are evaluated. These evaluations are also compared with those inferred from focal plane solutions released by several domestic and international seismological institutes (KOERI, USGS, ERD (AFAD), Harvard (GCMT), IGPT). The stress states of the Dead-Sea Fault Zone, East

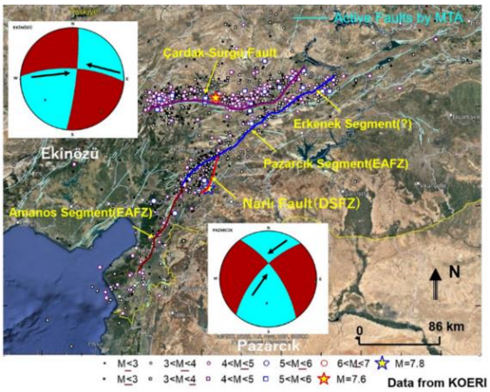

Figure 1. Locations of epicenters and focal mechanism of the earthquakes together with seismicity data from KOERI (2023) and the active faults prepared by MTA (Emre et al. 2013).

Şekil 1. *KOERI (2023) deprem verilerine göre depremlerin merkez üsleri ve faylanma mekanizmaları. Aktif fay haritası MTA (Emre vd. 2013).*

Anadolu Fault Zone and the Çardak and Sürgü Fault differ from each other and imply a very complex stress state. The author presents the inferred stress state of each segment of the fault zones and compares it with those inferred focal plane solutions and the previous studies.

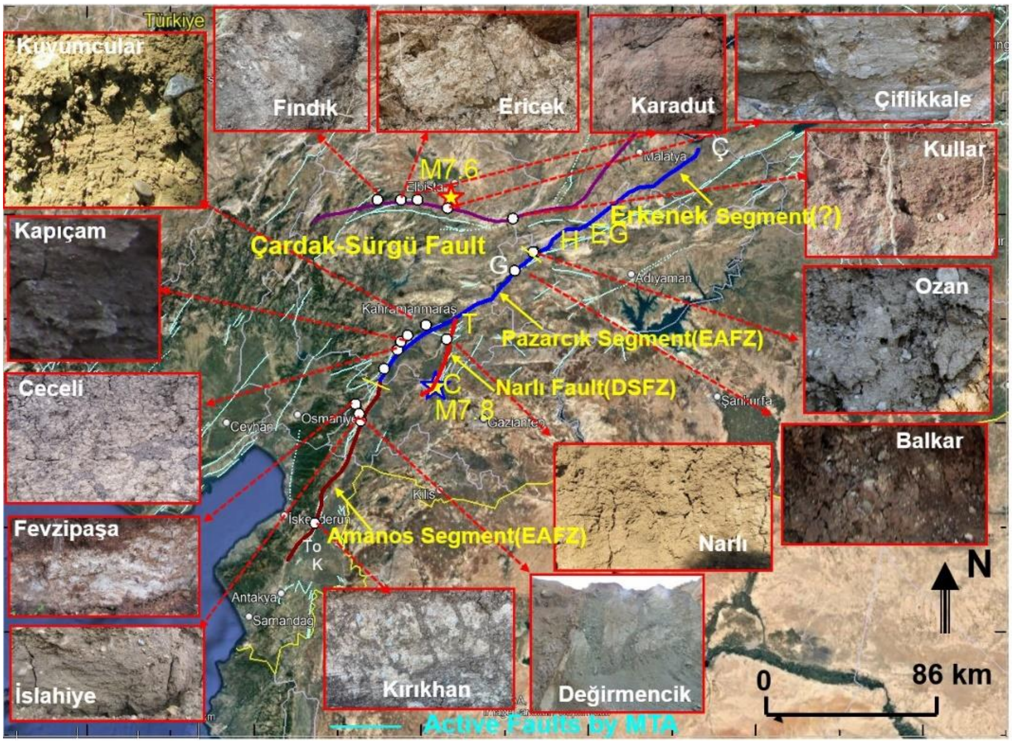

Figure 2. Views of the outcrops of scarps of the faults and their locations. C, T, G, H, Ç, K and To denote localities of Çöcelli, Tetirlik, Gölbaşı, Harmanlı, Çelikhan, Kumlu and Topboğazı mentioned in the text, respectively.

Şekil 2. *Yüzey kırıklarının yerleri ve görünümleri. C, T, G, H, Ç, K ve To Çöcelli, Tetirlik, Gölbaşı, Harmanlı, Çelikhan, Kumlu ve Topboğazı'nın özlenene yüzey kırıklarına karşılık gelmekte ve yerlerini göstermektedir.*

THE METHOD OF INFERENCE OF STRESS STATE

Aydan (2000a) proposed a new method to infer the crustal stresses from the striations of the faults or other structural geological features, which is powerful and accurate to study the stress state associated with paleo and modern-day earthquakes (Aydan 2013, 2015, 2016, 2023; Aydan and Tokashiki, 2003). While the details of the method can be found in the publications of Aydan (2000a, 2016, 2020), it is the most complete solution in view of the physics of rocks and fault mechanics. Furthermore, it is superior to any of available methods without any arbitrary assumption. Figure 3 illustrates the notation used in this method. Aydan (Aydan and Kim, 2002; Aydan, 2003; Aydan and Tokashiki, 2003) applied this method to infer the stress state of the earth crust from focal plane solutions with the utilization of rake angle obtained in focal plane solutions. However, it should be noted that the focal plane solutions used in geo-science are derived by assuming that the pure-shear condition holds. As a result of this assumption, one of the principal stresses is always compressive (P) while the other one is tensile (T) in focal plane solutions. This condition may further imply that the friction angle of the earthquake fault is nil.

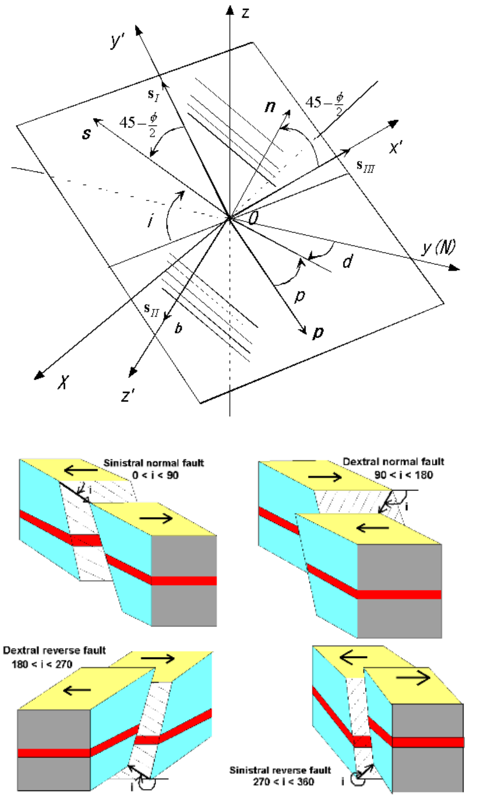

Figure 3. Illustrations of notation for fault striation method (from Aydan 2000a).

***Şekil 3.** Fay çiziği yönteminde kullanılan notasyon (Aydan 2000a'dan).*

THE INFERRED STRESS STATE FOR SURFACE RUPTURES OF THE 2023 PAZARCIK EARTHQUAKE

Narlı Segment of Dead Sea Fault Zone

The surface ruptures associated with the Narlı Segment were observed between Çöcelli (C) and Tetirlik (T) villages denoted in Figure 2. A clear fault scarp with an offset of 250cm was observed east of Narlı town (Figure 4a). Table 1 gives the computed stress state parameters for the fault scarp of the Narlı Segment (d_1, d_2, d_3 and p_1, p_2, p_3 stand for dip directions and plunges of principal stresses ($\sigma_1, \sigma_2, \sigma_3$) in Table 1 and other tables hereafter). Furthermore, the friction angle of faults are assumed to be 30 degrees in view of experiments on the samples obtained in Değirmencik, Ericek and Çiftlikkale fault rupture outcrops by the author and his group (Aydan et al. 2024) and studies by Byerlee (1978). Figure 4b shows a view of the fault surface striation while Figure 5 shows the inferred stress state and focal mechanism solutions. The maximum horizontal stress is orientated N39W and its ratio (σ_H/σ_v) to the vertical stress (σ_v) is 1.361.

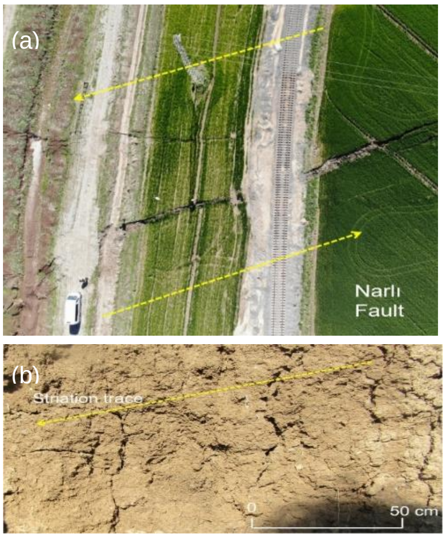

Figure 4. Views of the surface rupture (a) and the striation (b) of Narlı fault.

***Şekil 4.** Narlı fay yüzey kırığı (a) ile fay yüzleğinin (b) görüntüleri.*

Table 1. Computed results for Narlı Segment.

Tablo 1. *Narlı fayı segmenti için hesaplanan gerilme sonuçları*

σ_1			σ_2			σ_3			$\frac{\sigma_h}{\sigma_v}$	$\frac{\sigma_H}{\sigma_v}$	d_{σ_H}
$\frac{\sigma_1}{\sigma_v}$	d_1	p_1	$\frac{\sigma_2}{\sigma_v}$	d_2	p_2	$\frac{\sigma_3}{\sigma_v}$	d_3	p_3			
1.398	142	17	0.963	315	73	0.466	51	2	1.361	0.467	321

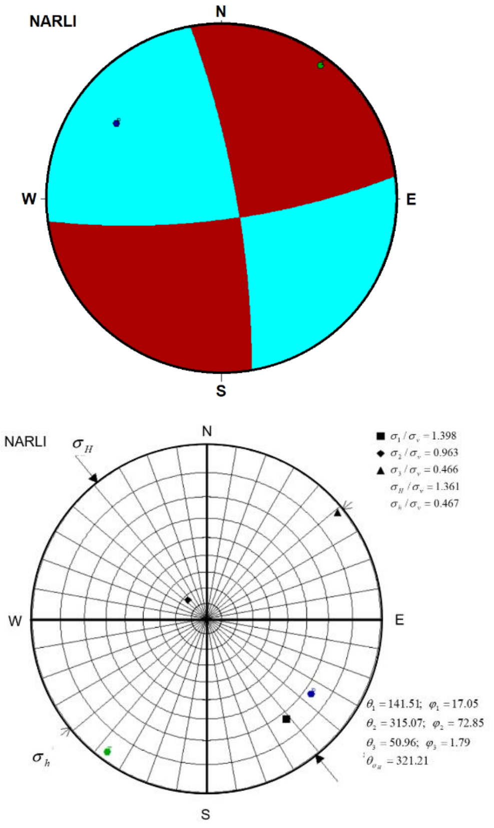

Figure 5. Stereo projections of inferred focal mechanism and stress tensor for the surface rupture of Narlı fault

Şekil 5.*Narlı fayı yüzey kırığı ve gerilme ortamı için elde edilen faylanma mekanizması ve gerilme tensörünün stereo izdüşümleri*

Amanos Segment of East Anadolu Fault Zone

Major ruptures of the Amanos segment appeared between Kırıkhan and Nurdağı. However, the surface ruptures also appeared at the south and runway of Hatay Airport. The offsets of surface ruptures at Kumlu (K) and Toboğazı (To) villages were less than 10-20cm. The stress inferences were done on the striation observations of the surface ruptures in Kırıkhan, Değirmencik, İslahiye and Fevzipaşa and they are reported herein. The fault observed at Değirmencik was spectacular in terms of fault orientation, the fault gouge and the fracturing within the fault zone near the ground surface. The host rock mass was highly fractured serpantine while the fault gouge was hydro-magnesite due to hydro-thermo-chemical metamorphism (Kumsar, 2023). Table 2 gives the computed stress state parameters for the fault scarps of the Amanos Segment at several localities mentioned above.

Pazarcık Segment

The striations on fault scarps at Ceceli, Türkoğlu, Kuyumcular, Kapıçam, Şekeroba, Balkar and Ozan were investigated and Table 3 gives the computed parameters of the stress state at each locality (see Figure 2 for locations). However, it should be noted that the

Erkenek segment of the EAF is said to start at Ozan, north of Gölbaşı (Duman and Emre, 2013). Furthermore, the two fault segments, namely, Pazarcık and Erkenek, join and forking occurred in this locality and in Gölbaşı City. In Şekeroba, there was more than 100 cm settlement of soft ground at a stone quarry about 800 m away east from the fault trace. The striations on the old fault surface in the stone quarry were also measured. This site also implied that the fault zone may have a wider zone of ground deformation without any distinct surface rupture. The maximum horizontal stress direction at Ozan Tunnel was highly rotated and it acts almost in the N70E direction, which implies the rotation and alteration of stress state from south to north.

Table 2. Computed results for Amanos Segment

Tablo 2. *Amanos segmenti için elde edilen sonuçlar*

Location	σ_1			σ_2			σ_3					
	$\frac{\sigma_1}{\sigma_v}$	d_1	p_1	$\frac{\sigma_2}{\sigma_v}$	d_2	p_2	$\frac{\sigma_3}{\sigma_v}$	d_3	p_3	$\frac{\sigma_h}{\sigma_v}$	$\frac{\sigma_H}{\sigma_v}$	d_{σ_H}
Kırıkhan	1.456	360	4	1.003	237	83	0.485	90	6	1.454	0.490	354
Değirmencik	1.452	332	16	1.000	197	68	0.484	66	15	1.415	0.521	334
Fevzipaşa	1.451	350	5	0.999	210	84	0.484	80	4	1.448	0.486	354
İslahiye	1.502	316	12	1.035	196	68	0.501	50	19	1.481	0.556	340

Table 3. Computed results for Pazarcık Segment

Tablo 3. *Pazarcık segmenti için elde edilen sonuçlar*

Location	σ_1			σ_2			σ_3					
	$\frac{\sigma_1}{\sigma_v}$	d_1	p_1	$\frac{\sigma_2}{\sigma_v}$	d_2	p_2	$\frac{\sigma_3}{\sigma_v}$	d_3	p_3	$\frac{\sigma_h}{\sigma_v}$	$\frac{\sigma_H}{\sigma_v}$	d_{σ_H}
Ceceli	1.427	5	19	0.983	145	66	0.476	270	14	1.378	0.507	2
Türkoğlu	1.452	332	16	1.000	197	68	0.484	66	15	1.415	0.521	334
Kuyumcular	1.452	350	3	1.000	124	86	0.485	260	3	1.451	0.485	350
Kapıçam	1.469	18	8	1.033	263	72	0.500	110	16	1.490	0.541	19
Şekeroba	1.495	346	19	1.030	112	60	0.498	247	23	1.440	0.583	341
Balkar	1.439	200	8	0.981	20	82	0.480	290	0	1.430	0.480	20
Ozan	1.495	163	20	1.030	37	59	0.498	263	24	1.436	0.587	348
Ozan Tunnel	1.455	70	3	1.002	190	85	0.485	340	4	1.454	0.488	70

THE INFERRED STRESS STATE FOR SURFACE RUPTURES OF THE 2023 EKINÖZÜ EARTHQUAKE

Major surface ruptures of Sürgü-Çardak fault zone took place in Nurhak fault complexity, which was designated by Duman and Emre (2013), Çardak Fault and Göksun bend, on the basis of segmentation suggested by Duman and Emre (2013). The striation of the surface ruptures in Kullar, Çiftlikkale, Karadut, Ericek and Fındık villages were analysed in this study.The fault observed at Çiftlikkale was spectacular in terms of fault orientation, the fault gouge and the fracturing within fault zone near ground surface. Table 4 gives the computed stress state parameters for the striations of the fault scarps of Nurhak fault complexity, Çardak Fault at several localities mentioned above.

FOCAL MECHANISM SOLUTIONS OF THE 2023 PAZARCIK AND EKİNÖZÜ EARTHQUAKES AND DISCUSSIONS

Focal Mechanism Solutions of the 2023 Pazarcık Earthquake

The focal mechanism of the Pazarcık earthquake was estimated by several seismological institutes and results are given in Table 5. The estimations imply that the earthquake occurred along a NE-SW trending fault with sinistral slip. Among all focal plane solutions, focal plane by KOERI is much more closer to the actual situations of faulting throughout the region investigated by the author and his group and the stress state for this solution is given in Table 6. As noted from Figure 6, the maximum horizontal stress is orientated in the direction of N18E. It should be also noted that this study is concerned with fresh fault ruptures that appeared during the earthquakes. However, the author measured striations on the old fault surfaces and they may be also important to explain the correlations among the new fault striations and old fault striations observed during the reconnaissance as well as those reported in the literature (e.g. Chorowicz et al. 1984; Yürür and Chorowicz, 1988).

Table 4. Computed results for Çardak Segment

Tablo 4. *Çardak segmenti için elde edilen sonuçlar*

Location	σ_1			σ_2			σ_3					
	$\frac{\sigma_1}{\sigma_v}$	d_1	p_1	$\frac{\sigma_2}{\sigma_v}$	d_2	p_2	$\frac{\sigma_3}{\sigma_v}$	d_3	p_3	$\frac{\sigma_h}{\sigma_v}$	$\frac{\sigma_H}{\sigma_v}$	d_{σ_H}
Kullar	1.473	68	22	1.015	197	57	0.491	328	23	1.400	0.578	62
Çiftlikkale	1.462	63	23	1.007	193	57	0.487	323	23	1.385	0.571	58
Karadut	1.509	60	2	1.040	158	74	0.503	327	16	1.500	0.544	59
Ericek	1.443	252	13	0.994	32	74	0.481	160	10	1.422	0.497	71
Fındık	1.599	256	25	1.102	14	45	0.533	148	35	1.491	0.742	67

Table 5. Focal plane solutions by different seismological institutes for the Pazarcık Earthquake

Tablo 5. *Pazarcık depremi için değişik deprem kurumların elde ettiği faylanma mekanizması parametreleri*

Institute	Mw	LAT	LON	Depth (km)	Fault Plane			Auxiliary Plane		
					Strike	Dip	Rake	Strike	Dip	Rake
GCMT	7.8	37.6	37.5	15	54	70	11	320	80	160
USGS	7.9	37.4	37.8	33	234	79	14	142	76	169
KOERI	7.7	37.1	37.1	10	222	64	-27	324	65	-152
ERD	7.8	37.2	37.1	18	233	74	18	140	77	168
IPGP	8.0	37.2	37.0	13	230	81	-18	323	72	-171

Table 6. Computed results for Pazarcık earthquake (KOERI Solution)

Tablo 6. *Pazarcık depremi (KOERI çözümü) için elde edilen sonuçlar*

σ_1			σ_2			σ_3			$\frac{\sigma_h}{\sigma_v}$	$\frac{\sigma_H}{\sigma_v}$	d_{σ_H}
$\frac{\sigma_1}{\sigma_v}$	d_1	p_1	$\frac{\sigma_2}{\sigma_v}$	d_2	p_2	$\frac{\sigma_3}{\sigma_v}$	d_3	p_3			
1.282	22	35	0.883	181	53	0.427	285	10	1.149	0.444	18

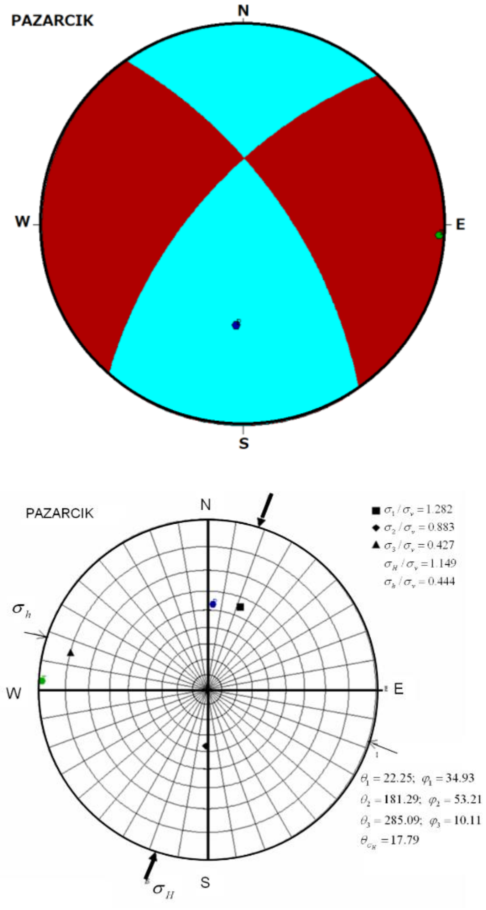

Figure 6. Focal mechanism by KOERI (2023) (re-drawn by the author) and its associated stress state for Pazarcık earthquake

Şekil 6. *Pazarcık depremi için KOERI (2023)'nin faylanma çözümü (yazar tarafından yeniden çizilmiştir) ve ilişkili gerilme ortamı*

Focal Mechanism Solutions for Ekinözü Earthquake

The focal mechanism of the Ekinözü earthquake was estimated by several seismological institutes and results are given in Table 7. The estimations imply that the earthquake occurred along a NE-SW trending fault with sinistral slip. Among all focal plane solutions, the focal plane computed by KOERI is close to the actual situations in view of rupture observations during the reconnaissance and the stress state for this solution is given in Table 8. As noted from Figure 7, the maximum horizontal stress is orientated in the direction of N65E. This implies that the stress state of the Pazarcık earthquake caused a great disturbance in the overall stress state of the region.

Discussions

Aydan (2016, 2020) evaluated the stress state of Türkiye using different techniques as shown in Figure 8 together with new additional data as well as those reported in the previous sections. The results plotted in Figure 8 obtained from various direct stress measurement techniques such as Acoustic Emisson (AE) method, stress relief method, flat jack method and indirect stress inference techniques such as GPS method, fault striation method, focal plane solution method (e.g. Aydan (2000a,b, 2020); Aydan and Paşamehmetoğlu, 1994; Tuncay et

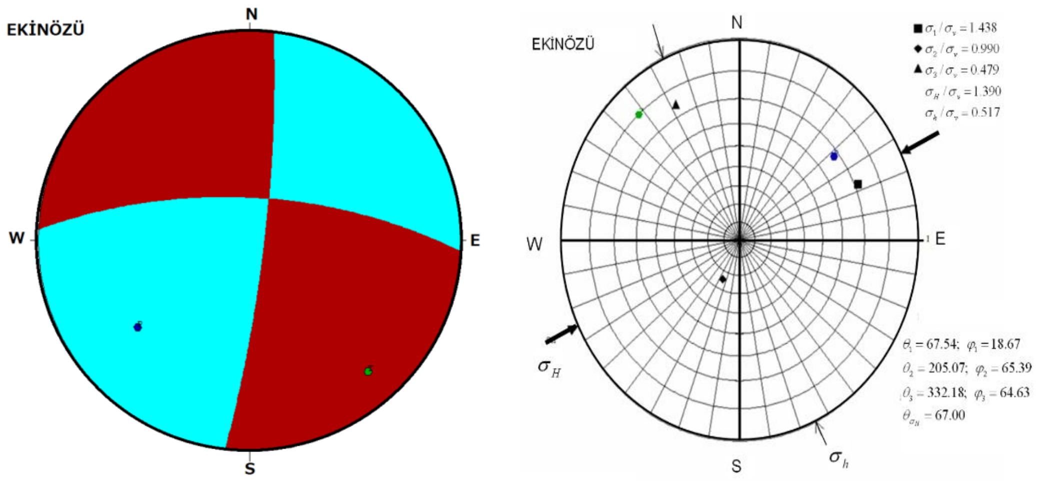

Figure 7. Focal mechanism by KOERI (2023) (re-drawn by the author) and its associated stress state for Ekinözü earthquake.

Şekil 7. *Ekinözü depremi için KOERI (2023)'nin faylanma çözümü (yazar tarafından yeniden çizilmiştir) ve ilişkili gerilme ortamı*

Table 7. Focal plane solutions by different seismological institutes for the Ekinözü Earthquake

Tablo 7. *Ekinözü depremi için değişik deprem kurumların elde ettiği faylanma mekanizması parametreleri*

Institute	Mw	LAT	LON	Depth (km)	Fault Plane			Auxiliary Plane		
					Strike	Dip	Rake	Strike	Dip	Rake
GCMT	7.7	38.1	37.2	12	261	42	-8	358	84	-132
USGS	7.6	38.0	37.2	19	276	82	-6	6	85	-172
KOERI	7.6	38.0	37.3	10	273	67	-9	6	81	-157
ERD	7.6	38.0	37.2	16	174	90	13	358	73	174
IPGP	7.7	38.0	37.2	13	270	60	-9	5	82	-150

Table 8. Computed results for Ekinözü earthquake (KOERI Solution)

***Tablo 8.** Ekinözü depremi (KOERI çözümü) için elde edilen sonuçlar*

σ_1			σ_2			σ_3			$\frac{\sigma_h}{\sigma_v}$	$\frac{\sigma_H}{\sigma_v}$	d_{σ_H}
$\frac{\sigma_1}{\sigma_v}$	d_1	p_1	$\frac{\sigma_2}{\sigma_v}$	d_2	p_2	$\frac{\sigma_3}{\sigma_v}$	d_3	p_3			
1.438	68	19	0.990	205	65	0.479	332	65	1.390	0.517	65

al. (2002, 2003)). As noted from the figure, maximum horizontal stress directions tend to be aligned in the directions of N-S, NE or NW. However, the stress state in the Arabian, which subduct beneath Anadolu platelet, orientated mainly in NE direction. The domain shown in Figure 8 is expanded and the results shown in the previous sections are re-plotted in Figure 9 together with available data previously. The data obtained from the analyses of striations on fault scarps caused by the doublet earthquakes are denoted with different colours in the respective figures. The direction of the maximum horizontal stresses obtained for Pazarcık earthquake are quite similar to those of the previous evaluations. On the other hand, the stress state within the Anadolu platelet is mainly NW-SE in the north of latitude 38 degrees. The stress state south of latitude 38 degrees is N-S or similar to that inferred for Ekinözü earthquake. It seems that the stress state within the earthquake affected area is rather complex and there is no doubt that the confirmation of the true stress state through in-situ stress measurement techniques is desirable despite such measurements are quite scarce in Türkiye.

Some stress directions for striations observed in this region are reported by Chorowicz et al. (1994) and Yürür and Chorowicz (1998), they utilized a method proposed by Angellier (1984), which actually violates the principles of rock and fault mechanics together with an arbitrary assumption on the first principle stress invariant and it fails to evaluate the stress state for a single fault plane and striation in view of the fundamental definition of stress tensor (e.g. Aydan 2021, Eringen 1980). While the maximum horizontal stress orientations might be similar to those obtained in this study, the least horizontal stress will never be the same in terms of magnitude, orientation and sense of compression.

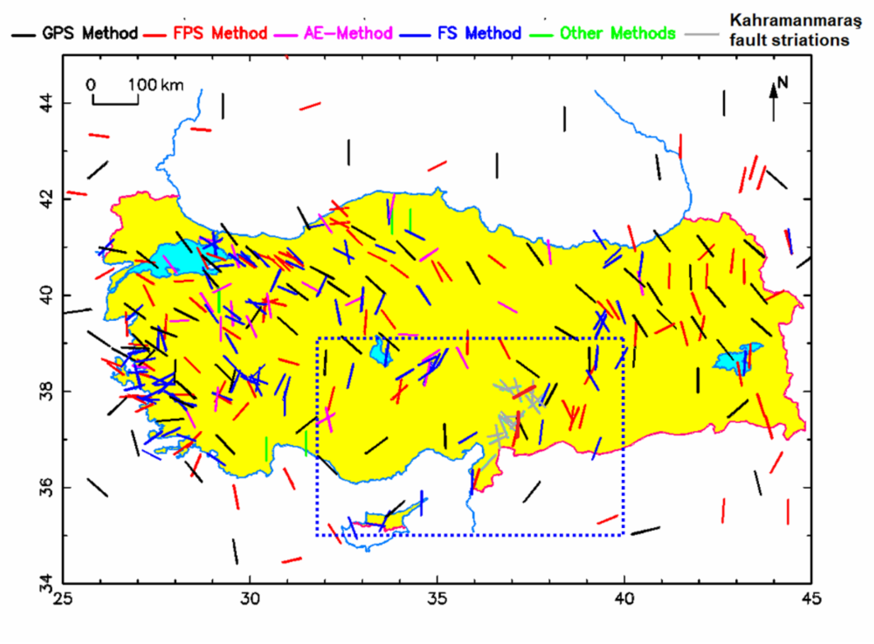

Figure 8. Distributions of maximum horizontal stress directions in Türkiye (from Aydan 2016, 2020) together with new additional data as well as those reported in the previous sections.

Şekil 8. *Aydan (2016, 2020) yayınladığı sonuçlar ve bu çalışmada elde edilen sonuçlar kullanılarak elde edilen Türkiye'de etkin en büyük yatay gerilme yönlerinin dağılımı*

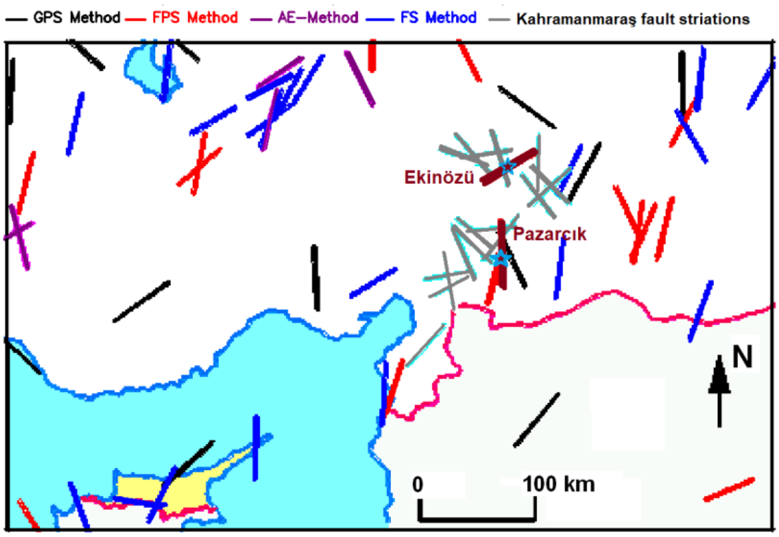

Figure 9. An expanded re-plot of the domain depicted in Figure 8

Şekil 9.*Şekil 8'de işaret edilen bölgenin büyütülmüş yeniden çizimi*

Following the Pazarcık and Ekinözü earthquakes or briefly Kahramanaraş earthquakes, some studies (e.g. Toda et al. 2023) were done on the stress changes using the Coulomb stress transfer method, which is based on static dislocation theory utilising the closed form solutions proposed by Okada (1992) for elastic isotropic half-space. However, this method can only evaluate static changes for a given prescribed displacement/traction distribution and it does not consider the total stress state acting in the earth's crust and the elasto-visco-plastic dissipation of stored energy during faulting. Therefore, the method can not evaluate the true stress state presented in this study. As also shown by Aydan (2015), it is possible to evaluate the changes of orientation and stress components due to earthquakes if peak and residual friction angles of the earthquake fault are available. In addition, better computational methods considering the three-dimensional crustal structure, stress state prior to earthquakes an elasto-visco-plastic dissipation of the stored energy are recently summarized and discussed in a text book by Aydan (2023) on Earthquake Science And Engineering.

CONCLUSIONS

The stress state obtained from the striation of the fault surface ruptures in this study can be usefull to infer the stress state of the earthquake region. The stress state along the fault segments of Dead Sea Fault Zone may be similar that of the Amanos segment. On the other hand, the stress state of the Pazarcık segment is slightly different than that of the Amanos segment. Furthermore, the orientation of the stress state of the Ekinözü earthquake differs by more than 40-50 degrees. This may imply that the stress states in the subducting Arabian plate and Anadolu platelet differ from each other, which is quite similar to the situation of Tokai Region in Japan (Aydan 2003, 2013). This difference is likely to be the main driving forces for earthquakes along the Çardak-Sürgü Fault. However, it is quite desirable to validate the estimations presented in this study through in-situ stress measurements available in the field of Rock Mechanics and Rock Enineering (Amadei and Stephanson, 1997; Aydan 2016, 2020). The borehole breakout method for deep oil and gas borings may also be used for assessing the stress field of this region.

ACKNOWLEDGEMENTS

The author sincerely thank Prof. Reşat Ulusay (Hacettepe University) and Prof. Halil Kumsar (Pamukkale University) for joining the author's investigation of surface ruptures of 2023 Pazarcık ve Ekinözü earthquakes, Dr. Nazlı Tunar Özcan for inviting the author to contribute Yerbilimleri and reviewers for very usefull discussions as well as providing references for the previous studies in the same issue.

REFERENCES

Amadei, B., and Stephansson, O., 1997. Rock Stress and Its Measurement. Chapman, and Hall, London, 490pp.

Angellier, J., 1984. Tectonic analysis of fault slip data sets, J. Geophys. Res., 89(B7), 5834-5848.

Aydan, Ö., 2000a. A stress inference method based on structural geological features for the full-stress components in the earth's crust, Yerbilimleri, No. 22, 223-236.

Aydan, Ö., 2000b. A stress inference method based on GPS measurements for the directions and rate of stresses in the earth' crust and their variation with time. Yerbilimleri, 22, 21-32.

Aydan, Ö. 2003. The Inference of crustal stresses in Japan with a particular emphasis on Tokai region, Int. Symp. on Rock Stress, Kumamoto, 343-348.

Aydan, Ö. 2013. Inference of Contemporary Crustal Stresses from Recent Large Earthquakes and Its Comparison with Other Direct and Indirect Methods. 6th International Symposium on In Situ Rock Stress (RS2013), Sendai, Paper No. 1051, 420-427.

Aydan, Ö. 2015. Crustal stress changes and characteristics of damage to geo-engineering structures induced by the Great East Japan Earthquake of 2011. Bull Eng Geol Environ, 74(3), 1057-1070.

Aydan, Ö., 2016. An integrated approach for the evaluation of measurements and inferences of in-situ stresses. Keynote lecture, RS2016 Symposium, 7th Int. Symp. on In-situ Rock Stress, Tampere, pp. 38-57.

Aydan, Ö., 2020. Rock Mechanics and Rock Engineering: Fundamentals, Vol.1, CRC Press, Taylor and Francis Group, 412 p.

Aydan, Ö., 2021. Continuum and Computational Mechanics for Geomechanical Engineers, ISRM Book Series No.7, CRC Press, Taylor and Francis Group, 324 p.

Aydan, Ö., 2023. Earthquake Science and Engineering, CRC Press, Taylor and Francis Group, 494p.

Aydan, Ö., and Kim, Y. 2002. The inference of crustal stresses and possible earthquake faulting mechanism in Shizuoka Prefecture from the striations of faults. Journal of the School of Marine Science and Technology, Tokai University, No. 54, 21-35.

Aydan, Ö. ve Paşamehmetoğlu, A.G., 1994. Dünyanın çeşitli yörelerinde ölçülmüş yerinde gerilimler ve yatay gerilim katsayısı. Kaya Mekaniği Bülteni, 10, 1-17.

Aydan, Ö. and N. Tokashiki, 2003. The Inference of crustal stresses in Ryukyu Islands. 3rd International Symposium on Rock Stress, Kumamoto, 349-354.

Aydan, Ö., Ulusay, R., 2023. A quick report on Pazarcık and Ekinözü earthquake (Türkiye) of February 2023 (This quick report has been available on the related web-sites since February 17, 2023). https://committees.jsce.or.jp/eec205/System/files/FINA_RU_OA_pazarcik_ekinozu_eqs_qr.pdf

Aydan, Ö., Kumsar, H. and Iwata, N. 2024. Frictional characteristics of the faults of the 2023 Great Turkish Earthquakes and the inference of their associated stress fields. 50th Japan Rock Mechanics Symposium, Tokyo (in press), 6 pages, JSCE.

Byerlee, J. 1978. Friction of rocks, Pure and Applied Geophysics, 116, 615-626.

Chorowicz, J., Luxey, P., Lyberis, N., Carvalho, J., Parrot, J.P., Yürür, T., Niyazi Gündogdu, N. 1994. The Maras Triple Junction (southern Turkey) based on digital elevation model and satellite imagery interpretation. Journal Geophysical Research. Solid Earth, 20225-20242.

Duman, T.Y. and Emre, Ö. 2013. The East Anatolian Fault: geometry, segmentation and jog characteristics. Geological Society of London Special Publication, 372 (1), p. 495–529.

Emre, Ö., Duman, T.Y., Özalp, S., Elmacı, H., Olgun, Ş., Şaroğlu, F., 2013, Açıklamalı Türkiye Diri Fay Haritası, Ölçek 1:1.250.000. Maden Tetkik ve Arama Genel Müdürlüğü, Özel Yayın Serisi-30, Ankara. ISBN: 978-605-5310-56-1

ERD,2023. Earthquake Research Department. https://tadas.afad.gov.tr/

Eringen, A.C. 1980. Mechanics of Continua, Huntington, N.Y., Robert E. Krieger Publishing Co., 606 p.

IPGP, 2023. Institut de Physique du Globe de Paris

GCMT, 2023. Global Centroid-Moment-Tensor (CMT) Project, Harvard University.

Goldberg, D. E., Taymaz, T., Reitman, N. G., Hatem, A. E., Yolsal-Çevikbilen, S., Barnhart, W. D., et al., 2023. Rapid characterization of the February 2023 Kahramanmaraş, Türkiye, earthquake sequence. The Seismic Record, 3(2), 156–167.

KOERI, 2023. Boğaziçi Üniversitesi Kandilli Rasathanesi ve Deprem Araştırma Enstitüsü (KRDAE), Bölgesel Deprem-Tsunami İzleme Ve Değerlendirme Merkezi (BDTİM) http://www.koeri.boun.edu.tr/sismo/2/tr/.

Kumsar, H., 2023. Personal communication on fault gouge from Değirmencik.

Okada, Y. 1992, Internal deformation due to shear and tensile faults in a half-space, Bull. Seismol. Soc. Am., 82(2), 1018–1040

Toda, S., Stein, R. S., Özbakir, A. D., Gonzalez-Huizar, H., Sevilgen, V., Lotto, G., and Sevilgen, S., 2023, Stress change calculations provide clues to aftershocks in 2023 Türkiye earthquakes,Temblor, http://doi.org/10.32858/temblor.295

Tuncay, E., Ulusay, R., Watanabe, H., Tano, H., Aydan, Ö., Yüzer E., 2002. Acoustic Emission (AE) technique: 2 – A preliminary investigation on the determination of in-situ stresses by AE technique in Turkey. Yerbilimleri, Vol. 25, 83-98.

Tuncay, E., Ulusay, R., Watanabe, H., Tano, H., Aydan, Ö., 2003. The measurement of the stress state of Turkey by Acoustic Emission (AE) method. 3rd International Symposium on Rock Stress, Kumamoto, Japan, 4 - 06 November 2003, pp.255-260

USGS, United States Geological Survey, https://earthquake.usgs.gov/earthquakes

Yürür, M. T. and Chorowicz, J., 1998. Recent volcanism, tectonics and plate kinematics near the junction of the African, Arabian and Anatolian plates in the eastern Mediterranean. Journal of Volcanology and Geothermal Research, 85/1-4 (1998) 1-15.

Yerbilimleri, 2024, 45 (1), 66-78, 1278778

Hacettepe Üniversitesi Yerbilimleri Uygulama ve Araştırma Merkezi Bülteni (*Bulletin of the Earth Sciences Application and Research Centre of Hacettepe University*

YERBİLİMLERİ
Bulletin for Earth Sciences

ISSN: 2687- 2978

Study Of Particles Flow Over Industrial Wobbler Type Feeder Using Discrete Element Method

Endüstriyel Wobbler Tipi Besleyici Üzerinden Parçacık Akışının Ayrık Elemanlar Yöntemi İle İncelenmesi

VİLAİAT ALEKPEROV [1*], **Esra BENLİCE**[1], **Zeynep DAĞTARLA**[1], **Ekrem SAVAŞ** [1]

[1] MEKA Crushing, Screening and Concrete Plant Technologies, R&D Center Department,
06909, Sincan, Ankara, Türkiye

Received *(geliş)*: 07 April *(Nisan)* 2023 Accepted *(kabul)*: 04 April *(Nisan)* 2024

ABSTRACT

Wobbler feeders are generally used to feed coarse material to the primary crusher in the mine and aggregate applications. In the operation, finer particles are also screened through the spaces among rollers and wobbling of the rocks through the roller cause impact and rubbing effect that helps to move undesired particle over batches. Motion of the materials on the feeder depends on design parameters such as roller size, rotation speed, spacing etc. and also gradation of the bulk material that fed into the feeder. The performance investigation of the feeder heavily relies on experimental studies due to complex motion of the material on the feeder as well as particle interaction in the batch. Discrete Element Method is a method that used to compute motion of large number of particles in a granular flow and it is widely accepted as an effective method in the rock mechanics. In this study, DEM is used to investigate the performance of a wobbler feeder. The feeder is designed and simulated for different parameters such as spacing, roller speed, particle shape and gradation in The Rocky DEM software. The particle velocities and trajectories were determined, and particle resident times were calculated to investigate the efficiency of the feeder for different disc configurations.

Keywords: Discrete element method, particle shape, wobbler feeder

ÖZ

Wobbler besleyiciler genellikle maden ve agrega uygulamalarında kaba malzemeyi birincil kırıcıya beslemek için kullanılır. Operasyonda, silindirler arasındaki boşluklardan daha ince parçacıklar da elenir ve kayaların silindir boyunca sallanması darbe ve sürtünme etkisine neden olarak istenmeyen parçacıkların yığınlar üzerinde hareket etmesine yardımcı olur. Malzemelerin besleyici üzerindeki hareketi, silindir boyutu, dönüş hızı, boşluk vb. gibi tasarım parametrelerine ve ayrıca besleyiciye beslenen dökme malzemenin gradasyonuna bağlıdır. Besleyicinin performans araştırması, malzemenin besleyici üzerindeki karmaşık hareketi ve yığındaki parçacık etkileşimi nedeniyle büyük ölçüde deneysel çalışmalara dayanır. Ayrık Elemanlar Yöntemi, çok sayıda parçacığın tanecikli bir akıştaki hareketini hesaplamak için kullanılan ve kaya mekaniğinde etkili bir yöntem olarak kabul edilen bir yöntemdir. Bu çalışmada, yalpalayan bir besleyicinin performansını araştırmak için AEM kullanılmıştır. Besleyici, Rocky DEM yazılımında boşluk, silindir hızı, parçacık şekli ve derecelendirme gibi farklı parametreler için tasarlanmış ve simüle edilmiştir. Parçacık hızları ve yörüngeleri *belirlenerek farklı disk konfigürasyonları için besleyicinin etkinliğini araştırmak üzere parçacık kalma süreleri hesaplanmıştır.*

Anahtar Kelimeler: *Ayrık eleman yöntemi, parçacık şekli, wobbler besleyici*

https://doi.org/10.17824/yerbilimleri.1278778

*Sorumlu Yazar/ Corresponding Author: valekperov@mekaglobal.com

INTRODUCTION

Different methods have been developed regarding feeding material in mining industry. Belt, apron, vibratory feeders are such examples. Vibrating feeder is a kind of feeding equipment widely used in metallurgy, coal, electric power, and chemical industries. It is used with other types of equipment together to realize the automatic operation of feeding, batching, quantitative packaging, and other processes (Z.J.Yin vd.,2010). For example, as the feeder vibrations occurred at its resonance frequency, vibration amplitude is highly dependent on a damping factor. On the other hand, the damping factor depends on the mass of the material on the feeder trough, the type of material, and the vibration amplitude (I. F. Goncharevich vd., 1990; T. Yanagida vd., 2001; O. Taniguchi vd., 1963)

Wobbler feeder is another type that is commonly used for removal of dirt and small undesired particles from raw material. Being able to perform two different processes, feeding and sieving, makes wobbler feeder different from others. Some feeders can screen bulk material while conveying materials to next process. Generally, vibrating grizzly feeders, Figure 1. From Meka Global that have grizzle bars are used for both feeding and scalping. Especially, wet and sticky materials may fill the opening between bars and grizzly feeder lack ability of screening unwanted material. To overcome this kind of problems, wobbler feeders are one of the best solutions. Working of a Wobbler feeder is similar to a roller screen. It is used for scalping out fines and feeding only oversize to a crusher. As shown in above figure, elliptical bars of steel are set in alternate vertical and horizontal positions in a Wobbler feeder. The elliptical bars rotate in the same direction, all at the same speed. Spacing between the bars remains constant throughout therotation.

Figure 1. Vibrating feeder and wobbler feeder
Şekil 1. *Titreşimli besleyici ve wobbler besleyici*

Looking at the literature, design workings is investigated using Discrete Element Method (DEM) with The Rocky DEM software. There are increasing reports of simulating of the screening process based on DEM (F. Elskamp vd., 2015; L.L. Zhao vd., 2016; M. Jahani vd., 2015; K.J. Dong vd., 2009; P.W. Cleary vd., 2018; Y.H. Chen vd., 2010). The initial numerical studies of the screening process were conducted with two-dimensional (2D) DEM to investigate the particle motion on the deck (J. Li, C. Webb vd., 2003).Then, a three-dimensional (3D) DEM model for a screening process of particles on a simply vibrated screen deck was developed (P.W. Cleary vd., 2002).

Ashrafizadeh and Ziaei-Rad considered the influence of material shape on its movement and used rectangular blocks instead of mass points to study material movement using the DEM (H. Ashrafizadeh and S. Ziaei-Rad., 2013) Kong et al. established a sliding and jumping motion model of materials based on Coulomb’s law of friction and collision principle, and the model is used to DEM analyze method the changes of material motion under different vibration conditions (X. X. Kong vd., 2015). Considering the studies on the subject are about roller screens which are another type of feeder and design intent is not feeding large sized materials, this work will provide an insight about wobbler feeders screening characteristics. In this study, a wobbler feeder design was investigated using Discrete Element Method (DEM) with The Rocky DEM software. The design variables of the feeder were the spacing between rollers and the rotation speed of the rollers. The effect of material that is fed into the wobbler was also investigated and different particle shape (L/D), the material (limestone and iron ore) and the gradation was simulated. In order to investigate the performance of the feeder, the particle motions were analyzed.

Particle passing percentage through each roller spacing were calculated and the residence time of the particle over the feeder was determined to discuss the performance of the wobbler feeder.Considering the studies on the subject are about roller screens which are another type of feeder and design intent is not

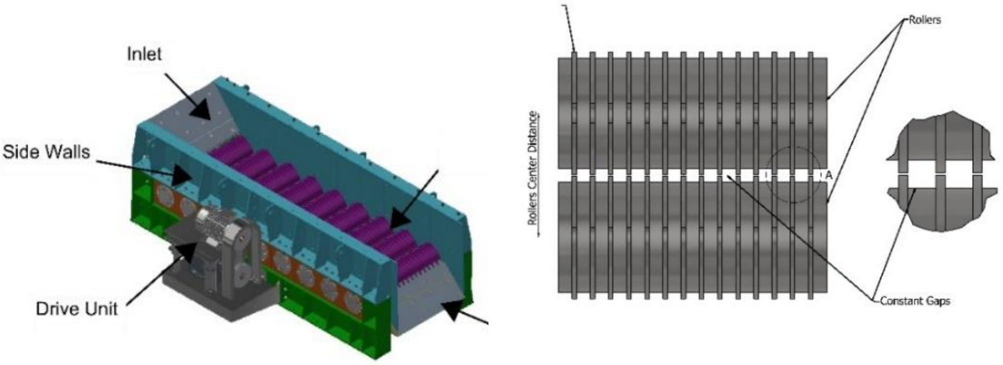

Figure 2. Wobbler feeder disc configuration

Şekil 2. *Wobbler besleyici disk formu* feeding large sized materials, this work will provide an insight about wobbler feeders screening characteristics.

MATERIALS AND METHODS

Wobbler Geometry

The wobbler feeder moves material forward with disc groups rotated by means of chains. All disc groups are rotating synchronously, in the same direction with same speed and two types of wobbler feeders are simulated in which the spacing between rollers are 40x40 mm and 60x60 mm. Overall dimensions of the feeder is 1200 mm in width and 3500 mm in length.

Distances between rollers came from EN standards for the drive chains (DIN 8187:1984). The space between the disc groups always remains the same because of the disc configuration (Figure 2). Hereby, the unwanted materials which are sand, dirt, soil etc. are discharged from those spaces. Besides, the clean particles move forwards along the rotation direction of the disk (Figure 3) and desired materials discharged from the exit. In Table 1, the wobbler feeder's simulation parameters are given in detail.

DEM, Simulation Setup

DEM is an effective numerical method to calculate the mechanical behavior of discrete particles based on Newton's law of motion (H.P. Zhu, et al. 2008, Zhu, Z.Y. Zhou et al. 2007, W.Q. Zhong 2016).

In this work, real size wobbler model is used in simulations. Feeding material chosen as Limestone (G1) and Iron Ore (G2) which are obtained from MEKA customer's material requirements. Their shapes are polyhedron (Figure 4). The size gradation is given inTable 2 and equipment properties are given in Table1. Density, Young's modulus and Poisson's ratio of boundaries are 7850kg/m^3, 210 GPa and 0,3 respectively. Details of all simulation parameters are listed in from Rocky Table 3.

RESULTS AND DISCUSSION

In this part, particle passing percentages, particle movement velocity and particle resident time were examined to obtain optimum parameters for screening efficiency.

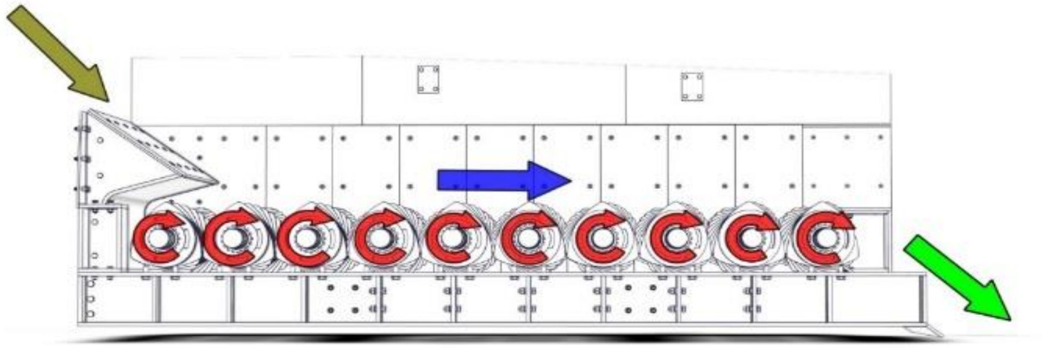

Figure 3. Simulation showing all disk groups running in synchronicity

Şekil 3. *Eş zamanlı çalışan disk gruplarını gösteren simülasyon*

Table 1. Equipment properties

Tablo 1. *Ekipman özellikleri*

Parameters	**Values**
Feed rate (t/h)	300
Types of gradation	Limestone (G1), Iron ore (G2)
Number of rollers	12
Spacing (mm)	40x40, 60x60
Roller speed (rpm)	20, 40, 60
Distance between two rollers (mm)	381
Feeder Length (mm)	3500
Feeder Width (mm)	1200
Roller Diameter (mm)	406

Figure.4. Selected feed materials shapes

Şekil 4. *Seçilen besleyici malzemelerin şekilleri*

Particle Passing Percentages

To examine working condition, passing percentages of undersize particles were examined for each spacing. For this reason, 12 cubes were created under each roller as shown in Figure 5. Also, at the exit of the wobbler, cube was created to consider overflow.

In Figure 6. It is observed that, overall passing percentage is increasing with the increase of roller rotation speed. To investigate passing percentages along the wobbler, each section of spacings were examined. Efficiency of all sections under the wobblers are shown In Figure 7.

Passing percentages almost is same for all cases at the beginning of section of the wobbler where nearest to inlet, though there is sharp decrease from 4th section till the 9th section. Also, almost every passing percentage is zero after 9th section which indicate that there is not any undersize material in this section. It also should be noted that generation order of particles changes in every simulation hence smaller particles may be created in the start of the simulation or in the later stages.

Particle passing percentage were examined which is one of the important parameters giving information about efficiency of the wobbler. Although, undersized particles escaped from overflow which is not desirable in application area general screening efficiency is compensating undersized material percent at discharge. As a result, optimum roller speed should be arranged for the optimum operation. Considering these configurations, although 60

Table 2. Size grading of materials

Tablo 2. *Malzemelerin boyut sınıflandırılması*

Particle Size Distribution			
Limestone (G1)		**Iron Ore (G2)**	
Size (mm)	**Cumulative (%)**	**Size (mm)**	**Cumulative (%)**
609.6	100	1066.8	100
304.8	52	914.4	85
203.2	41	508	70
152.4	34	406.4	61
101.6	27	355.6	56
76.2	22	304.8	52
50.8	17	254	46
38.1	15	203.2	41
25.4	12	152.4	34
19.05	10	101.6	26.7
12.7	8	76.2	22.5
9.53	7	50.8	14.7
6.35	5	38.1	14.9
4.76	4	25.4	12
2.38	3	19.05	9.8
2	0	12.7	8.1
		7.76	4.3
		2.38	3

Table 3. Properties of Limestone (G1), Iron ore (G2) materials

Tablo 3. *Kireçtaşı (G1), Demir cevheri (G2) malzemelerinin özellikleri*

Gradation **Properties of Particles**	G1	G2
Bulk Density (mt/m^3)	1.60	2.40
Specific Gravity	2.65	3.40
Coefficient of restitution	0.30	0.30
Coefficient of static friction	0.70	0.70
Coefficient of dynamic friction	0.70	0.70

rpm roller speed has higher efficiency it results in higher percentage of undersize material in overflow thus requires more sections which in turn leads to longer wobbler feeder configuration.

Particle Velocity

Another parameter affecting efficiency of the wobbler is particle velocity (Figure 8.) It should be examined to improve the screening efficiency and to obtain durable machine. To investigate wobbler efficiency, particle velocity was examined at different roller rotation speeds such as 20, 40 and 60 rpm. Totally, 12 conditions were examined, and data were obtained after reaching steady state to get accurate results. Also, size of particles was chosen to be between 80 and 90 mm for all conditions. The reason is that sizes in that range is larger than from both gap sizes. In Figure 8. absolute velocity of gradations at same gap sizes (40x40 mm and 60x60 mm) shown with respect to the roller rotation speed. As shown in Figure 8. For low bulk density particle, G1, absolute velocity at 20 rpm is 0.25 m/s while it is 0.46 m/s for high bulk density particle G2 at the 60 rpm roller speed for the gap size of 40x40mm. On the other hand, velocity change for G1 and G2 are 528% and 236 % respectively. Moreover, gap size for 60x60 mm is shown in Figure 8. For the particle G1, absolute velocity at 20 rpm is 0,18 m/s whereas for G2, it is 0,63 m/s. Also, velocity percentages are 412% and 44% respectively. It is clear that particle velocities are directly proportional to rollers rotation speed. As rollers speed is increasing, particle absolute velocity also increases.

Particle Resident Time and Trajectory

In addition to the particle velocities on the wobbler, particle resident time is another parameter that helps understand particle behavior over the wobbler. When particle resident time is decreasing, there is a possibility of undersized particles escaping to overflow section. On the contrary, increased particle resident time results in undersized particles passing from spacing. Former leads to decrease of performance. To this extent, optimum resident time should be obtained for high performance wobbler. Figure 9. gives detailed information about particle resident times for all cases. The resident times described as particles traveling time between entry and exit of the boundary domain. All values obtained after system reached steady state regime.

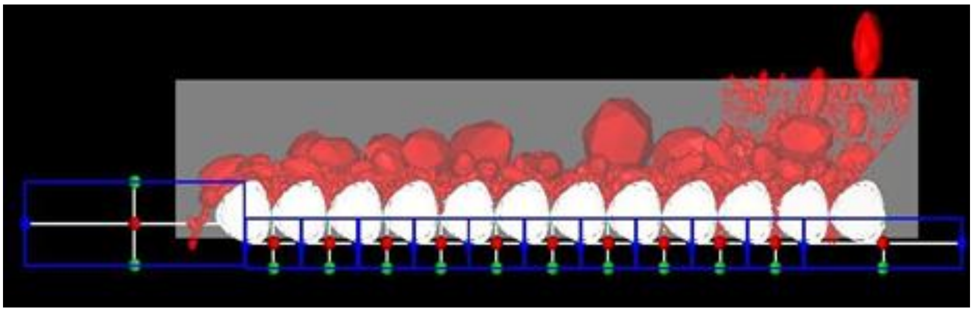

Figure 5. Simulation cube setup for particle passing percentages

Şekil 5. *Parçacık geçiş yüzdeleri için simülasyon küpü kurulumu*

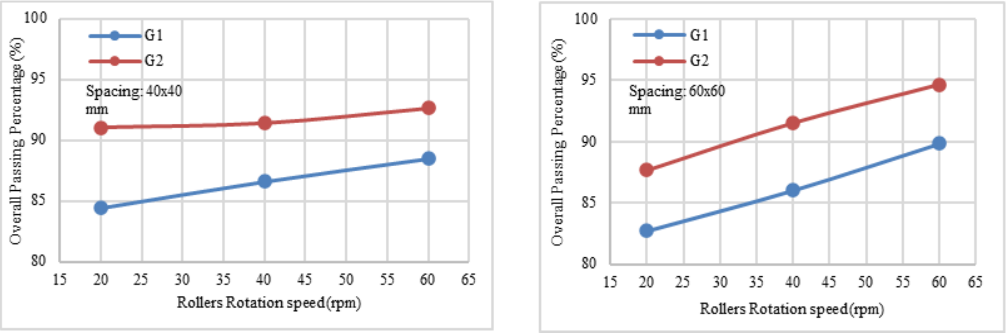

Figure 6. Overall passing percentage

Şekil 6. *Genel geçme yüzdesi*

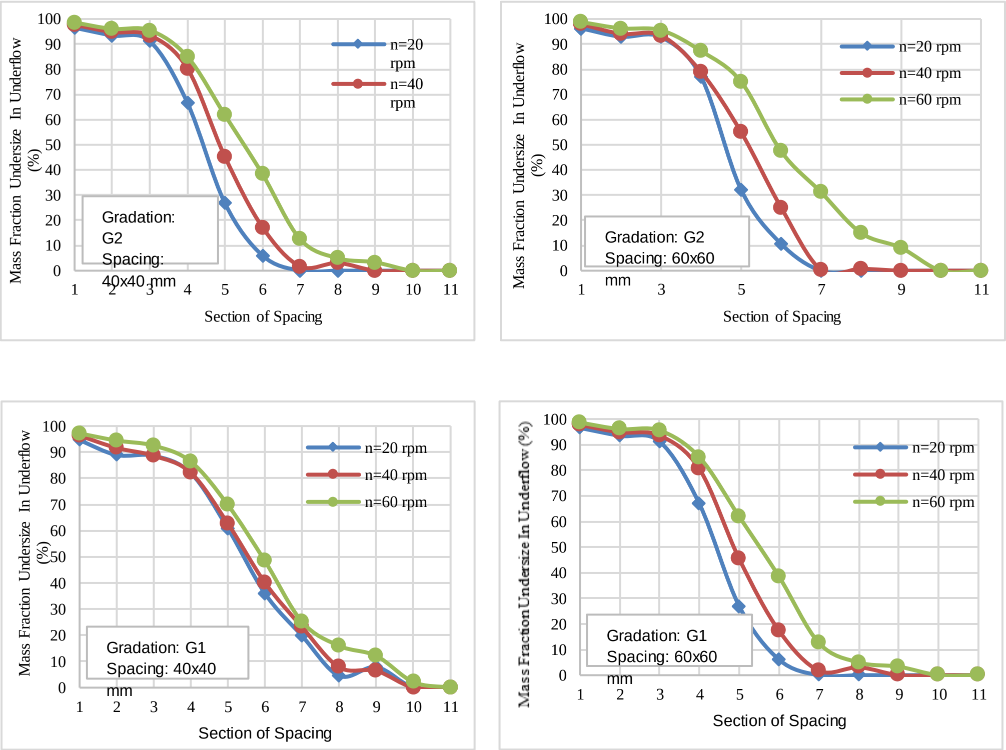

Figure 7. Undersize mass fraction for each spacing

Şekil 7. *Her boşluk için küçük kütle kesri*

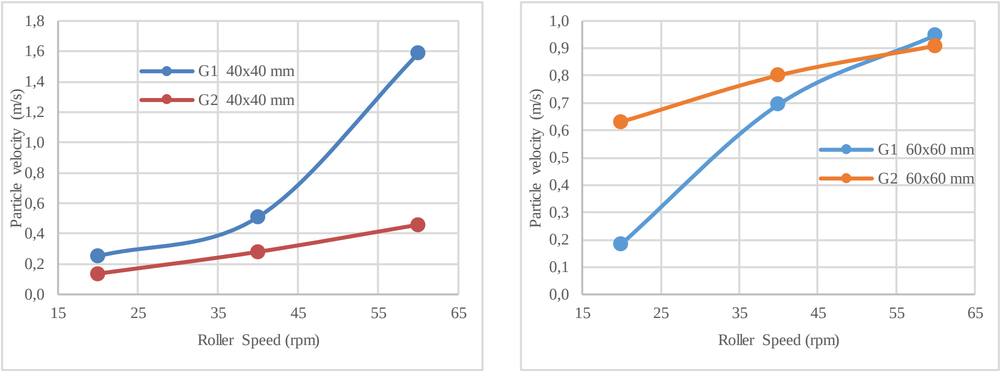

Figure 8. Absolute translational velocity of oversized particles

Şekil 8. *Büyük parçacıkların mutlak öteleme hızı*

Figure 9. shows particle resident time with respect to roller speeds for both low and high bulk density particles. All cases were examined for constant feed rate of 300 t/h. It became obvious that particle bulk density does not have enormous effect on resident time. Nonetheless, resident time is decreasing while roller rotation speed is increasing. For low bulk density particle, resident time is 29.5 sec, 15.45 sec and 11.2 sec in 20 rpm, 40 rpm and 60 rpm respectively for spacing of 40x40 mm. Besides, for high bulk density, resident time is 23.8 sec, 18.9 sec and 11.8 sec in 20 rpm, 40 rpm and 60 rpm respectively for spacing of 40x40 mm (In Figure 9.) Although having higher translational velocity at that time oversized particles moving forward on the Wobbler feeder may experience delayed motion and keep tumbling when stuck in between rollers and result in increased resident time. To understand particle behavior in detail, trajectory of the oversize particle is examined.

Only one particle is selected for all cases and size is chosen between 80-90 mm. In Figure 10, trajectories of the particles are shown for Gradation 1 and spacing 40x40mm. As it can be seen from figures, while rotation speed is smaller, particle is tumbling repeatedly between two rollers. However, in high roller speed, particle moves more quickly as expected. In addition, for undersized and very large particle, trajectories were obtained which is presented in Figure 11. Undersized particle (21.58 mm) directly passed form gaps whereas oversized particle (575.5 mm) moves forwards without any tumbling at 40 rpm, 40x40 mm gap and G1 gradation conditions.

Effect of Different Configurations on Screening Efficiency

The following formula is used to calculate the screening efficiency for condition of 40 rpm,40x40 mm gap and G1.

$$\mathrm{E_u} = \frac{\mathrm{Mass}_{\mathrm{U}_{\mathrm{Underflow}}}}{\mathrm{Mass}_{\mathrm{U}_{\mathrm{Feed}}}} \quad (1) \qquad \mathrm{E_O} = \frac{\mathrm{Mass}_{\mathrm{O}_{\mathrm{Overflow}}}}{\mathrm{Mass}_{\mathrm{O}_{\mathrm{Feed}}}} \quad (2) \qquad \mathrm{E} = \mathrm{E_U} * \mathrm{E_O} \quad (3)$$

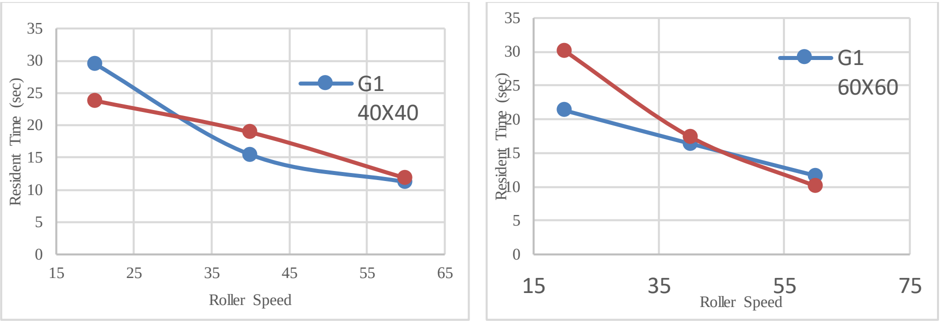

Figure 9. Particle resident time vs. roller speed

Şekil 9. *Parçacık kalma süresi ve silindir hızı*

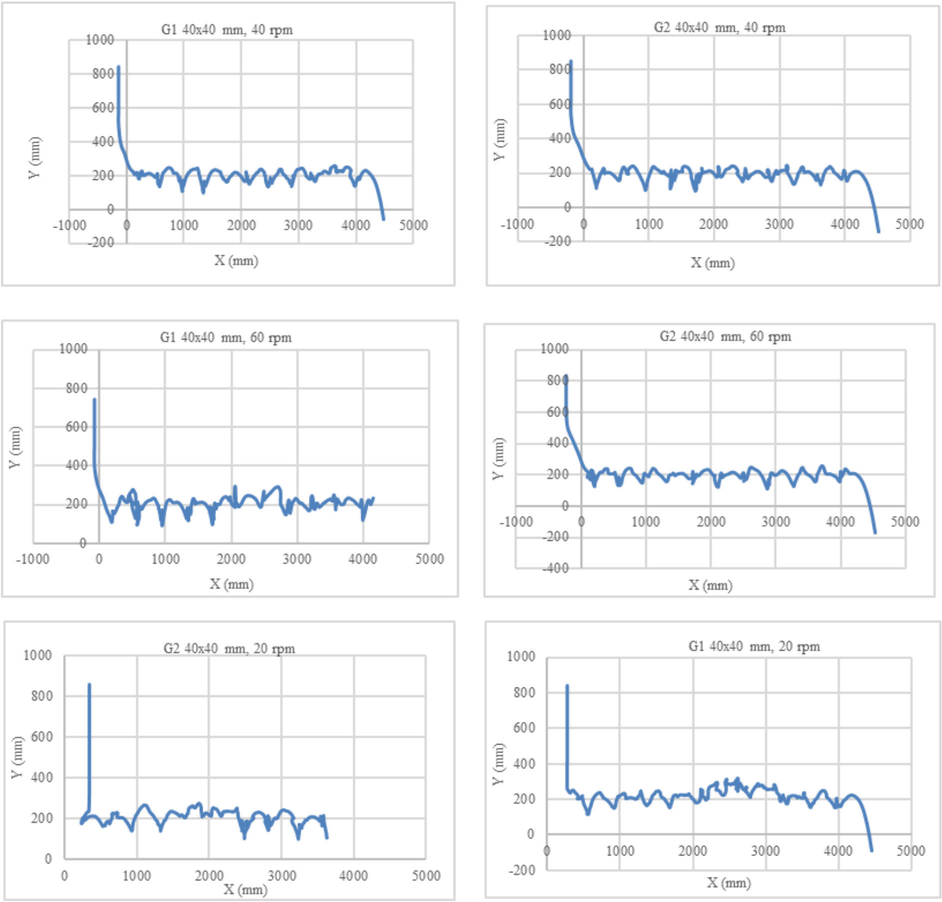

Figure 10. Oversize particle trajectory

Şekil 10. *Büyük boyutlu parçacık yörüngesi*

Efficiency results for corresponding configurations are as follows:

Herringbone configuration:

$$E_u = \frac{1250{,}38\ \text{kg}}{1266{,}85\ \text{kg}} = 0{,}986 \qquad E_O = 1$$

$$E = E_U = 98{,}6\%$$

Straight configuration:

$$E_u = \frac{1238{,}75\ \text{kg}}{1261{,}17\ \text{kg}} = 0{,}982 \qquad E_O = 1$$

$$E = E_U = 98{,}2\%$$

Cross configuration:

$$E_u = \frac{1196{,}2\ \text{kg}}{1231{,}45\ \text{kg}} = 0{,}971 \qquad E_O = 1$$

$$E = E_U = 97{,}1\%$$

CONCLUSION

In this study, motion of complex raw material for Wobbler Feeder is simulated with Discrete Element Method considering the effects of resident time and particle velocity. Simulations were run for three parameters 20,40 and 60 RPM, which maintains regular feeding of oversize particles and screening of undersize particles from gaps formed by triangular shaped discs.

Based on the results of screening efficiency and particle resident time the optimum roller speed was observed to be 40 RPM for both 40x40 and 60x60 gap. For low bulk density material (G1) resident time is 15.45 seconds whereas for high bulk density material (G2) resident time is 18.9 seconds for 40x40 mm gap. These results indicates that roller rotation speed has an important effect on particle flow characterization and screening efficiency.

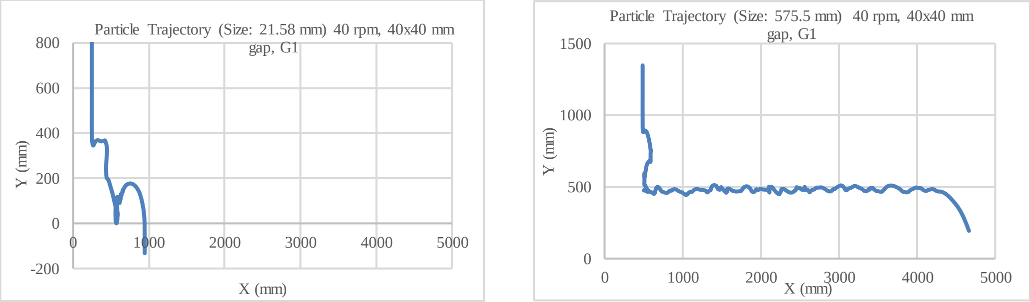

Figure 11. Undersize and oversize particle trajectory

Şekil 11. *Küçük ve büyük boyutlu parçacık yörüngesi*

Although with the increasing rotation speed feeding performance is increasing, it has an adverse effect in terms of particle resident time. For G1 material 40x40 mm and G2 material 40x40mm gap resident times are 13% and 6% higher comparing in 60 RPM compared to 40 RPM. Since decrease in resident time creates a possibility of undersize particle to escape into overflow, and increase of resident time means feeding of oversized particle will slow down, 40 RPM speed is an optimum choice rather than 60 RPM, where resident time is lower and 20 RPM where resident time is higher in described configuration. According to efficiency results herringbone configuration is higher than both straight and cross configurations, while latter two are still have quite adequate efficiency percentages.

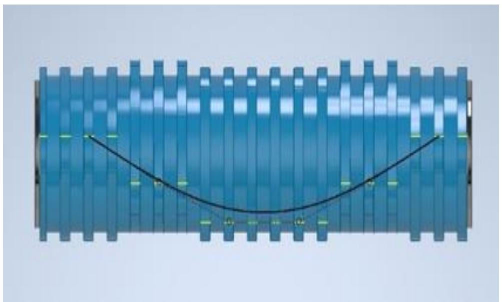

Figure 12. Herringbone configuration

Şekil 12. Balıksırtı form

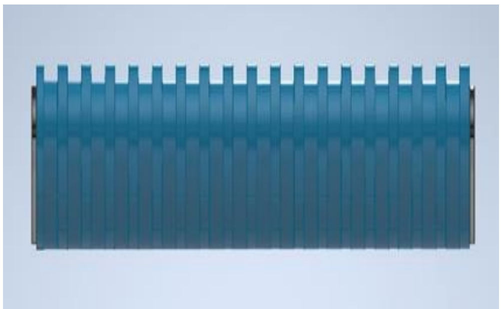

Figure 13. Straight configuration

Şekil 13. *Düz form*

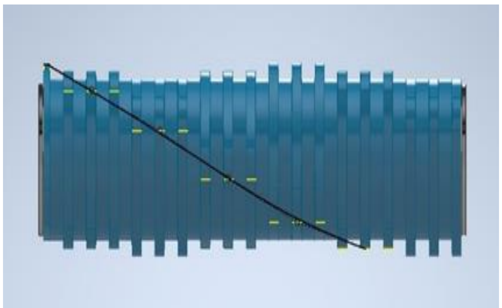

Figure 14. Cross configuration

Şekil 14. *Çapraz form*

For future work study can be done on comparison of simulation results with site tests. Effects of interaction coefficients could also be studied for different types of particles.

ACKNOWLEDGEMENT

Our work was carried out within the MEKA Crushing and Screening Technologies R&D Center. We thank the company for its contribution.

REFERENCES

Deutsches Institut für Normung (DIN)., 1984.European type roller chains DIN 8187

F. Elskamp, H. Kruggel-Emden, Review and benchmarking of process models for batch screening based on discrete element simulations, Adv. Powder Technol. 26 (2015) 679–697.

H. Ashrafizadeh and S. Ziaei-Rad, “A numerical 2D simulation of part motion in vibratory bowl feeders by discrete element method,” Journal of Sound and Vibration, vol. 332, no. 13, pp. 3303–3314, 2013.

H.P. ZHU., Z.Y. ZHOU., R.Y. YANG., A.B. YU., 2008. Discrete particle simulation of particulate systems: a review of major applications and findings. Chem. Eng. Sci. 63, 5728–5770.

I. F. Goncharevich, K. V. Frolov, and E. I. Rivin, Theory of Vibratory Technology. New York: Hemisphere, 1990.

J. Li, C. Webb, S.S. Pandiella, G.M. Campbell, Discrete particle motion on sieves -a numerical study using the DEM simulation, Powder Technol. 133 (2003) 190–202.

K.J. Dong, A.B. Yu, I. Brake, DEM simulation of particle flow on a multi-deck banana screen, Miner. Eng. 22 (2009) 910–920.

L.L. Zhao, Y.M. Zhao, C.Y. Bao, Q.F. Hou, A.B. Yu, Laboratory-scale validation of a DEM model of screening processes with circular vibration, Powder Technol. 303 (2016) 269–277.

MekaGlobal., https://www.mekaglobal.com/en/products/crushing-screening-plants/feeders/vibrating-feeder-with-grizzly-screen

MekaGlobal., https://www.mekaglobal.com/en/products/crushing-screening-plants/feeders/wobbler-feeders

M. Jahani, A. Farzanegan, M. Noaparast, Investigation of screening performance of banana screens using LIGGGHTS DEM solver, Powder Technol. 283 (2015) 32–47.

O. Taniguchi, M. Sakata, Y. Suzuki, and Y. Osanai, “Studies on vibratory feeder,” Bull. JSME, vol. 6, no. 21, pp. 37–43, 1963.

P.W. Cleary, M.L. Sawley, DEM modelling of industrial granular flows: 3D case studies and the effect of particle shape on hopper discharge, Appl. Math. Model. 26 (2002) 89–111.

P.W. Cleary, P. Wilson, M.D. Sinnott, Effect of particle cohesion on flow and separation in industrial vibrating screens, Miner. Eng. 119 (2018) 191–204.

T. Yanagida, A. J. Matchett, and J. M. Coulthard, “Dissipation energy of powder beds subject to vibration,” Trans. IChemE, vol. 79, pt. A, no. 6, pp. 655–662, Sep. 2001.

W.Q. ZHONG., A.B. YU., X.J. LIU., Z.B. TONG., H. ZHANG., 2016. DEM/CFD-DEM modelling of non-spherical particulate systems: theoretical developments and applications, Powder Technol. 302, 108–152.

X. X. Kong, X. J. Xi, and B. C. Wen, “Analysis of motion of the part on the linear vibratory conveyor,” Journal of Northeastern University (Natural Science), vol. 36, no. 06, pp. 827–831, 2015.

Y.H. Chen, X. Tong, Modeling screening efficiency with vibrational parameters based on DEM 3D simulation, Min. Sci. Technol. 20 (2010) 615–620.

Yerbilimleri, 2024, 45 (1), 79-92, 1357103

Hacettepe Üniversitesi Yerbilimleri Uygulama ve Araştırma Merkezi Bülteni (*Bulletin of the Earth Sciences Application and Research Centre of Hacettepe University*

YERBİLİMLERİ
Bulletin for Earth Sciences

ISSN: 2687- 2978

An experimental study on uniaxial compressive strength values of silicate based resin added sand samples with different types of fiber reinforcements

Farklı lif türleri ile güçlendirilmiş silikat bazlı reçine katkılı kum numunelerinin tek eksenli sıkışma dayanımı değerleri üzerine deneysel bir çalışma

EREN KÖMÜRLÜ [1*], ATİLA GÜRHAN ÇELİK [1], VEYSEL KARAKAYA [2]

[1] Giresun Üniversitesi İnşaat Mühendisliği Bölümü, Giresun, Türkiye

[2,] Ali Acar İnşaat Sanayi ve Ticaret Ltd. Şirketi, Giresun, Türkiye

Received *(geliş):* 08 September *(Eylül)* 2023 Accepted *(kabul)*: 05 April *(Nisan)* 2024

ABSTRACT

In this study, uniaxial compressive strength values of a sand type soil reinforced with polypropylene fiber and silicate-based resin additives with different amounts were investigated. Microgrid fiber (MGF) was tested as a new polypropylene fiber additive in the experiments to compare it with a conventional polypropylene fiber type geosynthetic product used in soil fill improvement applications. According to the findings obtained from the uniaxial compressive strength (unconfined compressive strength) tests, it was determined that the new MGF type fiber usually increased the strength values at higher rates in comparison with the conventional fiber product. As another outcome, it was found that target strength values can be supplied by using less resin amounts for the specimens with fiber additives. It was determined that proper strength improvements can be obtained more economically by the fiber additive use together with the resin, rather than the resin added mixtures without the fiber.

Keywords: ***G***eofiber, geosynthetics, , microgrid fiber, resin added soils, strengths of sand type fills

ÖZET

Bu çalışmada, farklı oranlarda polipropilen lif ve silikat bazlı reçine katkı ile güçlendirilmiş kum türü bir zeminin tek eksenli sıkışma dayanımı değerleri incelenmiştir. Toprak dolgu uygulamalarında kullanımı yaygın olan bir polipropilen lif türü geosentetik ürünle kıyaslanması amacıyla deneylerde yeni bir polipropilen lif katkı olarak mikro hasır lif (MHL) test edilmiştir. Tek eksenli sıkışma dayanımı (serbest basınç mukavemeti) deneylerinden elde edilen bulgulara göre, MHL türü yeni lif ürünlerin geleneksel life kıyasla dayanım değerlerinde daha yüksek oranlarda artış sağladığı belirlenmiştir. Ayrıca, lif kullanımı ile kum türü zeminlerin istenilen dayanım değeri artışlarının daha az reçine kullanılarak sağlandığı görülmüştür. Lif katkının reçine ile birlikte kullanılması yolu ile lif içermeyen reçineli karışımlara kıyasla daha ekonomik olarak hedef dayanım değerlerine sahip olunabildiği belirlenmiştir.

Anahtar kelimeler: *Geofiber, geosentetikler, mikro hasır lif, reçine katkılı zeminler, kum türü dolgu dayanımları* https://doi.org/10.17824/yerbilimleri.1357103

*Sorumlu Yazar/ Corresponding Author: ekomurlu@giresun.edu.tr

INTRODUCTION

Geosynthetics are generally produced from polymeric materials and used in geotechnical engineering with different purposes like reinforcement, filling, isolation, drainage and etc. Geosynthetics can be used as an alternative to conventional materials, or can be used together with conventional materials in geotechnical engineering. Depending on the polymer material type, geosynthetics can be divided into two main groups as thermosets and thermoplastics. Thermosets are purchased before their polymerization as in the liquid form. One or more components of thermosets in the liquid form are mixed, chemically react with each other and solidify in a consequence of the polymerization. Thermoset geosynthetics are used in various applications of spraying membranes, grouting in anchorage holes, ground improvement injections and etc. (Guner and Ozturk, 2016; Holter, 2016; Sabri et al., 2021; Spagnoli, 2021; Komurlu, 2023a).

Although polymerization reactions of thermosets are typically completed within a day, a significant solidification generally happens in one hour. There are three stages of the thermoset polymerization. The first one is cream time; polymerization does not start and the mix of components is in the liquid phase in this stage. By the end of this time, the gel time and polymerization start. During the gel time, thermosets pass from the liquid phase to the solid phase. In the third stage called tack free time, material solidifies completely and the polymerization ends. Therefore, the maximum mechanical strength is reached at the end of the tack free time (Komurlu and Kesimal, 2015; Komurlu and Kesimal, 2017; Węgrzyk et al. 2023).

Depending on the application necessities, the thermoset products can be chosen considering their solidification times. For instance, quite short liquid phase times are preferred in spraying membrane applications. On the other hand, longer liquid phase times are preferred for ground injection works for supplying a proper penetration in the soil voids and/or cracks in rock masses. Also, relatively long cream and gel times are preferred in the resin added soil mixes used in filling applications to have enough time for a good homogenization property. Liquid phase times of different thermosets can vary within a big interval from several seconds to tens of minutes (Ajalloeian et al., 2013; Collico et al., 2023; Pratter et al., 2023).

Thermoset polymer resins can be injected into the soil in place or can be mixed with soils to prepare a filling material mix. Geosynthetics are preferred considering their mechanical properties and their high chemical resistances which make them advantageous in terms of their service lifetimes. Another important reason for using polymer materials is their high energy absorption capacities. Engineering polymers that provide good mechanical properties are preferred because of their strength values as well as their high energy absorption capacities (Komurlu et al., 2017; Kolay and Dhakal, 2020; Komurlu, 2021; Komurlu et al., 2014).

High energy absorption capacity geosynthetics supply an advantage of improvement under both static and dynamic load conditions by providing soil reinforcement. As some polymer resins can polymerize in contact with water, novel resin type geosynthetics can supply another important advantage in the watery regions against conventional materials (Luciani and Peila, 2019; Komurlu, 2020). Geosynthetics are also usable to improve the liquefaction resistance of soils (Latha and Lakkimsetti, 2022; Lakimsetti and Gali, 2023; Lakkimsetti and Latha, 2023). Due to their different advantages, the use of geosynthetics is becoming more widespread every day.

Fiber additive use is a reinforcement method for soil filling applications. Fiber additives which provide high adherence to the soil particles improve the reinforcement performance. For the supply of a good adherence property, the size and geometry properties of fibers are determinative (Patel and Singh, 2017; Divya et al., 2020; Patel and Singh, 2020; Tiwari et al., 2020) Also, fiber material has an important effect on the strength values of reinforced soils (Khajeh et al., 2020; Malicki et al., 2021; Zafar et al. 2023).

Microgrid fiber (MGF) is a new geosynthetic type with small mesh openings with sizes like several tens or hundreds of micrometers. Microgrid usage was previously investigated for soil improvement works as an alternative for the classical geogrids (Mittal and Shukla, 2019; Mittal and Shukla, 2020; Vieira and Pereira, 2022). The “microgrid” term is suggested to use for grid sizes below 2.5 mm according to the study authored by Leshchinsky et al. (2016). As a novelty of this study, microgrids were cut into pieces and used as a new fiber type for resin added soil mixes. In comparison with ordinary fiber products, it is estimated that the MGF reinforcement can provide higher adherence to soil particles due to its structural properties. MGF is the combination of thin plastic fiber ribs in groups of two or more different directions, which form mini grids. There are several structural properties that can vary the grid performances like rib dimensions, planar angles, junction characteristics, aperture size and shape. As similar with geogrids, MGFs can be biplanar, triplanar or quadroplanar. Lengths of MGF pieces can change in a typical interval of those of conventional geofibers. As a motivation of this study, a bettered adherence performance was estimated from MGF additives because combined fibers can work together in their use. In addition, grid type physical property was thought to make an additional friction coefficient for the soil particle contacts because proper adherence performances can be achieved by attaching grain edges to the grids. Grid type reinforcement inclusions can provide an interlocking mechanism with the grains (Gu et al., 2017; Hajitaheriha et al., 2021).

Good adherence property of the reinforcement provides a significant advantage not only in the strength values, but also in the crack propagation resistance, as well as the energy absorption capacity of the reinforced soil materials (Dhar and Hussain, 2019; Lv et al., 2021; Zhou et al. 2023). In this study, effect of a conventional polypropylene fiber (PPF) additive which is commonly used in geotechnical engineering and new MGF on the strength values of resin added sand type soil mixes were comparatively investigated with a series of experimental studies. It should be noted herein that the MGF additive is also made of the polypropylene type engineering polymer material. Details of the experimental study are given under the next section. Investigation of the new MGF type additive use can be noted herein as the main novelty of this study. In addition, use of different fiber types with resin additives is thought to be another remarkable point to make cost-effective solutions in soil improvement works.

MATERIALS VE METHODS

A sieve analysis was performed to classify the soil sample used in this study. The particle size distribution obtained from the sieve analysis is given in Table 1. According to the unified soil classification system (USCS), the soil sample with the Cu (coefficient of uniformity) value of 10 and the Cc (coefficient of curvature) value of 1.25 was classified as a well-graded sand (SW). As parameters for the soil classification system, 93.4% and 4.1% of particles are smaller than 4.76 mm (No. 4) and 0.075 mm (No. 200), respectively. The ratios by masses in the specimen contents with different amounts of resin and fiber additives are given in Table 2. The sandy soil having a natural moisture content of 19% was mixed with resin. The natural moisture content was determined by drying specimens at 105°C in the stove.

Table 1. Particle size distribution of the soil specimen

Tablo 1. Zemin numunesi tane boyu dağılımı

Sieve size	0.075 mm (No. 200)	0.150 mm (No. 100)	0.300 mm (No. 50)	0.850 mm (No. 20)	2.00 mm (No. 10)	4.76 mm (No.4)
% Passing	4.1	9.7	20.2	41.3	67.9	93.4

Table 2. Contents of specimens (M_{resin}: Mass of resin, M_{sand}: Mass of sand, M_{fiber}: Mass of fiber, M_{SR}: Mass of sand and resin, NF: No fiber)

Tablo 2. *Numune içerikleri (M_{resin}: Reçine kütlesi, M_{sand}: Kum kütlesi, M_{fiber}: Lif kütlesi, M_{SR}: Kum ve reçine kütlesi, NF: Lif yok)*

Specimen type	M_{resin}/M_{SR}	M_{sand}/M_{SR}	M_{fiber}/M_{SR}
8R-NF	0.08	0.92	0
14R-NF	0.14	0.86	0
20R-NF	0.20	0.80	0
8R-0.5PPF, 8R-0.5MGF	0.08	0.92	0.005
8R-1.0PPF, 8R-1.0MGF	0.08	0.92	0.010
8R-1.5PPF, 8R-1.5MGF	0.08	0.92	0.015
14R-0.5PPF, 14R-0.5MGF	0.14	0.86	0.005
14R-1.0PPF, 14R-1.0MGF	0.14	0.86	0.010
14R-1.5PPF, 14R-1.5MGF	0.14	0.86	0.015
20R-0.5PPF, 20R-0.5MGF	0.20	0.80	0.005
20R-1.0PPF, 20R-1.0MGF	0.20	0.80	0.010
20R-1.5PPF, 20R-1.5MGF	0.20	0.80	0.015

In Figure 1, MGF and PPF type polypropylene fibers are seen. Both MGF and PPF type fibers have 10 mm length. The MGF type fiber has square shape geometry with a width of 10 mm and the grid size of 1.2 mm. Contents of the mixes were sensitively weighed using an electronic scale (Figure 2). The resin was added in the specimen mixes as the last ingredient. Specimens were mixed by hand in a basin for 150 seconds. It should be noted herein that specimens were molded within the liquid phase time of the resin additive. 3 specimens were molded for the each specimen type. Specimens were filled into the molds in three layers and compacted with 15 hammer strokes after each layer (Figure 3). It was cared that details of molding and remolding processes were totally same for all the specimens used in this study. Diameter of the cylindrical split plastic molds is 50 mm and the ratio of length to diameter of the specimens is 2 in this study. Resin added specimens were cured for a day before the remolding process, and one week cured specimens were used in the UCS (uniaxial compressive strength) test. Specimens used in this study are seen in Figure 4. A sensitive electric motor press with the loading capacity of 50 kN was used to measure the load values (Figure 5). In the UCS test, the loading rate was chosen to be 0.5 mm/min.

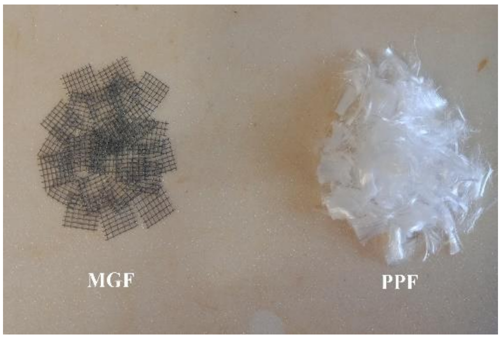

Figure 1. Fiber types used in this study

Şekil 1. *Çalışmada kullanılan lif türleri*

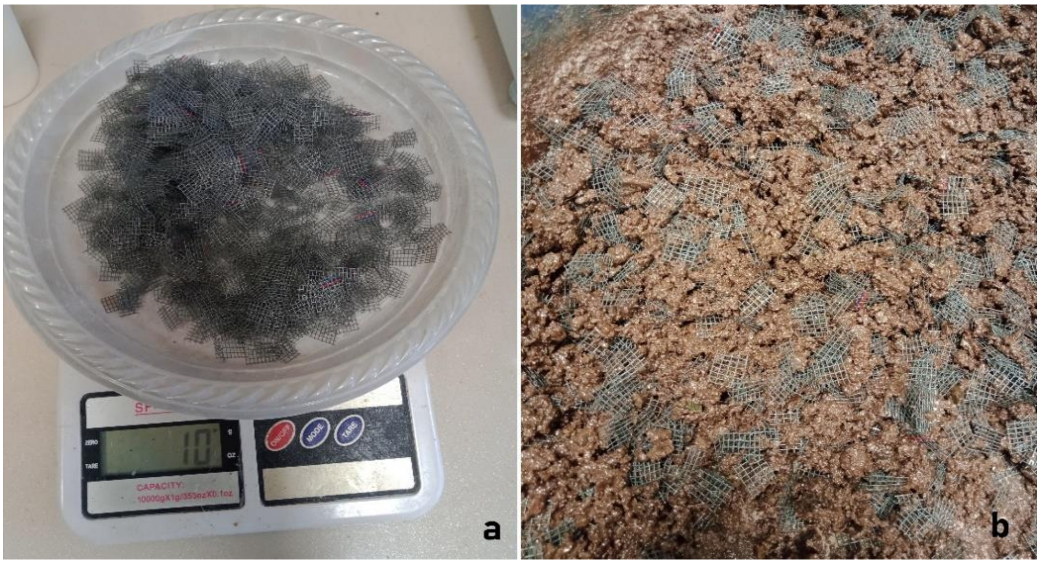

Figure 2. a) A photo from weighing processes, b) a view of MGF added soil mix

Şekil 2. *a) Tartım işlemlerinden bir görsel, b) MGF katkılı zemin görüntüsü*

Figure 3. a) Components of the resin, b) specimen mixing, c and d) specimen molding

Şekil 3. *a) Reçine birleşenleri, b) numune karıştırma, c ve d) numune kalıplama*

Figure 4. Specimens used in this study

Şekil 4. *Çalışmada kullanılan numuneler*

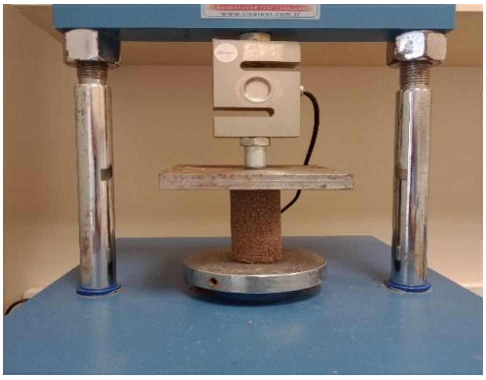

Figure 5. A photo from the uniaxial compressive strength test

Şekil 5. *Tek eksenli sıkışma dayanımı deneyinden bir görüntü*

RESULTS AND DISCUSSIONS

Uniaxial compressive strength (UCS) test results obtained from this study are given in Table 3. In addition, results of this study are graphically given in Figure 6 to comparatively show the strength values obtained from different specimen mixes. As it can be well estimated, strength values of specimens were determined to increase with an increase in the amount of resin additive. The fiber additive was also found to significantly improve the strength values of specimens. Instead of using only resin additive, it was evaluated that target strength values can be reached in a more economical way by using fiber reinforcement in resin added soils. Therefore, it was assessed to be advantageous to use fiber and resin additives together. To deal about the costs in the year of 2023, it can be noted that the price of the silicate based thermoset resin is 2.7 USD per a kilogram, and the price of polypropylene fiber products used in this study typically varies from 5.2 to 5.5 USD per a kilogram. The use of 20% resin additive means that 200 kg resin additive is used in a ton of the soil mix. In this case, 540 USD is spent for a ton of the soil mix. This price is too high for typical ground fill applications. In case 8% resin and 0.5% fiber are used together, the cost approximately decreases to 243 USD for a ton of the soil mix. In other words, the cost is reduced by more than half. The soil reinforcement costs can be made to be affordable by using fiber products in the resin added soils.

When the strength values and costs of the mixes are assessed together, it is recommended to use fiber reinforcement in resin added sands. The amount of fiber in the mixes is an important parameter that determines the strength value (Chou and Ngo, 2018; Zhao et al., 2020). Fiber additives must be used in the correct ratio in mixes. In the case of excessive use of fiber additives, strength values of soil mixes decrease (Gao et al., 2017; Mirzababaei et al., 2018). Threshold fiber content that begins to reduce strength values of resin-added samples may differ from those of resin-free and some other binder-free soils. Therefore, some resin added samples still had no decrease in strength values at the 1.5% fiber content rate.

Table 3. Uniaxial compressive strength (UCS) test results (SN: Specimen number, SD: Standard deviation)

Tablo 3. *Tek eksenli sıkışma dayanımı deney sonuçları (SN: Numune sayısı, SD: Standart sapma)*

Specimen type	UCS (MPa)	SN	SD (MPa)
8R-NF	1.05	3	0.08
14R-NF	1.73	3	0.07
20R-NF	2.61	3	0.15
8R-0.5PPF	2.67	3	0.19
8R-1.0PPF	3.08	3	0.26
8R-1.5PPF	3.90	3	0.21
14R-0.5PPF	9.23	3	0.58
14R-1.0PPF	11.74	3	0.52
14R-1.5PPF	12.15	3	0.63
20R-0.5PPF	14.64	3	0.75
20R-1.0PPF	17.51	3	0.84
20R-1.5PPF	12.20	3	0.71
8R-0.5MGF	2.81	3	0.23
8R-1.0MGF	3.97	3	0.29
8R-1.5MGF	4.69	3	0.26
14R-0.5MGF	10.64	3	0.90
14R-1.0MGF	13.80	3	0.85
14R-1.5MGF	10.99	3	0.78
20R-0.5MGF	13.22	3	0.60
20R-1.0MGF	21.74	3	0.97
20R-1.5MGF	17.58	3	1.03

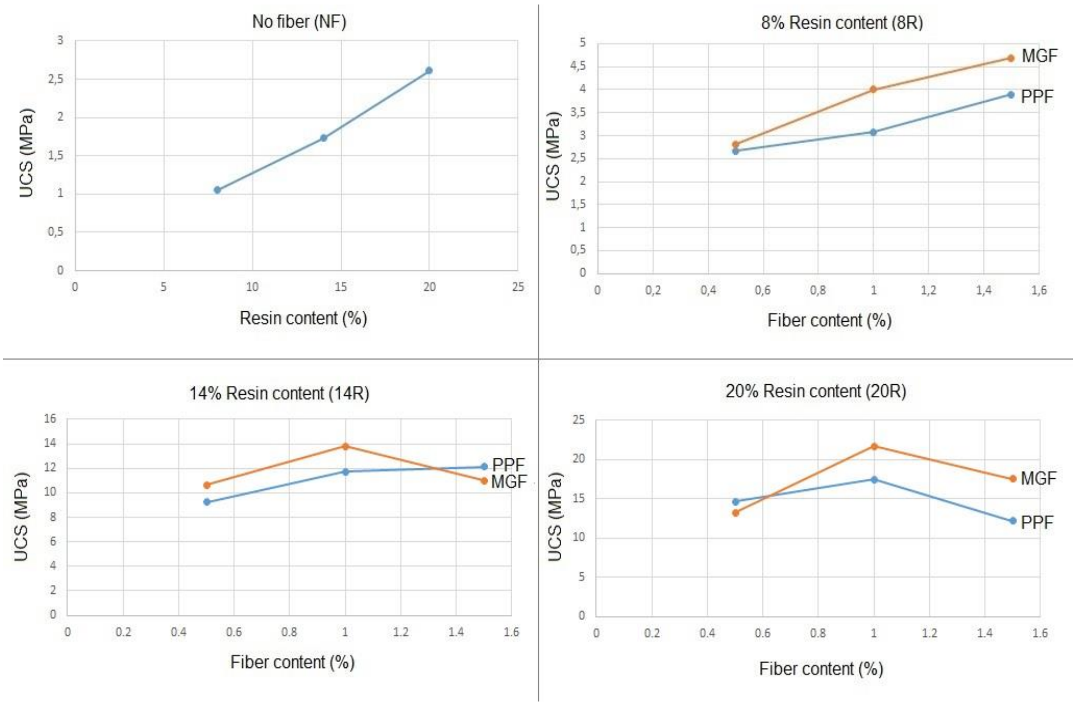

***Figure 6.** Graphical shown of the UCS test results*

***Şekil 6.** Tek eksenli sıkışma dayanımı deneyi sonuçlarının grafiksel gösterimi*

In this study, MGF additive was examined as a new fiber type and found usable to increase the strength values of soil mixes. According to the results of this study, it has been found that MGF type additive is usually more advantageous in terms of increasing in strength values, in comparison with the conventional PPF type fiber additive. This study is a preliminary one on the MGF usage to reinforce soils. In order to better understand the properties of the MGF additive, different parametric studies can be carried out within the scope of new investigations. For instance, different topics like grid size, fiber size and geometry, fiber material can be examined to better understand the effect of MGF additive use. Fiber size, geometry and material are important parameters varying the reinforcement performances (Shukla, 2017; Bos et al., 2019; Shafei et al., 2021). Likewise, the relationship between fiber size and soil particle size distribution is another important parameter in terms of strength values of fiber reinforced soil mixes (Pradhan et al., 2012; Anagnostopoulos et al., 2013; Yixian et al., 2016). It is possible to further improve the MGF additive efficiency within new studies on such issues. It is believed that there is a good potential for many new research topics for the use of MGF products as a new fiber type.

It has been observed from the MGF use that target strength values can be reached by using less fiber compared to the use of conventional fiber additives. In addition to the strength improvement purposes, fiber additives are also used for increasing the ductility and energy absorption capacity values of reinforced soils (Firoozi et al., 2017; Boz et al., 2018; Rathod and Reddy, 2021). It is also a new topic to investigate energy absorption capacity and ductility properties of MGF added soil mixes in the further studies. It is hoped that this study will be a beneficial reference for new researches on different fiber-reinforced soil mix designs.

It should be noted herein that the findings of this study are for the use of polypropylene type polymer fiber material. Both conventional and MGF type fibers used in this study are made of polypropylene type engineering polymer. Other geofiber materials can be investigated within further studies. In this regard, it should be noted that non-corrosive fiber materials must be preferred in soil mixes to prevent strength losses due to the ground water contact. Plastic geofiber materials like polypropylenes are advantageous as a result of their good chemical resistivity and non-corrosive property.

The soil reinforcement performance of MGF additives has been investigated in various research studies. In a previous study conducted by Komurlu (2023b), MGF-type fiber additives were utilized in cement-stabilized aggregate mixes. Similar to the findings of this study, it was observed that polypropylene MGF-type fibers provide greater increases in strength values compared to conventional polypropylene fiber (PPF) products. Komurlu (2023b) concluded that MGF-type novel additives offer improved adherence and reinforcement performance under both compression and indirect tension (splitting) conditions compared to conventional fiber additives.

Fiber additive is a strengthening method that can be preferred in ground filling applications.

In soil fill applications, issues such as curing times of resins, the order of additions to the mixture and the appropriate liquid phase time property of resin products should be considered in terms of obtaining a good homogeneity and proper reinforcement efficiency (Naeini et al., 2012; Masoumi et al., 2013; Vakili et al., 2023). High-strength soil fill materials can be created using different fiber and resin combinations. Following new materials and developments in material sciences can bring new solutions in geoengineering disciplines.

CONCLUSION

The following sentences can be noted to conclude this study: According to the results, the silicate based resin additive was assessed to notably increase the strength values of tested sand samples. On the other hand, it is suggested to use the resin additive with the fiber reinforcement in mixes to obtain better strength values while reducing the costs of the soil mixes. Different fiber types were comparatively tested and the microgrid fiber (MGF) was investigated as a new geofiber type within this study. Considering the outcomes of this study, MGF reinforcement was assessed to be able to supply better strength improvement of silicate resin added sand samples in comparison with a conventional fiber product. The MGF type fiber reinforcement was found to be usable and advantageous in soil filling works. There are numerous new research topics on MGF products with different designs and their use for different soil mixes. It is believed that MGF type new geofibers have a significant potential to become more popular in the near future of geotechnical engineering.

ACKNOWLEDGEMENT

This study has been supported by FEN-BAP-A-090323-24 coded scientific research project of Giresun University. Authors express their sincere thanks for the support by the Giresun University Scientific Research Projects Coordination Unit.

REFERENCES

Ajalloeian, R., Matinmanesh, H., Abtahi S.M., Rowshanzamir, M., 2013. Effect of polyvinyl acetate grout injection on geotechnical properties of fine sand. Geomechanics and Geoengineering, 8(2), 86-96. DOI: 10.1080/17486025.2012.705897

Anagnostopoulos, C.A., Papaliangas, T.T., Konstantinidis, D., Patronis, C., 2013. Shear Strength of Sands Reinforced with Polypropylene Fibers. Geotechnical and Geological Engineering, 31, 401–423. DOI: 10.1007/s10706-012-9593-3

Bos, F.P., Bosco, E., Salet, T.A.M., 2019. Ductility of 3D printed concrete reinforced with short straight steel fibers. Virtual and Physical Prototyping, 14(2), 160-174. DOI: 10.1080/17452759.2018.1548069

Boz, A., Sezer, A., Özdemir, T., Hızal, G.E., Dolmacı, Ö.A., 2018. Mechanical properties of lime-treated clay reinforced with different types of randomly distributed fibers. Arabian Journal of Geosciences, 11, 122. DOI: 10.1007/s12517-018-3458-x

Chou, JS., Ngo, NT., 2018. Engineering strength of fiber-reinforced soil estimated by swarm intelligence optimized regression system. Neural Computing and Applications, 30, 2129–2144. DOI: 10.1007/s00521-016-2739-0

Collico, S., Spagnoli, G., Tintelnot, G., 2023. Statistical Analysis of Grouted Tertiary Sands with Acrylate and Polyurethane. International Journal of Geosynthetics and Ground Engineering, 9, 41. DOI: 10.1007/s40891-023-00457-8

Dhar, S., Hussain, M., 2019. The strength behaviour of lime-stabilised plastic fibre-reinforced clayey soil, Road Materials and Pavement Design, 20 (8), 1757-1778. DOI: 10.1080/14680629.2018.1468803

Divya, P.V., Viswanadham, B. V. S., Gourc, J.P. 2020. Influence of fibre morphology on the integrity of geofibre-reinforced soil barriers. Geosynthetics International, 27 (5), 460-475. DOI: 10.1680/jgein.20.00006

Firoozi, A.A., Guney Olgun, C., Firoozi, A.A., Baghini, M.S., 2017. Fundamentals of soil stabilization. Geo-Engineering 8, 26. DOI: 10.1186/s40703-017-0064-9

Gao, L., Zhou, Q., Yu X., Wu, K., Mahfouz A.H., 2017. Experimental study on the unconfined compressive strength of carbon fiber reinforced clay soil. Marine Georesources and Geotechnology, 35(1), 143-148. DOI: 10.1080/1064119X.2015.1102184

Gu, M., Han, J., Zhao, M., 2017. Three-dimensional DEM analysis of single geogrid-encased stone columns under unconfined compression: a parametric study. Acta Geotechnica, 12, 559–572. DOI: 10.1007/s11440-017-0547-z

Guner, D., Ozturk, H. Experimental and Numerical Analysis of the Effects of Curing Time on Tensile Mechanical Properties of Thin Spray-on Liners. Rock Mechanics and Rock Engineering, 49, 3205–3222. DOI: 10.1007/s00603-016-0997-x

Hajitaheriha, N.M., Akbarimehr, D., Hasani Motlagh, A., Damerchilou, H., 2021. Bearing capacity improvement of shallow foundations using a trench filled with granular materials and reinforced with geogrids. Arabian Journal of Geosciences, 14, 1431. DOI: 10.1007/s12517-021-07679-y

Holter, K.G. 2016. Performance of EVA-Based Membranes for SCL in Hard Rock. Rock Mechanics and Rock Engineering, 49, 1329–1358.

Khajeh, A., Jamshidi Chenari, R., Payan, M., 2020. A Simple Review of Cemented Non-conventional Materials: Soil Composites. Geotechnical and Geological Engineering, 38, 1019–1040. DOI: 10.1007/s10706-019-01090-x

Kolay, P.K., Dhakal, B., 2020. Geotechnical Properties and Microstructure of Liquid Polymer Amended Fine-Grained Soils. Geotechnical and Geological Engineering, 38, 2479–2491. DOI: 10.1007/s10706-019-01163-x

Komurlu, E., 2020. Investigation of Uniaxial Compressive Strength values of a Polyvinyl resin reinforced Silt: An Experimental Study on resin amount and curing temperature. International Journal of Engineering, Design and Technology, 2(2), 82-87.

Komurlu, E., 2021. Use of Polymeric Energy Absorption Liners to Improve the Concrete Rock Fall Barriers. Geoscience Engineering, 67(4), 168-175. DOI: 10.35180/gse-2021-0062

Komurlu, E., 2023a. A resin type additive use to improve load bearing capacities of grouted rock bolts exposed to thermal cycles. Journal of Engineering Sciences and Designs, 11(2), 743-754. DOI: 10.21923/jesd.1214531

Komurlu, E., 2023b. Use of microgrid fiber as a new reinforcement additive to improve compressive and tensile strength values of cemented rock fill mixes. International Journal of Mining, Reclamation and Environment, 37(10), 760-768. DOI: 10.1080/17480930.2023.2266200

Komurlu, E., Kesimal, A., 2015. An Experimental Study on Polyurethane Foam Reinforced Soil use as Rock-like Material. Journal of Rock Mechanics and Geotechnical Engineering, 7(5), 566-572. DOI: 10.1016/j.jrmge.2015.05.004

Komurlu, E., Kesimal, A., 2017. Usability of Thin Spray-on Liners (TSL) for Akarsen Underground Mine in Murgul. 25th International Mining Congress and Exhibition of Tukey (IMCET 2017), Antalya, Turkey, pp. 89-104

Komurlu, E., Kesimal, A., Colak, U., 2014. Polyurea type Thin Spray-on Liner Coating to Prevent Rock Bolt Corrosion. 8th Asian Rock Mechanics Symposium, 1389-1397, Sapporo, Japan

Komurlu, E., Kesimal, A., Aksoy, C.O., 2017. Use of Polyamide-6 type Engineering Polymer as Grouted Rock Bolt Material. International Journal of Geosynthetics and Ground Engineering, 3, Paper no: 37, DOI: 10.1007/s40891-017-0114-6

Lakkimsetti, B., Gali, M.L., 2023. Grain Shape Effects on the Liquefaction Response of Geotextile-Reinforced Sands. International Journal of Geosynthetics and Ground Engineering, 9, 15. DOI: 10.1007/s40891-023-00434-1

Lakkimsetti, B., Latha, G.M., 2023. Effectiveness of Different Reinforcement

Alternatives for Mitigating Liquefaction in Sands. International Journal of Geosynthetics and Ground Engineering, 9, 37. DOI: 10.1007/s40891-023-00459-6

Latha, G.M., Lakkimsetti, B., 2022. Morphological Perspectives to Quantify and Mitigate Liquefaction in Sands. Indian Geotechnical Journal, 52, 1244–1252. DOI: 10.1007/s40098-022-00649-5

Leshchinsky, B., Evans, T.M., Vesper, J., 2016. Microgrid inclusions to increase the strength and stiffness of sand. Geotextiles and Geomembranes, 44, 170-177. DOI: 10.1016/j.geotexmem.2015.08.003

Luciani, A., Peila, D., 2019. Tunnel Waterproofing: Available Technologies and Evaluation through Risk Analysis. International Journal of Civil Engineering, 17, 45–59. DOI: 10.1007/s40999-018-0328-6

Lv, C., Zhu, C., Tang, C.S., Cheng, Q., Yin, L.Y., Shi, B., 2021. Effect of fiber reinforcement on the mechanical behavior of bio-cemented sand. Geosynthetics International, 28(2), 195-205. DOI: 10.1680/jgein.20.00037

Malicki, K., Górszczyk, J., Dimitrovová, Z., 2021. Recycled Polyester Geosynthetic Influence on Improvement of Road and Railway Subgrade Bearing Capacity—Laboratory Investigations. Materials, 14, 7264. DOI: 10.3390/ma14237264

Masoumi, E., Abtahi Forooshani, S.M., Abdi Nian, F., 2013. Problematic Soft Soil Improvement with Both Polypropylene Fiber and Polyvinyl Acetate Resin. Geotechnical and Geological Engineering, 31, 143–149. DOI: 10.1080/19386362.2020.1775358

Mirzababaei, M., Arulrajah, A., Haque, A., Nimbalkar, S., Mohajerani, A., 2018. Effect of fiber reinforcement on shear strength and void ratio of soft clay. Geosynthetics International, 25(4), 471-480. DOI: 10.1680/jgein.18.00023

Mittal, A., Shukla, S., 2019. Effect of geosynthetic reinforcement on strength behaviour of weak subgrade soil. Material Science Forum, 969, 225-230. DOI: 10.4028/www.scientific.net/MSF.969.225

Mittal, A., Shukla, S., 2020. Effect of Geogrid Reinforcement on Strength, Thickness and Cost of Low-volume Rural Roads. Jordan Journal of Civil Engineering 14, 587-598.

Naeini, S.A., Naderinia, B., Izadi, E., 2012. Unconfined compressive strength of clayey soils stabilized with waterborne polymer. KSCE Journal of Civil Engineering, 16, 943–949. DOI: 10.1007/s12205-012-1388-9

Patel, S.K., Singh, B., 2017. Experimental Investigation on the Behaviour of Glass Fibre-Reinforced Cohesive Soil for Application as Pavement Subgrade Material. International Journal of Geosynthetics and Ground Engineering, 3, 13. DOI: 10.1007/s40891-017-0090-x

Patel, S.K., Singh, B., 2020. A Comparative Study on Shear Strength and Deformation Behaviour of Clayey and Sandy Soils Reinforced with Glass Fibre. Geotechnical and Geological Engineering, 38, 4831–4845. DOI: 10.1007/s10706-020-01330-5

Pradhan, P.K., Kar, R.K., Naik, A., 2012. Effect of Random Inclusion of Polypropylene Fibers on Strength Characteristics of Cohesive Soil. Geotechnical and Geological Engineering, 30, 15–25. DOI: 10.1007/s10706-011-9445-6

Pratter, P., Boley, C., Forouzandeh, Y., 2023. Innovative Ground Improvement with Chemical Grouts: Potential and Limits of Partial Saturation with Polymers. Geotechnical and Geological Engineering, 41, 477–489. DOI: 10.1007/s10706-022-02301-8

Rathod, R.S.B., Reddy, B.V.V., 2021. Strength and stress–strain characteristics of fibre reinforced cement stabilised rammed earth. Materials and Structures, 54, 52. DOI: 10.1617/s11527-021-01640-x

Sabri, M.M.S., Vatin, N.I., Alsaffar, K.A.M., 2021. Soil Injection Technology Using an Expandable Polyurethane Resin: A Review. Polymers, 13, 3666. DOI: 10.3390/polym13213666

Shafei, B., Kazemian, M., Dopko, M., Najimi, M. 2021. State-of-the-Art Review of Capabilities and Limitations of Polymer and Glass Fibers Used for Fiber-Reinforced Concrete. Materials, 14, 409. DOI: 10.3390/ma14020409

Shukla, S.K., 2017. Fundamentals of Fibre-Reinforced Soil Engineering. Springer Nature Singapore Pte Ltd. Singapore, ISSN 2364-5164

Spagnoli, G., 2021. A review of soil improvement with non-conventional grouts. International Journal of Geotechnical Engineering, 15(3), 273-287. DOI: 10.1080/19386362.2018.1484603

Tiwari, N., Satyam, N., Patva, J. 2020. Engineering Characteristics and Performance of Polypropylene Fibre and Silica Fume Treated Expansive Soil Subgrade. International Journal of Geosynthetics and Ground Engineering, 6, 18. DOI: 10.1007/s40891-020-00199-x

Vakili, A.H., Rastegar, S., Golkarfard, H., Salimi, M., Izadneshan, Z., 2023. Effect of polypropylene fibers on internal erosional behavior of poorly graded sandy soil stabilized with the binary mixtures of clay and polyvinyl acetate. Environmental Earth Sciences, 82, 294. DOI: 10.1007/s12665-023-10961-9

Vieira, C.S., Pereira, P.M., 2022. Influence of the Geosynthetic Type and Compaction Conditions on the Pullout Behaviour of Geosynthetics Embedded in Recycled Construction and Demolition Materials.

Sustainability, 14, 1207. DOI: 10.3390/su14031207

Węgrzyk, G., Grzęda, D., Ryszkowska, J., 2023. The Effect of Mixing Pressure in a High-Pressure Machine on Morphological and Physical Properties of Free-Rising Rigid Polyurethane Foams—A Case Study. Materials, 2023, 16, 857. DOI: 10.3390/ma16020857

Yixian, W., Panpan, G., Shengbiao, S., Haiping, Y., Binxiang, Y., 2016. Study on Strength Influence Mechanism of Fiber-Reinforced Expansive Soil Using Jute. Geotechnical and Geological Engineering, 34, 1079–1088. DOI: 10.1007/s10706-016-0028-4

Zafar, T., Ansari, M.A., Husain, A., 2023. Soil stabilization by reinforcing natural and synthetic fibers – A state of the art review. Materials Today: Proceedings, onlinefirst, DOI: 10.1016/j.matpr.2023.03.503.

Zhao, Y., Ling, X., Gong, W., Li, P., Li, G., Wang, L., 2020. Mechanical Properties of Fiber-Reinforced Soil under Triaxial Compression and Parameter Determination Based on the Duncan-

Chang Model. Applied Sciences, 10, 9043. DOI: 10.3390/app10249043

Zhou, L., Chen, J.F., Zhuang, X.Y., 2023. Undrained cyclic behaviors of fiber-reinforced calcareous sand under multidirectional simple shear stress path. Acta Geotechica, 18, 2929–2943. DOI: 10.1007/s11440-022-01780-6